



**Michigan
Technological
University**

Michigan Technological University
Digital Commons @ Michigan Tech

Dissertations, Master's Theses and Master's Reports

2019

EXPLORING THE ROLE AND IMPACT OF MICROSCALE PHENOMENA ON ELECTRODE, MICRODEVICE, AND CELLULAR FUNCTION

Sanaz Habibi

Michigan Technological University, habibi@mtu.edu

Copyright 2019 Sanaz Habibi

Recommended Citation

Habibi, Sanaz, "EXPLORING THE ROLE AND IMPACT OF MICROSCALE PHENOMENA ON ELECTRODE, MICRODEVICE, AND CELLULAR FUNCTION", Open Access Dissertation, Michigan Technological University, 2019.

<https://doi.org/10.37099/mtu.dc.etdr/800>

Follow this and additional works at: <https://digitalcommons.mtu.edu/etdr>



Part of the [Biochemical and Biomolecular Engineering Commons](#), [Biomedical Devices and Instrumentation Commons](#), and the [Complex Fluids Commons](#)

EXPLORING THE ROLE AND IMPACT OF MICROSCALE PHENOMENA ON
ELECTRODE, MICRODEVICE, AND CELLULAR FUNCTION

By

Sanaz Habibi

A DISSERTATION

Submitted in partial fulfillment of the requirements for the degree of

DOCTOR OF PHILOSOPHY

In Chemical Engineering

MICHIGAN TECHNOLOGICAL UNIVERSITY

2019

© 2019 Sanaz Habibi

This dissertation has been approved in partial fulfillment of the requirements for the Degree of DOCTOR OF PHILOSOPHY in Chemical Engineering.

Department of Chemical Engineering

Dissertation Advisor: *Dr. Adrienne Minerick*

Committee Member: *Dr. Caryn Heldt*

Committee Member: *Dr. Tony N. Rogers*

Committee Member: *Dr. Smitha Rao*

Department Chair: *Dr. Pradeep K. Agrawal*

Dedication

To:

my mother, Shahnaz, my father, Reza, my sisters Sahar and Sadaf, and my dear husband

Mohammad Reza.

Table of Contents

List of Figures	x
List of Tables	xiii
Preface	xiv
Acknowledgments.....	xv
Abstract.....	xvii
Chapter 1: Introduction and Outline	1
1.1 Introduction.....	1
1.2 Microfluidics and Electrokinetics.....	2
1.3 Polarization Mechanisms	4
1.4 Dielectrophoretic Phenomena	5
1.4.1 Single-Shell Spherical DEP Polarization Model.....	9
1.4.2 Single-Shell Oblate DEP Polarization Model	10
1.4.3 Mammalian cells	12
1.5 Types of Dielectrophoresis Electrode Designs	13
1.6 Implemented Material within Dielectrophoresis-used Microfluidic Systems.....	14
1.7 Conclusions.....	15
Chapter 2: Dielectrophoretic Literature Review for Biomedical Sciences Applications ..	19
2.1 Introduction.....	19

2.2 Biomedical Science Applications	20
2.2.1 Cell Lysis.....	21
2.2.2 Cell Membrane Capacitance	25
2.3 Current Dielectrophoretic Challenges and Limitations.....	29
2.3.1 Biocompatibility Change in Spatially Non-uniform AC DEP Fields	30
2.3.2 Interactions between Biological Cell and DEP Medium Additives	35
2.4 Conclusions.....	38
Chapter 3: Exploring the Role and Impact of Faradaic Reactions on Hemolysis in Non-Uniform AC Electric Fields.....	41
3.1 Introduction.....	41
3.2 Materials and Methods	52
3.2.1 Microdevice Design and Fabrication	52
3.2.2 Chemicals and Preparation.....	52
3.2.3 Sample Preparation.....	54
3.2.4 Electrical Signal Optimization of the Uncoated Microdevice.....	54
3.2.5 Simulations	55
3.2.6 Electrical Signal Optimizations of the HfO ₂ Microdevices.....	56
3.2.7 Data Analysis	57
3.3 Results and Discussion.....	58

3.3.1 Electrical Signal Optimization of the Uncoated Microdevices	59
3.3.2 Electrical Signal Optimization of the HfO ₂ Coated Microdevices.....	60
3.3.3 Time and Spatial Dependence of Hemolysis in Non-Uniform AC Fields	62
3.3.4 Isolating Faradaic Reaction Contributions to Ion Concentration Changes	65
3.3.5 Membrane Stabilization against Ion Fluctuations	69
3.3.6 Faradaic Reaction Effects at Electrode Surfaces.....	71
3.4 Conclusions.....	73
Chapter 4: Investigating the Impact of Low Concentration Surfactant on Red Blood Cell	
Dielectrophoretic Responses.....	76
4.1 Introduction.....	76
4.2 Dielectrophoresis Theory and Background	79
4.2.1 Single-Shell Oblate Particles.....	80
4.2.2 Quantifying DEP Spectra from Cell Velocities	82
4.3 Materials and Methods	84
4.3.1 Chemicals and preparation	84
4.3.2 Microfluidics Design and Fabrication	85
4.3.3 Blood Experiments	86
4.3.4 UV-Vis Experiments	86
4.3.5 Data Acquisition and Analysis	88

4.4 Results and Discussion	91
4.4.1 Hemolysis and Cell Size Dependence on Triton X-100 Concentrations	91
4.4.2 RBC Integrity Analysis via UV-Vis Spectroscopy	93
4.4.3 Qualitative Dielectrophoretic Behavior	97
4.4.4 Quantitative Dielectrophoretic Spectra	100
4.4.5 Single-Shell Oblate Dielectrophoretic Force Model	102
4.5 Conclusions	108
Chapter 5: Dielectric Changes in Membrane Properties of Porcine Kidney Cells Before and After Porcine Parvovirus Infection	110
5.1. Introduction	111
5.2. Dielectrophoresis Theory and Background	114
5.2.1 Single-Shell Spherical DEP Polarization Model	115
5.2.2. Quantifying DEP Force Spectra on Bioparticles by Velocity Tracking Measurements	117
5.3. Materials and Methods	118
5.3.1. Chemicals and Preparation	118
5.3.2. Cell Culture, Virus Infection, and Osmolyte Treatment	119
5.3.3. Microfluidics Design and Fabrication	120
5.3.4. DEP Solution Preparation and Experiments	121

5.3.5. Cell Viability Assessment	122
5.3.6. Cell Selection and Data Acquisition	123
5.4. Results and Discussion.....	124
5.4.1. Qualitative Dielectrophoretic Behavior.....	125
5.4.2. Cell Population Analysis	126
5.4.3. Cell Viability Assessment	128
5.4.4. Quantitative Dielectrophoretic Spectra	130
5.4.5. Cell Membrane Capacitance	133
5.5. Conclusions.....	137
Chapter 6: Low Concentration Surfactant Impacts on Red Blood Cell Membrane Integrity and Cellular Viability	140
6.1. Introduction.....	140
6.2. Materials and Methods	141
6.3. Results and Discussion.....	142
Chapter 7: Conclusions and Future Works	146
7.1 Introduction.....	146
7.2 Biocompatibility Change in Spatially Non-uniform AC DEP	147
7.3 Interactions Between Biological Cell and DEP Medium Additives	149
7.4 Utilize Dielectrophoresis-Based Microfluidics in its Full Capacity.....	151

7.5 Contribution of Our Work to Dielectrophoresis Field	153
References	156
Letter of Permission	170
A.1 Letter of Permission for Reference [33] (Chapter 1).....	170

List of Figures

Figure 1-1: The electric field (V/m) distribution in the microfluidic chamber. The non-uniform distribution	7
Figure 1-2: Classification of DEP devices according the microelectrodes configuration.	14
Figure 2-1: Schematic of surface-induced electric double layer. The electrode is shown in yellow.....	32
Figure 2-2: Schematic of a surfactant molecule and subsequent assembly into micelles..	36
Figure 3-1: Microdevice designs.	53
Figure 3-2: Electrical/material configuration in (a) uncoated microdevice and (b) HfO ₂ coated microdevice	57
Figure 3-3: Intensity analysis of video microscopy images from the T-shaped microdevice to obtain a normalized intensity (I_i) and subsequent final hemolysis, H_f , for RBCs diluted to 1.0 v/v %	60
Figure 3-4: For T-shaped microdevices, (a) impedance, $Z[k\Omega]$, and (b) current, $I[\mu A]$, plotted as a function of frequency.....	62
Figure 3-5: Time sequence of 1.0 v/v% red blood cells in 0.1 S/m isotonic PBS at 0.10 $V_{pp}/\mu m$ and 1 kHz applied potential for parallel (uniform), T-shaped (non-uniform), and star-shaped (non-uniform) electrode configurations.....	64

Figure 3-6: Comparisons between normalized intensity (I_i) with respect to time for T-shaped (left column) and star-shaped (right column) microdevices at 1kHz.	67
Figure 3-7: Hemolysis experiments were conducted at $0.10 \text{ V}_{pp}/\mu\text{m}$ and 1kHz ($n \geq 5$)	71
Figure 3-8: Optical images of T-shaped electrodes for both uncoated (a and b), and HfO_2 coated (d and e) electrodes before and after ~ 15 experiments at $0.10 \text{ V}_{pp}/\mu\text{m}$ and 1 kHz	72
Figure 4-1: Microfluidic device configuration with a PDMS fluidic layer bonded on a Cr/Au electrode glass slide	90
Figure 4-2: (a) The impact of 0.00, 0.07, 0.11, 0.17, and 0.50 mM Triton X-100 on percent hemolysis.....	92
Figure 4-3: UV-Vis absorbance spectra of 0.25 v/v% RBC/PBS from 250 to 750 nm.....	95
Figure 4-4: Video microscopy images illustrating the time sequence of 1.0 v/v% red blood cells in 0.1 S/m isotonic PBS medium.....	100
Figure 4-5: Dielectrophoretic force as function of frequency from 300 to 700 kHz.	101
Figure 5-1: Microfluidic device configuration with a PDMS fluidic layer.....	121
Figure 5-2: Time sequence of PK-13 cells in 0.1 S/m isotonic phosphate buffer saline at $0.1 \text{ V}_{pp}/\mu\text{m}$ with frequencies from 0.9 MHz to 0.1 MHz.....	126
Figure 5-3: Cell's dielectrophoretic response, R_c (%) stacked into a column chart for PPV-infected PK-13 cells (a) before and (c) after glycine treatment.	128

Figure 5-4: Trypan blue staining in PK-13 cells (a) before and (b) after PPV infection at $t=10$ hours.	129
Figure 5-5: Dielectrophoretic force spectra of untreated (first column) and glycine-treated (second column) PK-13 cells post infection as function of frequency 0.9 to 0.1 MHz...	131
Figure 5-6: The box-and-whiskers-plots of cell radii for non-infected (controls) and PPV-infected (a) before and (c) after glycine treatment.....	134
Figure 6-1: Histogram and overlaid normal/Gaussian distribution line of normalized intensity density.....	143

List of Tables

Table 2-1: Lysis applications of dielectrophoresis-based microfluidic devices for cellular analysis in the literature.	24
Table 2-2: Summary of cell membrane capacitance studies in the literature.	28
Table 2-3: Faradaic reaction detection in microdevices involving pH changes	34
Table 4-1: Optimized parameters for single-shell oblate DEP polarization model for 0.00, 0.07, 0.11, and 0.17 mM treated RBCs in 0.1S/m isotonic PBS	105

Preface

The subject of this dissertation is exploring the role and impact of microscale phenomena on electrode, microdevice, and cellular function. Dielectrophoresis was utilized as a unique characterization technique within this dissertation. The aim of this work is to optimize the performance of dielectrophoresis-based microdevices. Many individuals have made contributions to the chapters found within this dissertation. I would like to give a special thanks to my Ph.D. advisor Dr. Adrienne Minerick for her critical feedback with experimental design, data collection and analysis, and manuscript editing. I would like to thank Dr. Hwi Yong and Dr. Hector Mocada-Hernandez for providing critical feedback on experimental design, data collection, and manuscript for Chapters 3 and 4. I would like to graciously thank Dr. Caryn L. Heldt for providing me with porcine kidney cells and porcine parvoviruses to collect all data in Chapter 5. She also provided critical feedback with experimental design and data interpretation. I would like to thank Pratik U. Joshi and Xue Mi for their effort in sample preparation, data collation, and data interpretation for Chapter 5. I collected and analyzed all of the human red blood cell data in Chapter 3 and 4, and collected and analyzed the porcine kidney cell data in Chapter 5. I wrote and edited Chapters 1-6 in this dissertation, and I am the first author of the future publications based on Chapters 3, 4, and 5.

Acknowledgments

I would like to express my gratitude to my Ph.D. advisor, Dr. Adrienne Minerick for all her inspiration, guidance, and support during the past five years. Dr. Minerick's passion for research has been a great motivation for me to conduct research and pursue my future career goals. Her professionalism and ethics in the engineering profession will be lifelong lessons.

I gratefully thank Dr. Caryn Heldt, who not only served on my dissertation committee, but she has been also a wonderful counselor and mentor for me. She has always given me novel ideas for my research, and valuable advice for my future career. My special thanks go to Dr. Tony N. Rogers and Dr. Smitha Rao who agreed to serve on my dissertation committee and provided me with valuable inputs to improve my dissertation quality.

I would like to thank several individual colleagues at Michigan Technological University, who have provided both encouragement and technical help during the course of my Ph.D.: Dr. Meysam Razmara, as one of my best friends, Dr. Hector Mocada-Hernandez and Dr. Hwi Yong for helping me to build up my professional skills, and Dr. Jeana Collins for her technical writing comments. I would like to acknowledge my dear friends: Nasim Azimi, Atefeh Farajollahzadeh, Atefeh Tarahi, Yasaman Behbahani, Bahareh Bakhshi, Nilufar Bakhshi, Masoumeh Alirezaei, Arash Jamali, and Amirhossein Hosseini.

My family holds a special place in my heart. I would like to thank my husband, Mohammad Reza, for his kind support, love, and encouragement during the past five years. I owe deep gratitude to my dear mother, Shahnaz, and my father, Reza, you two are my biggest cheerleaders. Maman Shahnaz and Baba Reza, you have always given me the courage to work hard and achieve my goals in life, I love you with all of my heart. I would like to thank my sister, Sahar, you are my role model, my friend, and the best sister anyone could ever have. I would like to also thank my little sister, Sadaf, you always know how to cheer me up. I would like to thank my grandmother, Sephora, and my grandfather, Shabanali, you always hold a special place in my heart. Finally, I would like to thank my mother-in-law, Molouk, and my father-in-law Jamal for their encouragement and support.

Abstract

Microfluidic technologies enable the development of portable devices to perform multiple high-resolution unit operations with small sample and reagent volumes, low fabrication cost, facile operation, and quick response times. Microfluidic platforms are expected to effectively interpret both wanted and unwanted phenomena; however, a comprehensive evaluation of the unwanted phenomena has not been appropriately investigated in the literature. This work explored an attenuative evaluation of unwanted phenomena, also called here as secondary phenomena, in a unique approach.

Upon electric field utilization within microfluidic devices, electrode miniaturization improves device sensitivity. However, electrodes in contact with medium solution can yield byproducts that can change medium properties such as pH as well as bulk ion concentration and eventually target cell viability. While electrode byproducts are sometime beneficial; but, this is not always the case. Two strategies were employed to protect cells from the electrode byproducts: (i) coating the electrodes with hafnium oxide (HfO_2), and (ii) stabilization of the cell membrane using low concentration of Triton X-100 surfactant. Our results showed that both strategies are plausible way to selectively isolate cell and reduce the risk of contamination from electrode byproducts.

The design of a medium solution is also critical to minimize the unwanted cell-medium interaction. Surfactants are frequently added to cell-medium solutions to improve sensitivity and reproducibility without disrupting protein composition of cell membranes or cell viability. In non-electrokinetic systems, surfactants have been shown to reduce interfacial tensions and prevent analyte sticking. However, the impacts of

surfactant interactions with cell membranes have not previously been explored in electrokinetic systems. This work indicated the dynamic surfactant interactions with cell membranes which altered the cell membrane integrity. It is important that the effects of the chemical interactions between cells to be fully explored and to be separately attributed to reported cellular responses to accurate catalog properties and engineer reliable microfluidic electrokinetic devices.

Finally, a comprehensive level of understanding led us to utilize dielectrophoresis in its full capacity as a tool to monitor the state and progression of virus infection as well as anti-viral activities of regenerative compound. Glycine was utilized as potential antiviral compounds to reduce porcine parvovirus (PPV) infection in porcine kidney (PK-13) cells. Our results demonstrate that the glycine altered the virus-host interactions during virus assembly. Thus, elucidating the mechanisms of these novel antiviral compounds is crucial to their development as potential therapeutic drugs.

Chapter 1: Introduction and Outline

1.1 Introduction

Our knowledge of fundamental biological processes including genetic sequences, proteomic distributions, and cellular traits has been influenced enormously by the usage of electric fields at the microscale level because the fields can manipulate and reproducibly distinguish charged cells, proteins, DNA, and other molecules [1]. Electrokinetics at the microfluidic scale are attractive due to their advantages of low fluid volume consumption, low cost, rapid analysis, and high resolution to perform quantitative chemical analysis, medical diagnosis, infectious disease detections, genetic abnormality detections, and other biomedical science applications [2-10]. A noteworthy application of electrokinetic microfluidic platforms is in biomedical science in numerous areas of diagnosis, therapeutics, and drug discovery [11-15]. Despite advancements, electrokinetic microfluidic reliability has not yet achieved that of lab-scale analytical tests. Reliable electrokinetic microfluidic platforms require deliberate experimental design elements to protect analyte integrity along with device functionality. Electrokinetic microfluidic devices aim to discern molecular and cellular level differences with the assumption that medium conditions around the target analyte are stable with respect to pH, ionic concentration and ionic strength, and that the medium has minimal interactions with the analyte (e.g. cell, (bio)molecule). Previous studies suggest that these constant condition assumptions are inaccurate and that undesirable secondary phenomena can occur within microfluidic systems over operational timescales [16-19]. To accurately catalog analyte

properties and engineer reliable electrokinetic microfluidic devices, each phenomenon should be separately interrogated to then discern impact on microdevice performance and reported cellular responses. This work outlines systematic efforts to quantify these secondary, time-dependent microdevice medium changes to more fully understand secondary phenomena influencing microscale electrokinetic responses. Thorough understanding of these molecular and cellular charge interactions will enable precise control of results within microdevices for subsequent DNA, protein, cell and other separations and analysis.

1.2 Microfluidics and Electrokinetics

Microfluidics is a technology developed to manipulate small volumes of fluids and small numbers of molecules using channels and chambers with dimensions of tens to hundreds of micrometers. Microfluidics can perform precise experiments quickly and at low cost; the technology emerged at the beginning of the 1980s for different applications such as inkjet printheads, DNA microchips, micro-propulsion, micro-thermal technologies, as well as lab-on-a-chip (LOC) technologies [20]. The use of electric fields [21] and integrated circuit fabrication technologies has greatly influenced the rapidly emerging field of microfluidics.

Electrokinetic microfluidic applications are widely advantageous since they only require electric fields to perform chemical reactions, chemical analysis, and cell or particle concentration, manipulation, separation, and detection [22]. The following is a brief overview of electrokinetic phenomena with an emphasis on the subsets most related

to this research project; electrophoresis [23], electro-osmosis [24], streaming potential and current [25], capillary osmosis [26], diffusiophoresis [27], sedimentation potential [28], and dielectrophoresis [22]. *Electrophoresis* describes the motion within an aqueous environment of charged collided particles or polyelectrolytes in a response to an externally applied electric field, most commonly direct current (DC) [23]. *Electro-osmosis* describes the movement of liquid, adjacent to a charged surface, induced by an electric field; the charged surface can be microchannel or capillary walls, porous bodies, immobilized particle beds, monoliths, or membranes and the electric field can be DC or alternating current (AC) [24]. The phenomena corollary is *streaming potential or current*, which describes the electrical potential or current generated by fluid moving, due to a pressure gradient, across a charged capillary tube, porous body, or membrane [25]. *Capillary osmosis* describes the motion of liquid under the influence of a chemical potential gradient [26]. *Diffusiophoresis* describes particle motion in response to an existing diffusion (or concentration) gradient [27]. *Sedimentation potential* is the electric field generated as a result of settling colloid particles in a suspension under the effect of gravity [28]. *Dielectrophoresis* (DEP) describes the complex motion of dielectric particles or cells under the influence of spatially non-uniform electric fields (either DC or AC). In this technique, particle polarizations result in a net force on the dielectric particles that causes motion up or down electric field gradients [22]. DEP can compete against other microfluidic methods since it can selectively manipulate a target particle based on its intrinsic dielectric polarizability. Simultaneously, non-target particles experience negligible dielectric polarizations and thus negligible forces. Each of these

phenomena do not exist only in isolation. Complex behaviors are observed when one phenomenon is triggered and influences secondary and tertiary phenomena within the microdevice and media.

The following sections in this chapter discuss general concepts of dielectrophoresis, as well as these other electrokinetically-driven microfluidic phenomena, and the motivation for further fundamental research into these areas. This introduction chapter concludes with an outline of the remainder of this dissertation.

1.3 Polarization Mechanisms

Dielectrophoresis depends on fundamental properties of the particles/cells and the surrounding medium polarization mechanisms [22, 23]. Under both uniform and non-uniform electric fields, both the particles and the suspending medium polarize, resulting in induced effective moments around the particle. Applied electric fields polarize the different dielectric particles differently yielding charge at all interfaces. Opposite charges ($+Q$ and $-Q$) move to either side of the particle, leading to a net-induced effective dipole moment. This dipole moment depends on the applied electric field frequency as well as the dielectric mismatch between the particle and the medium [22, 23]. The induced dipole moment is given by:

$$p = Qd \tag{1-1}$$

where p is the dipole moment and d is the particle diameter. When the applied electric field is uniform, equal but opposite forces are generated around the particle causing no net particle movement. In non-uniform electric fields, the charges induced on either side

of the particle are unequal and yield a net particle charge. As a result, the particles' dipole and the spatial gradient of the non-uniform electric field interact such that the dielectrophoretic force induces particle motion along the electric field gradient. Dielectrophoretic force, as a function of dipole moment and electric field gradient, is given by:

$$\vec{F}_{DEP} = (p \cdot \vec{\nabla})E \quad (1-2)$$

where \vec{F}_{DEP} is the dielectrophoretic force, the symbol $\vec{\nabla}$ is the differential operator for a gradient, and E is the electric field [22, 23].

1.4 Dielectrophoretic Phenomena

Dielectrophoresis (DEP) is a fundamental, leverageable pillar of microfluidic particle manipulation. Knowledge of this phenomena has advanced considerably over the last 20 years [22]. Dielectrophoresis is a powerful technique to manipulate particles in a non-uniform electric field. Ideal, perfect dielectric particles carry zero net charge; however, nonideal particles like biological cells can act like dielectrics, yet carry net charge on their membranes. When subjected to an external electric field, the particle undergoes a shift in distribution of the positive and negative charges from the resting equilibrium distribution causing dielectric dipole polarization. Particle size impacts how quickly charge distributions can shift and as a consequence the polarization phenomena is frequency dependent. Spatially non-uniform AC polarization creates a dielectrophoretic force on the particle (\vec{F}_{DEP}), which is described by the following relationship [22, 23]:

$$\vec{F}_{DEP} = 2\pi r^3 \epsilon_m \text{Re}[f_{CM}] \nabla E_{rms}^2 \quad (1-3)$$

where, r is the radius of the particle, ε_m is the permittivity of the medium, $\text{Re}[f_{CM}]$ is the real component of Clausius–Mossotti factor, and $\nabla \vec{E}^2$ is the electric field gradient squared [22, 23]. The Clausius–Mossotti factor (f_{CM}) describes particle’s polarizabilities and can be defined as:

$$f_{CM} = \frac{\varepsilon_p^* - \varepsilon_m^*}{\varepsilon_p^* + 2\varepsilon_m^*} \quad (1-4)$$

where ε_p^* and ε_m^* are the complex permittivity of the particle and medium, respectively. The complex permittivity can be further described via $\varepsilon_i^* = \varepsilon_i + \frac{\sigma_i}{j\omega}$, where ε_i is permittivity, σ_i is conductivity, ω is angular frequency, and j is imaginary number, while the subscript i refers to particle ($i = p$) and medium ($i = m$). The permittivity [F/m] is the summation of the substance polarization and the residual electric field and is given by $\varepsilon = \varepsilon_0(1 + \chi_e)$. The vacuum permittivity (ε_0) can be approximated as $\varepsilon_0 = 8.85 \times 10^{-12}$ F/m. The electric susceptibility (χ_e) is a dimensionless constant which shows the substance’s dielectric polarization degree in response to the electric field, while the conductivity [S/m] is the substance’s ability to conduct the current. Thus, the complex permittivity is a function of the conduction and dielectric energy losses of the particle and medium, as well as the frequency of the polarizing electric field.

The f_{CM} is essential to the understanding and application of dielectrophoresis. Thus, it is important to understand the physical principles of f_{CM} . The f_{CM} shows that the complex permittivity is frequency dependent, with low frequencies amplifying conductivity-driven effects while high frequencies intensifying permittivity-driven

effects. Figure 1-1 shows the electric field distribution within a simple non-uniform electrode configuration. The non-uniform electric field distribution is altered by the presence of a dielectric particle. The particle experiences an electric field gradient within its body, which is unique from the spatial gradient caused by the electrode configuration. Moreover, since permittivity describes how easily a dielectric is polarized in response to an electric field, this property determines the extent of the particle's induced dipole. The word stem “permit” in permittivity relates to a material's ability to resist electric flux.

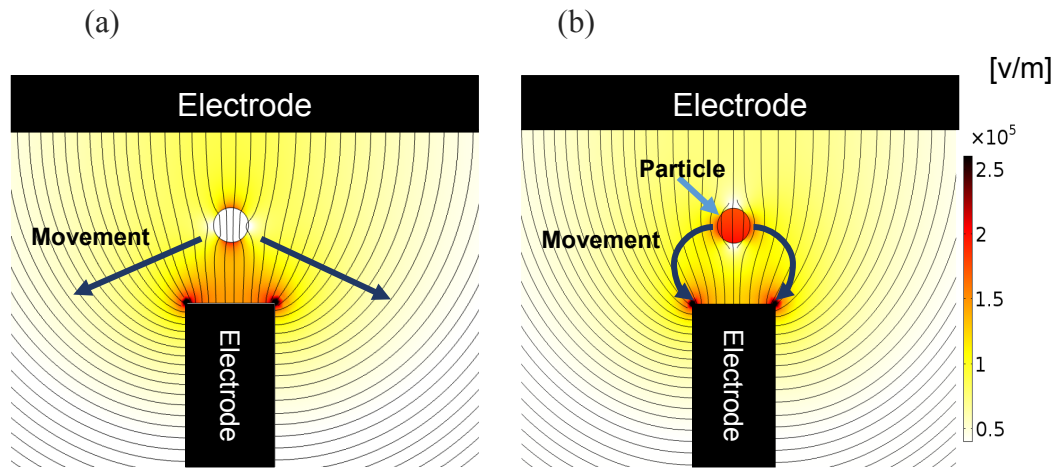


Figure 1-1: The electric field (V/m) distribution in the microfluidic chamber. The non-uniform distribution of particle charges generates a net DEP force that either moves the particle towards lower electric field gradient regions called (a) negative DEP (n-DEP) or moves the cell toward higher electric field gradient regions called (b) positive DEP (p-DEP). The color map shows the electric field gradient with the darkest red indicating the largest gradient and white indicating the lowest gradient. Overlaid electric field lines which can be envisioned as pathways for charge and electron flow between the electrodes.

This resistance to charge manifests into motion in electric field gradients. If the permittivity of the particle is lower than that of the medium, the particle shows less resistivity to the electric field and the electric field lines can pass through the particle (shown in Figure 1-1-a). On the other hand, if the permittivity of the particle is higher than that of the medium, the particle shows resistance to the electric field; therefore the

electric field lines cannot pass through the particle (shown in Figure 1-1-b). In equation (1-4), when a particle's complex permittivity is less than the medium ($\epsilon_p^* < \epsilon_m^*$), the direction of the net force is toward regions of minimum electric field strength, which is known as negative-DEP (n-DEP). On the other hand, when a particle's complex permittivity is greater than that of the medium solution $\epsilon_p^* > \epsilon_m^*$, net force direction is toward maximum electric field strength regions, which is known as positive-DEP (p-DEP) [22, 23]. Dielectrophoresis has been used to determine the DEP crossover frequency (f_{co}) where the dielectrophoretic (DEP) motion makes the transition from n-DEP to p-DEP or p-DEP to n-DEP.

Since equations (1-3) and (1-4) do not account for cellular structure such as the membrane and cytoplasm, these equations do not accurately represent a cell's DEP behavior. Key equations have been developed to model the polarization responses of cells within electric fields. A cell's polarization can be described based on cell size, shape, and dielectric properties. Cell shape is a critical parameter affecting interfacial polarization. A variety of cellular shapes can be represented using existing DEP polarization model equations, and cellular complexity can be added to account for cellular components (e.g. membrane, cytoplasm, and nucleus). The most common cell shapes modeled are single-shell spherical and single-shell oblate geometries since these model account for the cell membrane (shell) and cell cytoplasm. Thus, the following section will focus on the single-shell spherical and single-shell oblate DEP polarization model.

1.4.1 Single-Shell Spherical DEP Polarization Model

The single shell spherical DEP polarization model is more precise model, which modifies the cell's complex permittivity by incorporating the intrinsic effects of the cell membrane and cytoplasm. When in suspension, mammalian cells such as porcine kidney cells have a spherical geometry. For a sphere with a radius of r and membrane thickness of d , the effective complex dielectric permittivity ε_c^* as a function of cell components [29] can be described in a ratio metric fashion:

$$\varepsilon_c^* = \varepsilon_{mem}^* \frac{\left(\frac{r}{r-d}\right)^3 + 2\left(\frac{\varepsilon_{cyto}^* - \varepsilon_{mem}^*}{\varepsilon_{cyto}^* + 2\varepsilon_{mem}^*}\right)}{\left(\frac{r}{r-d}\right)^3 - \left(\frac{\varepsilon_{cyto}^* - \varepsilon_{mem}^*}{\varepsilon_{cyto}^* + 2\varepsilon_{mem}^*}\right)} \quad (1-5)$$

where ε_{mem}^* is the complex permittivity of the membrane, and ε_{cyto}^* is the effective complex permittivity of the cytoplasm. In most DEP applications, the most vital experimental parameter is the identification of operating frequency. The complex permittivity of the cell depends on frequency and can be characterized by the α , β , and γ dielectric dispersion regions ($\omega_\alpha < \omega_\beta < \omega_\gamma$). The first low-frequency dispersion is termed as α -dispersion and appears in the frequency range 10 Hz to 10 kHz. The second low-frequency is called β -dispersions and ranges from 10 kHz to 10 MHz. Maxwell-Wagner interfacial polarizations govern cell responses at the β -dispersion region whereby the cell's dielectric dispersion is affected by their membrane. At frequencies above 10 MHz, the electrical properties of the cell are dominated by the cell's cytoplasm.

As the DEP force changes polarity, cell's dielectric properties can be estimated from the crossover frequency (f_{co}) along with other data points from the DEP spectra. This

zero-polarization state at the crossover frequency can be calculated by setting $\text{Re} [f_{CM}]$ equal to zero in equation (1-4):

$$f_{CO} = \frac{1}{\sqrt{2}} \frac{\sigma_m}{\pi r C_{mem}} \sqrt{1 - \frac{r G_{mem}}{2 \sigma_m} - 2 \left[\frac{r G_{mem}}{\sigma_m} \right]^2} \quad (1-6)$$

where C_{mem} and G_{mem} are the cell membrane capacitance and conductance, respectively [29]. Membrane capacitance is a measure of the membrane area that acts as a charge barrier, which reflects the membrane thickness, composition/dielectric properties, and morphological complexity. Membrane conductance, on the other hand, reflects the net transport of ionic species across the membrane through pores, ion channels, and defects under the influence of the applied field. The practical applications of observing f_{CO} to then calculate membrane properties include being able to determine the dielectric property shifts of the cell resulting from apoptosis, cell differentiation, or others. In equation (1-6), the medium properties such as pH, ionic concentration and ionic strength are treated as constants. Since dielectrophoresis-based microfluidics devices manipulate nano/microliter sample volumes, the finiteness of ions within the system can dominate responses if sufficient buffer is not present to maintain local ion equilibrium. Previous studies suggest that constant medium assumption is inaccurate and that undesirable secondary phenomena can occur within microfluidic systems over operational timescales [16-19]. Thus, reliable results require careful experimental design.

1.4.2 Single-Shell Oblate DEP Polarization Model

Polarizable particle shapes can distort the electric field around them. As cell shapes deviate from spherical, the spherical single-shell model accuracy decreases. For example,

human red blood cells (RBCs) is known to be biconcave disk. A biconcave disk is a geometric shape resembling an oblate structure. Treating the cell geometry as an oblate spheroid with a long semi-major r radius and a semi-minor c radius, where c is the cell height ($r > c$), the DEP force expression is [30, 31]:

$$\vec{F}_{DEP} = \frac{3}{2} V_c \epsilon_m \text{Re} [f_{CM}] \nabla \vec{E}_{rms}^2 \quad (1-7)$$

where V_c is the cell volume and the f_{CM} is [30, 31]:

$$f_{CM} = \frac{\epsilon'_p - \epsilon_m^*}{3A_{oc}\epsilon'_p + 3(1-A_{oc})\epsilon_m^*} \quad (1-8)$$

A_{oc} represents the outer cell (OC) membrane depolarization factor which reflects the effects of cell shape on interactions with and distortions to the local electrical field. As discussed above, each interface accumulates charge such that the inner cell membrane (IC) and OC membrane depolarization factors are necessary to determine the effective complex permittivity of an oblate spheroid single-shell particle in a non-uniform electric field as follows:

$$\epsilon'_c = \epsilon_{mem}^* \frac{\epsilon_{mem}^* + (\epsilon_{cyto}^* - \epsilon_{mem}^*)[A_{IC} + v(1-A_{OC})]}{\epsilon_{mem}^* + (\epsilon_{cyto}^* - \epsilon_{mem}^*)[A_{IC} - vA_{OC}]} \quad (1-9)$$

where A_{IC} is the inner cell membrane depolarization factor, and v is volume ratio of cell outer to inner membrane $v = r^2 c / [(r + d)^2 (c + d)]$. For an oblate spheroid, the inner and outer membrane depolarization factor is:

$$A_{OC} = A_{IC} = -\frac{\gamma^2}{2(1-\gamma^2)} + \frac{\gamma\pi}{4(1-\gamma^2)^{1.5}} - \frac{\gamma}{2(1-\gamma^2)^{1.5}} \left[\text{Arctan} \left(\frac{\gamma^2}{1-\gamma^2} \right)^{0.5} \right] \quad (1-10)$$

where $\gamma = c/r$ for inner membrane depolarization, and $\gamma = (c + d)/(r + d)$ for outer membrane depolarization. For a spherical particle/cell, $\gamma = 1$ and $A_{OC} = 0.33$, in which

case equation (1-8) reduces to the familiar f_{CM} expression for spherical particles (1-4). RBC membranes have been determined to be less conductive than the cytoplasm [30]. Under these conditions, by setting $\text{Re}[f_{CM}] = 0$ in equation (1-8) results in the crossover frequency, as follows [32]:

$$f_{CO} = \frac{A_{OC}}{2\pi b r C_{mem}} \sqrt{\left[\sigma_m - \frac{b r G_{mem}}{A_{OC}} \right] \times \left[\frac{1-A_{OC}}{A_{OC}} \sigma_m + \frac{b r G_{mem}}{A_{OC}} \right]} \quad (1-11)$$

where $b = c / (2c + r)$ [32]. As equations (1-6) and (1-11) demonstrate, f_{CO} provides a means for monitoring localized changes in cell membrane capacitance and conductance. Thus, measuring cell DEP behavior can infer cell dielectric properties, which can then be utilized to characterize, compare, and separate cells of interest. The measurement of cell behaviors requires reproducible control of electric field gradients. This research uses orthogonal T-shaped electrodes and four pairs of converging triangular electrodes (star-shaped electrodes) to achieve electric field gradients to interrogate cells. There are various electrode arrangements to generate a non-uniform electric field which will be further discussed in this chapter.

1.4.3 Mammalian cells

Dielectrophoresis is a popular choice for manipulation of bacteria, yeast, and mammalian cells. Our work mainly focuses on mammalian cells such as porcine kidney cells (PK-13) and human red blood cells (RBCs). Mammalian cell such as PK-13 are generally grown in vivo, outside their natural environment. The process of growing cells is called cell culture. In cell culture, cells are grown under controlled conditions at an appropriate temperature and gas mixture (typically, 37 °C, 5% CO₂ for mammalian cells)

in a cell incubator. Unlike complicated PK-13 cell preparation process, red blood cell can be collected through simple blood donation. DEP behavior of both mammalian cells will be discussed in the second chapter.

1.5 Types of Dielectrophoresis Electrode Designs

Dielectrophoresis can be produced either in direct current (DC) or alternating current (AC) systems because the electric field gradient in equation (1-1) is not frequency dependent. Briefly, DC systems generate and distribute electrical charge flow in one direction while the AC charge flow direction oscillates back and forth. Depending upon the desired application, either DC or AC can be selected. In both DC-DEP and AC-DEP, spatially non-uniform electric fields can be generated via microelectrode or insulator geometries including parallel or interdigitated, castellated, oblique, curved, quadrupole, microwell, matrix, extruded, top-bottom patterned, and side wall patterned (Figure 1-2) [33]. Each of these cause spatial variations (e.g. curvatures) in the electric field. An advantage of AC-DEP over DC-DEP is the prevention of Joule heating at lower voltages. Joule heating is an undesirable phenomenon because it can cause secondary electrokinetic flow due to unwanted local temperature increases, convection, bubble generation, and sample degradation [34]. However, Joule heating effect is desirable for some applications, i.e. polymerase chain reactor (PCR) [35], pH gradient [36], and temperature gradient generation across a microchannel [37]. For this project, AC dielectrophoresis-based microfluidic platform is preferred due to the low operating voltage which prevents water electrolysis and thwarts impacts from Joule heating.

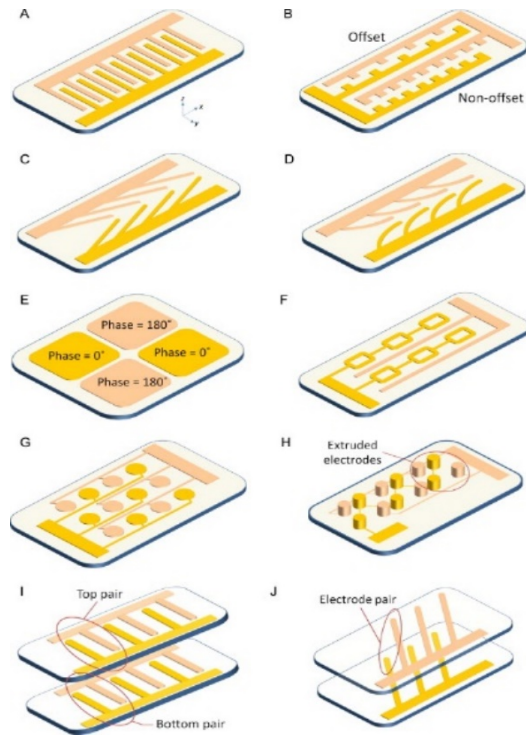


Figure 1-2: Classification of DEP devices according to the microelectrodes configuration. (A) parallel or interdigitated, (B) castellated, (C) oblique, (D) curved, (E) quadrupole, (F) microwell, (G) matrix, (H) extruded, (I and J) top–bottom patterned, (K) sidewall patterned, (L) insulator-based or electrodeless, and (M) contactless. Copied with permission [33].

1.6 Implemented Material within Dielectrophoresis-based Microfluidic Systems

Dielectrophoresis also depends on fundamental properties of the material implemented within microfluidic systems. A variety of material such as conductors and dielectrics are utilized in the dielectrophoresis-based microfluidic device. Conductors are generally utilized to fabricate metal-based microelectrode arrays in specific geometries. Many materials such as platinum, gold, stainless steel, tungsten, iridium oxide and titanium nitride have been used to fabricate the microelectrodes [16, 17, 38, 39]. On the other hand, dielectric thin films are used to coat over the microelectrode surfaces as passivation layers to reduce ion production, redox reaction (e.g. Faradaic reactions), and

electrode surface fouling [16, 17, 40, 41]. The most common dielectric thin film coating materials are silicon dioxide (SiO_2), silicon nitride (Si_3N_4), lanthanum oxide (La_2O_3), lanthanum aluminate (LaAlO_3), aluminum oxide (Al_2O_3), Zirconium dioxide (ZrO_2), titanium dioxide (TiO_2), cerium oxide (CeO_2), and hafnium silicate (HfSiO), and hafnium oxide (HfO_2) [42-45]. In the dielectrophoresis-based microfluidic device, passivation materials should tolerate mechanical and chemical stresses and not interfere with the electric field characteristics [46].

A proper choice of conductive and dielectric materials is important for microfluidic device performance. Electrochemical Impedance Spectroscopy (EIS) is frequently utilized to distinguish the dielectric and electric properties of individual contributions of microfluidic device components [47]. Impedance spectroscopy is a non-destructive technique and can provide time-dependent information about the electrode processes and complex interfaces[48]. The electrochemical impedance method consists in measuring the response of an electrode to a sinusoidal potential modulation at different frequencies. The mathematical approach of electrochemical impedance data is based on the Ohm's law. Defining dielectric and electric properties of microfluidic device components can be utilized to accurately design experimental matrix.

1.7 Conclusions

This chapter described the basic theory of dielectrophoresis. Dielectrophoresis is without a doubt one of the mature and fundamental parts of the microfluidic manipulation. The continued advances in DEP technology has always been driven by

curiosity for potential practical applications. One of the primary applications of dielectrophoresis subject is in biomedical science. Current biomedical science applications of dielectrophoresis are directed towards characterizing the dielectric properties of biological material such as blood cells (e.g. RBCs) or pathogenic bioparticles (e.g. viruses). As was shown in equations (1-6) and (1-11), exploring the difference in the dielectric properties of the target cell manifests itself as a difference in the DEP crossover frequency, f_{CO} . Cell screening based on DEP crossover frequency has valuable biomedical applications in numerous areas of diagnosis, therapeutics, and drug discovery.

For most dielectrophoresis biomedical applications, the surrounding medium is an aqueous solution. As was shown in equations (1-3) and (1-4), medium solution properties are extremely critical in determining DEP force. The medium properties are typically presumed to be constant with having minimal influence on cell viability and membrane integrity. However, limited works have studied the legitimacy of this assumption [16-18, 49]. Previous studies suggest that these constant condition assumptions are inaccurate and that unwanted secondary phenomena can occur within microfluidic systems over operational timescales [16-19]. Knowledge of the extent to which these secondary phenomena alter the dielectric properties of the medium provides the means to accurately monitor DEP behavior. Examples of undesirable secondary phenomena include the following:

- Microfluidic devices have a large ratio of surface area to volume. Scaling down the dimensions creates the possibility for the target cell to quickly inherit the

properties of its microenvironment. Any changes in medium properties (e.g. pH, ionic concentration, and ionic strength) can influence the comfortable physiological state of medium for cells. In dielectrophoresis-based microfluidic systems, electrodes in contact with the medium solution can participate in redox reactions (e.g. Faradaic reactions) yielding byproducts that can change medium properties and eventually target cell membrane integrity as well as viability [16-19]. Unbalanced medium and high field gradient increase the risk of damage or stress-induced changes to cells. Knowledge of the extent to which unbalanced medium alter the cell is essential to accurately monitor or control the DEP behavior.

- At micro dimensions, computer-aided image analysis is usually employed to record cell movement for identification of DEP crossover frequency, f_{CO} . In medium solution, the suspended cells have the tendency for undesirable nonspecific adhesion to the microchip surfaces. This nonspecific cell adhesion to the microfluidic surface can reflect in cell movement and ultimately reduce the accuracy of the collected data. Commonly, chemicals such as surfactant are introduced to the suspending medium to reduce undesirable nonspecific adhesion [50-54]. Adding chemicals to the suspending medium can alter dielectric properties of the cells. Knowledge of the extent to which these chemicals alter the dielectric properties of the cell is essential to accurately monitor or control the magnitude DEP force and the f_{CO} .

In conclusion, the accuracy and reliability of dielectrophoresis-based microfluidic systems should not take for granted in biomedical applications. In this dissertation, this assumption is challenged by evaluating undesirable secondary phenomena within the medium and their possible impacts on cell viability and membrane integrity. This work provides a better understanding of these issues, which enables optimized process/microdevice design. To pursue this objective, the DEP biomedical science applications and current challenges and limitations were reviewed in the second chapter of this dissertation. Finally, at the end of the second chapter we proposed how to appropriately choose the experimental parameters.

Chapter 2: Dielectrophoretic Literature Review for Biomedical Sciences Applications

2.1 Introduction

Dielectrophoresis (DEP) is a fast, label-free, and low-cost technique that utilizes the polarization principles to generate particle/cell motion in non-uniform electric fields. This technique has proven to be beneficial in biomedical science application providing insights in both fundamental research and practical practices [11, 12]. The first proof that DEP could be useful in biomedical sciences application was the shown by Herb Pohl and Ira Hawk in 1966 [55]. Pohl and Hawk were able to discriminate and separate live and dead yeast cells at the same time using DEP technique.

As mentioned in previous chapter, cellular DEP behavior is attributed to unique differences in cell's dielectric properties and catalogued as if they are “finger-prints” or “cell-prints”. Briefly, ion movement around the cell membrane polarizes the cell due to the different charges inside and outside the cell membrane. The effect of the extracellular membrane biomarkers (e.g. membrane molecular marker expression) interaction with the medium can determine the dielectric properties of the cells by exploiting the crossover frequency, f_{CO} . The extracellular membrane biomarkers can be studied as an electrophysiological marker to diagnose disease, track disease progression, and help vet more tailored treatment strategies.[13-15].

Cellular analysis based on DEP forces are extremely dependent on medium properties as shown in equations (1-3) and (1-4). Accurate and reliable reading of DEP behavior requires deep knowledge and interpretation of both wanted primary and

unwanted secondary phenomena within the medium solution to develop a reliable dielectrophoresis-based microfluidic platform [16-19]. Undefined phenomena within the medium and their possible impacts on cell membrane integrity and viability can reduce the reliability of the microfluidic platform limiting its utility and applications in biomedical sciences. A broader list of potential biomedical applications exists than what Pohl and Hawk were able to demonstrate with yeast cells. The objective of this chapter is to outline the progress and development of biomedical science application of DEP field that has been accomplished over the past 53 years following by its current challenges and limitations.

2.2 Biomedical Science Applications

Fast and accurate disease diagnoses and monitoring can save lives. During the disease progression, there are certain complex alterations that occur within the cells ranging from changes in membrane molecular integrity to cell morphology. Diagnosing and screening the disease cannot be accomplished without an in-depth knowledge of the cell's physiological state, pathological condition, as well as any cyto-active agents to which the cell was exposed. Characterizing differences in cell properties between a healthy and pathological state can elucidate cell-driven mechanisms of a disease, which can lead to delivery of a more tailored treatment or cure. Over the past 53 years, many researchers have directed efforts to characterize healthy and infected/unhealthy cells in the various avenues of DEP technique described by Pohl and Hawk. [11, 12, 55-58].

The biomedical science applications discussed within this dissertation can be categorized into mechanisms associated with cell lysis [59-64] and membrane capacitance [13, 32, 65-71]. Cell lysis involves breaking the cell membrane so that the internal contents of the cells can be studied for cellular analysis, medical diagnosis, and treatment. Other biomedical science application is associated with cell membrane. A link between membrane capacitance and the cell's electro-physiological/pathological properties has been being established via DEP [13, 32, 65-71]. Both mechanism and their application in biomedical science are broadly studied in the literature. The following sections review published works related to cell lysis and membrane capacitance.

2.2.1 Cell Lysis

Utilizing intracellular contents such as proteins, organelles, DNA/RNA, etc. found and/or grown inside cells is closely integrated with drug development in the broad field of biomedical science. Cell lysis is a technique in which the cell membrane is broken to extract the intracellular components for the intended downstream applications [60-64, 72-76]. The cell contents can then be examined to study the chemical expression or distributions of metabolites (metabolomics), the expression of genetic traits (genomics), and the structure and function of proteins (proteomics). Cell lysis can be achieved using osmotic pressure differences [77], chemical [72], sonic [73], mechanical [74-76], electrochemical, and electrical techniques [59-64]. Osmotic lysis, or cytolysis, is a technique where the osmotic balance of the surrounding media is shifted to create an osmotic pressure imbalance across the cell membrane. Relatively sudden or extreme changes in the ionic conditions surrounding a cell can induce cytolysis [77]. Chemical cell

lysis is a relatively fast and convenient technique for generating both complete and fractionated cell lysates. However, this method leaves unwanted chemicals within the analytical fluid which can complicate downstream processing [72]. Sonication methods apply high frequency sound waves to a cell suspension and cells are lysed as a result of liquid shear and cavitation [73]. Mechanical approaches can be used to break up the membrane with physical instruments including nano-knives, filters, compression between flat plates, and beads/cells interacting on a microfluidic compact disk. Mechanical lysis requires a pump to achieve a pressure drop and complex fabrication techniques, which are disadvantages [74-76]. In electrochemical technique, lysis is achieved by applying electric field to electrochemically generate hydroxide ions, $[\text{OH}^-]$, inside the device. The produced hydroxide ions induce membrane permeabilization and cell lysis by cleaving fatty acids [78-82]. Traditional electrical lysis techniques include electroporation whereby a pulsed electrical field creates holes in cell membranes due to transmembrane potential distributions. A strong electric field can lead to membrane rupture and cell death. One newer electrical lysis method is dielectrophoresis (DEP), which has been studied by our group. Dielectrophoresis occurs when cells are strongly polarized in a non-uniform electric field and depending on the electric field strength, frequency, and time of exposure, membranes can be irreversibly damaged or experience lysis. Dielectrophoresis requires much lower potentials than electrical lysis, involves simpler fabrication and does not leave a chemical residue. The technique chosen for cell lysis must be compatible with the intended downstream applications.

Table 2-1 summarizes research progress on lysis applications with different microdevices, experiment conditions, and cell types for variety of intended downstream applications. Lin et.al [60] fabricated an optically-induced microfluidic device using dielectrophoresis to rupture an individual cell among a group of cells or lyse the cell membrane without damaging the nucleus [60]. Within the cell lysis device, the cell suspension was sandwiched between two glass substrates coated with indium-tin-oxide (ITO) film. The bottom ITO film was coated with an amorphous silicon layer as a photoconductive layer. When an AC signal was applied between the two ITO films, high electrical impedance was generated within the silicon layer. Then, the silicon layer was exposed to a light beam to excite electron-hole pairs. The excitation of the electron-hole pair led to electrical impedance reduction thus creating a non-uniform electric field [60]. One of the disadvantages of this system is that the ITO films are not electrochemically inert material and can participate in redox reactions (e.g. Faradaic reactions) in the presence of isotonic media solutions. Faradaic reactions degrade the ITO film such that it loses transparency over time. To address this issue, Ameri et al. [61] replaced the bottom ITO electrode with graphene for dielectrophoretic trapping and lysing RBCs. Graphene is an adequate electrochemically inert material with sufficient optical transparency if thin enough. While successful, the electrical and optical properties of graphene-based electrodes must be improved since they are still lower than those of the ITO electrodes.

Table 2-1: Lysis applications of dielectrophoresis-based microfluidic devices for cellular analysis in the literature. The bold font highlights red blood cells (RBCs) studies which is one of the cell models used in this dissertation.

DEP electrode configuration	Cell type	Electric field gradient [$V_{pp}/\mu m$]	Frequency [kHz]	Ref
Optically-induced electrodes	Fibroblast cells, Oral cancer cells	7	20	[60]
Optically-induced electrodes	RBCs	0.025	120	[61]
Saw-tooth electrodes(3d)	Carcinoma cells	0.2-0.3	5 -10	[62]
Castellated electrodes	Murine clonal cells, White blood cells	4 -10	1000-6000	[63]
Liquid electrode	Yeast cells	60, 80, and 100	300	[64]
T-shaped electrodes	RBCs	0.015, 0.03,0.06	1-10	[59]

Cell lysis was studied via dielectrophoresis-based microfluidics device in unpublished previous work in our group [59]. To investigate the overall hemolysis profiles, our previous group member has utilized 100 μm platinum wire electrodes in a T-shaped configuration to create the spatially non-uniform electric fields [59]. Important parameters potentially affecting the rupturing rate were studied: ABO antigen and Rhesus factor dependency, variation within donors, variation within devices, aging of the RBC samples, concentration dependency, electric field strength dependency, the effects of washing RBCs with phosphate buffer saline (PBS), and AC frequency dependence. The results showed that the hemolysis was mainly influenced by frequency and strength of the electric field, with additional influences from ABO antigen and Rhesus factor. High-intensity as well as low-frequency alternating electric field resulted in higher hemolysis efficiency. Moreover, RBCs of B+ blood type ruptured 74% more than any other blood types [59]. This work is unpublished and provided to me by Dr. Kaela Leonard.

Applications from DEP phenomena are not limited to cell lysis. Cell membranes also carry various useful information about a cell's status. Cell membrane capacitance has been extensively described as one of the most informative parameters for monitoring cell physiological and pathological states. In the following section, the background and literature review on cell membrane capacitance is discussed.

2.2.2 Cell Membrane Capacitance

During the past 50 years, researchers have established a dependable link between membrane capacitance and a cell's physiological/pathological properties by using dielectrophoresis [13, 32, 65-71]. The study of cell membrane capacitance can investigate cell membranes which is an essential requirement for therapeutics and drug discovery researches.

The cell membrane is comprised of a phospholipid bilayer with interior and exterior surface proteins as well as transmembrane proteins that allow only certain molecules/ions to travel through the membrane [83, 84]. The cell membrane works as a barrier to regulate the movements of ions and molecules in- and outside the cell. Ions and molecules can passively diffuse through the cell membrane (slow), transfer in- or outside the cell via osmosis or experience active transport via transmembrane exchange proteins. Active transport is needed to move some molecules against their concentration gradient which requires energy consumption (ATP, NADP participating in redox reactions with the proteins) [83].

Membrane capacitance is a measure of the membrane area that acts as a charge barrier, which reflects the membrane thickness, composition/dielectric properties, and morphological complexity. Membrane barrier functionality can be discriminated between cells via DEP. Simply put, a living cell with active metabolic processes has a distinctly different dielectric signature than dead cells. The electric field perturbation depends upon the total charge capacity of the cell plasma membrane where its membrane area plays a major role in defining the membrane capacitance and DEP properties. The membrane area ($4\pi r^2$) of a perfectly smooth lipid bilayer with a spherical shape has a C_{mem} value of 6.3 mF/m². However, the experimental values obtained for a cell's C_{mem} are normally ranging from 1 to 30 mF/m² [13, 32, 65-71] as compiled in Table 2-2. The cell membrane capacitance closely correlates with the membrane effective area in direct contact with the surrounding medium. The presence of membrane folds and perturbation such as blebs and microvilli increase the effective membrane surface area, resulting in an increase in membrane capacitance. On the other hand, a decrease of the membrane capacitance can be caused by smoothing or stretching of a membrane [66]. Cell interrogations, via dielectrophoresis-based microfluidic device, reveal a wide range of information about a cell's physiological/pathological state.

Table 2-2 summarizes the cell membrane capacitance of bone cancer cells, prostate cancer cells, human oral cancer cells (CaLH3, H357, OSCC1, and DOK), human mesenchymal stem cells, mouse macrophage cells, human red blood cells, human hepatic fetal epithelial cells, and baby hamster kidney fibroblast cells. These cell systems were analyzed in different medium conductivity solutions ranging from 10 to 100 mS/m. Ismai

et al. [67] characterized human skeletal stem and bone cell populations using dielectrophoresis. A mixed population of two osteosarcoma cell lines (MG-63 and SAOS-2) and an immunoselected enriched skeletal stem cell fraction (STRO-1 positive cell) was explored to separate skeletal cell populations from heterogeneous bone marrow cell populations. The different cell membrane capacitance patterns of a mixed population [67] was confirmed by Huang et al. [68], who went onto separate cancer prostate cells via cell capture from peripheral blood mononuclear cells. Specific membrane capacitance values of 5.0 and 7.5 mF/m² were found for cancer prostate and peripheral blood mononuclear cells, respectively. Liang et al. [69] investigated the dielectric properties of human oral cells based on their adherence to collagen IV classified as rapid adherent cells (RAC), middle adherent cells (MAC), and late adherent cells (LAC). Rapid adherent cells (RAC) had rough surface membrane and cellular protrusions resulting in greater membrane capacitance than middle (MAC) and late (LAC) adherent cells. Adams et al. studied the human mesenchymal stem cells (hMSCs) at different DEP medium solutions conductivity (30 and 100 mS/m) for stem cell therapeutic applications. The membrane capacitances were found to be 1.0 and 1.3 mF/m², respectively [70]. Forero et al. [71] showed that leishmania amazonensis (a parasite) induced a significant increase in membrane capacitance of monocytes (J774.1), suggesting that parasite invasion leads to the addition of cell membrane surface area to the host cell.

Table 2-2: Summary of cell membrane capacitance studies in the literature. The bold font highlights the human red blood cells (RBCs) study which is one of the cell models used in this dissertation.

Cell Type	Application	σ_m [mS/m]	C_{mem} [mF/m ²]	Ref
Bone cancer	Identification of cancer cell heterogeneity	10.00	MG-63= 16.0 SAOS-2 =13.6 STRO-1= 10.7	[67]
Prostate cancer	Isolation of cancer cells from blood	70	Cancer cells= 5.0 Blood cells= 7.5	[68]
Human oral cancer	Identification of tumorigenic properties	10.00	CaLH3=23.0-18.0-12.0* H357=18.1-15.1-10.1* OSCC1=8.0-7.0-5.0* DOK=25.0-24.0-23.0*	[69]
Human mesenchymal stem	Separation of the stem cells for therapeutic application	30 100	1.0 1.3	[70]
Mouse macrophage	Characteristics of normal and lishmania amazonensis (parasite) infected cells	N/P**	Normal cells=15.6 Infected cells=21.2	[71]
HUMAN RED BLOOD CELLS (RBCS)	Characteristics of normal and malaria (parasite) infected cells	20.00	Normal cells= 11.8 Infected cells =9.0	[32]
Human hepatic fetal epithelial	Characteristics of normal and dengue (virus) infected	10.00	Normal cells =1.2 Infected cells =4.0	[65]
Baby hamster kidney fibroblasts	Characteristics of normal and herpes simplex virus type 1 infected cells	17.5	Normal cells=20.0 Infected cells=15.0	[13]

* The C_{mem} for human oral cancer is shown in the following sequence: RAC, MAC, and LAC.

** Not applicable.

Gascoyne et al. [32] indicated that malaria (parasite) increased the infected erythrocyte cell membrane capacitance. From measurements of the crossover frequency, values of 11.8 and 9 mF/m² were derived for the membrane capacitance of the malaria infected and normal cells, respectively [32]. The cell membrane alteration of normal and parasitized cells was considered a consequence of parasite-associated membrane pores in the parasitized cells [32, 71]. Normal and dengue-infected human hepatic fetal epithelial

cells were characterized based on their DEP crossover frequency [65]. The crossover frequency decreased from 220 kHz for the normal cells to 140 kHz after infection. This reduction in crossover frequency yielded an increase in cell membrane capacitance from 1.2 to 4.0 mF/m². This increase in membrane capacitance was due to alterations in cell size as well as cell composition as infection progressed. Archer et al. [13] characterized baby hamster kidney fibroblast cells before and after herpes simplex virus type 1 (HSV-1) infection as a function of time from infection. The non-infected cell's membrane capacitance was 20.0 mF/m², reducing to 15.0 mF/m² after 12 hours post infection [13].

In summary, DEP is a powerful technique to monitor, interrogate, and characterize a wide variety of cells as well as prepare them for downstream characterization. Most published works focus on positive attributes of DEP microfluidic systems. However, very few studies have been published regarding cell biocompatibility, consistency, reproducibility, accuracy, and design translatability of DEP performance [16, 17, 44]. As a result, microfluidics systems are facing challenges, which are discussed in the following sections.

2.3 Current Dielectrophoretic Challenges and Limitations

Dielectrophoretic-based microfluidic systems are promising platforms to implement diverse biomedical applications in both research and as field-implemented diagnostic platforms. However, each dielectrophoretic-based microfluidic system has limitations [85] which compromise their reliability. Cell population variation, pressure alteration, non-inert medium additives, and medium pH/ion alteration can limit the reliability of

dielectrophoretic-based microfluidic systems in biomedical application [85]. External pressure sources, valves, and plugs can be utilized to minimize cell population and pressure alteration. In this study our focus revolves around medium changes.

Scaling down the dimensions for cell analysis and manipulation accelerates the timescale for the target cell to experience the properties of its microenvironment. Any unwanted secondary phenomena within the medium can change the medium's physiological homeostasis (e.g. pH, ionic concentration, and ionic strength); consequently, analyte properties can change such as protein conformation or cell's membrane integrity [16, 17, 40, 41, 50, 52, 53, 86]. Cell membrane integrity can alter over time in response to secondary phenomena such as cell exposure to (i) the byproducts of electrode and medium redox reactions (i.e. Faradaic reactions) [16, 17, 40, 41] or (ii) medium additives [50, 52, 53, 86]. Thus, each microfluidic system should separately define and differentiate all of the possible secondary phenomena. In the following, two possible unwanted secondary phenomena within a medium (i) release of the Faradaic reaction byproducts [16, 17, 40, 41] and (ii) addition of medium additives [50, 52, 53, 86] are discussed.

2.3.1 Biocompatibility Change in Spatially Non-uniform AC DEP Fields

Despite the challenges outlined in the previous section, dielectrophoretic microfluidic systems are well-established platforms for fast and efficient cellular characterization. The major technical problem in DEP microfluidic systems that involves medium solution alterations during the experiment was shown by a previous member of

our research group to originate from electrodes at electrode/medium interfaces [16, 17]. The medium solution alterations during the experiment has been neglected for the vast majority of published DEP microfluidic systems resulting in unattributed biocompatibility challenges. There are two types of processes that can occur at the interface of an electrode/medium solution; non-Faradaic processes and Faradaic processes/reactions [87, 88]. In non-Faradaic processes, the electrode-medium interface works as a capacitor without any charge transfer. Adsorption and desorption are two examples of non-Faradaic process at the electrode-medium surface. Alternative Faradaic processes are based on charge transfer via electrochemical reactions at the interface between the electrode and the medium. Oxidation-reduction reactions at the electrode-medium surface are two examples of Faradaic processes [87, 88]. Faraday's law governs these Faradaic processes. A previous member of our research group showed that Faradaic processes can alter medium solution properties (e.g. pH, ionic concentration, and ionic strength) during the experiment. Thus, the following reviews will focus on Faradaic processes in electrokinetic-based microfluidic platforms.

When electric currents pass through the medium solution, Faradaic reactions can occur at the electrode and medium interface. Under AC potentials, Grahame [89] showed that Faradaic reactions occur within a thin layer which is known as an electrical double layer (EDL). Solid surfaces carry a net electric charge. When an aqueous solution is in contact with solid surface, counterions in bulk solutions are transferred toward the oppositely charged solid surface to create the electrical double layer (EDL). In the presence of the electric field, the EDL adjusts and settles to a new equilibrium. Figure 2-1

shows the formed electrical double layer at the surface of a negatively charged electrode as a result of external potential.

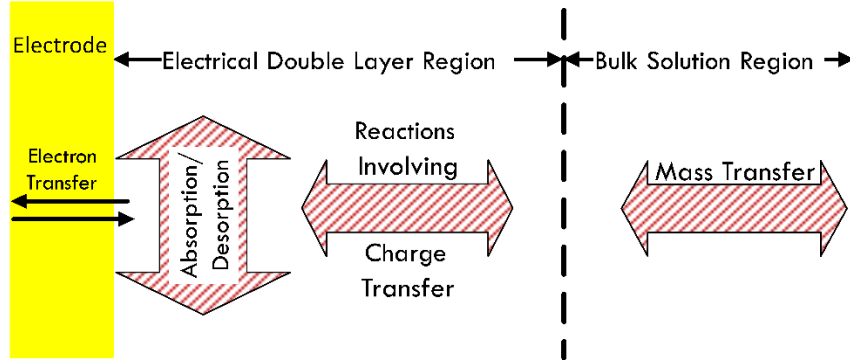


Figure 2-1: Schematic of surface-induced electric double layer. The electrode is shown in yellow. The electrical double layer is adjacent to the electrode. Charge transfer occurs within the EDL region during Faradaic Reactions.

As shown in Figure 2-1, Faradaic reactions include three main stages: (i) reactant migration (mass transfer) to the electrical double layer, (ii) the reaction, and (iii) product migration (mass transfer) away from the EDL through the bulk electrolyte. The EDL is a dispersed ion layer, with a thickness of a few nanometers. The EDL does not approach to the equilibrium condition instantaneously; the timescale for EDL formation and reformation is governed by ion transport. Ion oxidation/reduction occurs within the EDL during a finite electrode charging time, termed the characteristic charging time [18, 49]. Characteristic time (t_c) is the production of the typical resistance of bulk medium ($L/\sigma S$), and the capacitance of the EDL ($S\varepsilon/\lambda_D$) and is calculated as follows:

$$t_c = \frac{L\varepsilon}{\sigma\lambda_D} \quad (2-1)$$

where, ε is the fluid permittivity, σ is the conductivity, λ_D is the Debye length, and L and S are the system's characteristic length and area, respectively. The electrode charging

frequency (f_c) can be calculated according to the characteristic time (t_c) using $f_c = 1/t_c$. [49, 90]. Since the f_c is inversely If the applied frequency (f) is low and close to DC conditions ($f \ll f_c$), ions have enough time to migrate in and out of the EDL and charge it to its full capacity. Using sufficiently low frequency ($f \ll f_c$), the polarity period is so long the condition becomes similar to the DC case, thereby enabling EDL layer formation and Faradaic reactions. At higher frequencies ($f \gg f_c$), the polarity period is very short and not sufficient for ions to completely charge the EDL [16, 91]. According to the Grahame review, at very high frequency ($f \gg f_c$), the EDL is not well established and thus Faradaic reactions tend not to occur. At moderate frequencies ($f \approx f_c$), the EDL is partially established [89]. At frequencies close to the electrode charging frequency, Faradaic ion exchanges occur slowly resulting in a reduced Faradaic reaction rate; however, the extent of it and its impact on a cellular level is not fully explored in the literature.

In electrokinetic aqueous-based microfluidic systems, water electrolysis is often the most dominant Faradaic reaction as studied in previous works [92, 93]. In water electrolysis, pH changes are induced through formation of hydrogen ions [H^+] at the anode and hydroxide ions [OH^-] at the cathode. pH changes are induced by water electrolysis according to the following anode and cathode redox reactions:



In addition to water electrolysis, electrode materials can dissolve and release trace quantities of metals and toxic material into the medium solution. Thus, oxidation and dissolution can also alter bulk pH. The pH value has been reported to change and shift within an entire $6.3 \times 10^5 \mu\text{m}^2$ bottom area of T-shaped microdevice chamber as quickly as 120 seconds at $0.05 \text{ V}_{\text{pp}}/\mu\text{m}$ and 5 kHz [16]. The applied frequency was higher than the theoretically predicted electrode charging frequency ($f_c = 500 \text{ Hz}$) meaning that the electric double layer was not well charged.

It should be noted that pH changes are always accompanied with an unavoidable change in the ion concentration. When ions are dissociated and/or released into the medium, tonicity deviates from the initial isotonic state needed for cells and creates spatial ion concentration gradients as a function of experiment time. Ion concentration gradient establishment gradually creates an osmotic pressure imbalance across the cell membrane. Changes in the ionic conditions has been reported to induce cell deformation at distances of 10 to 60 μm starting at time scales around 150 seconds in a T-shaped microdevice at $1.5 \text{ V}_{\text{pp}}/\mu\text{m}$ and 500 kHz [17]. Table 2-3 shows key previous work ([16] is from our group) in this context.

Table 2-3: Faradaic reaction detection in microdevices involving pH changes.

Solution	Characteristic length	f_c	Ref
0.1 mM KCl	10 μm and 20 μm	500Hz	[18]
0.1 mM KCl	80 μm	100 kHz	[19]
4.0 mM NaCl	100 μm	500Hz	[16]

Very few works have investigated the impact of Faradaic reactions in the bulk electrolyte and cellular membrane integrity [16, 17, 40, 41]. Thus, the impact of electrochemical reactions has been neglected for the vast majority of published DEP microfluidic systems resulting in unattributed biocompatibility challenges. To increase the reliability of the DEP microfluidics systems, the impact of medium solution property changes that effect ionic strength and conductivity on cell/biomolecule biocompatibility must be investigated.

In the vast majority of studies listed above, the possibility and extent of Faradaic reaction contributions were not controlled for nor discussed comprehensively. Thus, there exists a need for investigating the impact of Faradaic reactions and their byproducts within standard media solutions within electrokinetic microfluidic systems. The first objective of this dissertation systematically explores the impact of Faradaic reactions and its impact on cellular systems for analytical applications.

2.3.2 Interactions between Biological Cell and DEP Medium Additives

For most dielectrophoretic biomedical applications, experiments are performed using an aqueous medium solution. The dielectrophoretic force acting on the cells depends on the Clausius–Mossotti factor, f_{CM} , which is defined in terms of the dielectric properties of the medium relative to the cell. The dielectric properties of the medium depend on its chemical composition such as the salt [94, 95] and sugar additives [96, 97], amino acids [98], and proteins [99]. If chemical additives are not carefully selected, they can interact with the target cells in an undesired manner and change their dielectric properties.

One class of chemicals that is routinely added to medium solutions to increase reproducibility within microfluidic platforms without disrupting protein content of cell membranes is surfactants [50-53]. Surfactants, also known as surface-active agents, are chemical agents which adsorb to interfaces (or surfaces) and generally lower interfacial free energy [100], which is the minimum amount of work required to create the interface. Surfactants have an amphipathic structure, meaning they contain both hydrophobic groups (typically tails) and hydrophilic groups (typically heads). At low concentrations, surfactants dissolve into individual molecules within solution; but, above the critical micelle concentration (CMC), surfactant molecules aggregate in an ordered fashion to form micelles (Figure 2-2).

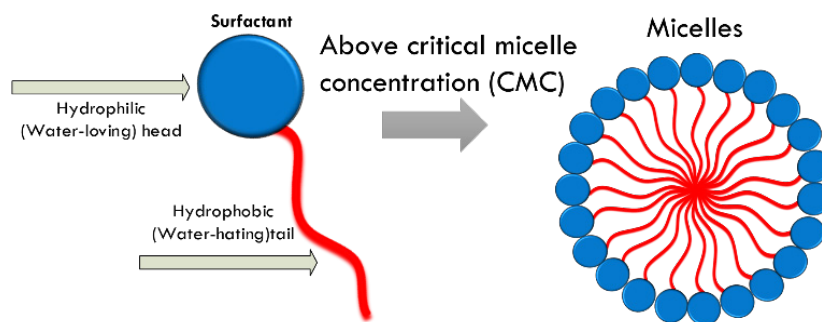


Figure 2-2: Schematic of a surfactant molecule and subsequent assembly into micelles. The blue circles represent the surfactant head (hydrophilic or water loving moieties) and the red curve represents the surfactant tail (hydrophobic or water-hating moieties). Above the critical micelle concentration (CMC), micelles readily form in an aqueous solution. In aqueous solution, surfactant molecules aggregate with their hydrophobic tails inside the micelles to avoid contact with water. In non-polar solvents, the micelle structure is reversed.

Surfactants serve different purposes in microdevices including achieving droplet generation and stabilization [101], reduce Joule heating [102], lysing cells [103], preventing biomolecule adsorption at aqueous/oil interfaces or chamber surfaces [86, 104], controlling electrolysis bubbles [39], and split conglomerated cells/particles [50, 52,

53, 86]. In non-electrokinetic systems, investigations have shown that surfactant molecules can protect red blood cells against hypo-osmotic lysis at low concentrations; however, at higher concentrations, surfactant can rupture red blood cells and release their contents into the surrounding medium. This so-called biphasic surfactant behavior has been observed for ionic and non-ionic surfactants. Microfluidic applications tend to utilize non-ionic surfactants to minimize conductivity disruptions and protein conformational changes. Non-ionic examples include poly[oxyethylene (n) nonylphenol] [105], polyoxyethylene alkyl ethers [106], octyl- β -D glucopyranoside [107], and Triton [108]. Katz et al. studied the biphasic behavior of RBCs in the presence of different Triton concentrations. He concluded that micelles formed above the CMC dissociated the red blood cell membranes [109], but RBCs were stable below the CMC.

Although surfactants are commonly added to the medium solution [50-53, 86, 100-104] in electrokinetic microdevices, their possible impact on cell dielectric properties have not been investigated. Knowledge of the degree to which surfactants could change cell dielectric properties would provide tools to accurately monitor or control the magnitude of the Clausius–Mossotti factor and resulting DEP forces. Any undefined phenomena within microscale systems should be separately studied and attributed to overall reported cellular responses in order to accurately catalog cell properties and engineer reliable microfluidic electrokinetic devices. This knowledge is needed before microfluidic point of care applications can be utilized for portable analytical and diagnostic applications.

2.4 Conclusions

DEP microfluidic systems have a broad range of applications in the biomedical sciences. This field has encompassed diverse and intensive research efforts around designs, performance, and analysis to deliver novel and cost-effective platforms. Thus, in-depth understanding of both wanted primary and unwanted secondary phenomena effecting cell behaviors has become essential and simultaneously poses substantial challenges. This dissertation outlines the unwanted secondary phenomena of cells by exploring ion reactions and ion transport impacting cell biocompatibility and viability. Prior to applying external fields within microfluidic systems, or adding chemical additives to the DEP medium solution, ion concentrations and gradients should be considered and placed in context with cell viability. In this dissertation, the assumption that aqueous media remain constant throughout electrokinetic experiments is challenged by evaluating fundamental mechanisms and possible impacts on cell-medium interactions influencing cell viability and membrane integrity. This work explores and thus provides a better understanding of these issues, which enables optimized process operating conditions and microdevice designs. Overall, this research sought to quantify and mitigate issues associated with cell viable and cell membrane integrity in electrokinetic microdevice operations. The following objectives were explored during completion of this PhD research and dissertation:

Objective 1- Exploration of the impact of Faradaic reactions on hemolysis in a microdevice with non-uniform, alternating current electric fields:

Objective 1-a: Systematical optimization of the required experimental conditions to

achieve and quantify RBC hemolysis during microdevice operation.

Objective 1-b: Isolation of the Faradaic reactions using a dielectric layer (HfO_2).

Objective 1-c: Utilization of low concentrations of Triton X-100 surfactant to characterize extent of cell protection from Faradaic reaction byproducts.

Objective 2- Investigation of the impact of low concentration surfactant on red blood cell dielectrophoretic responses:

Objective 2-a: Study of the impacts of surfactant interactions with cell membranes using dielectrophoresis over the membrane-dominated β -dispersion frequency region.

Ultimately, the reliability of a representative biomedical application was tested within a DEP platform. Here, the ability to monitor the state and progression of an infection was investigated with implications in applications ranging from detection of electrophysiological markers for disease diagnoses to possibly even screening therapeutic treatment strategies tailored to individual patients. The following objective was also explored during completion of this PhD research and dissertation:

Objective 3- Determination of the dielectric changes in membrane properties of porcine kidney cells before and after porcine parvovirus infection:

Objective 3-a: Characterization of healthy as well as porcine parvovirus infected pig kidney cells.

Objective 3-b: Determination of the membrane-related mechanisms from a previously vetted antiviral compound.

In the first two chapters, we discussed the fundamental features and potential advantages of using DEP-based microfluidic devices for biomedical assays. Our ability to manufacture microscale devices provide the opportunity in biomedical science in both research and practical tool. Shrinking the length scale creates a number of challenges by introducing unwanted secondary phenomena that can impact cell biocompatibility and viability. Microscale problems are normally approached by neglecting these secondary phenomena. These microscale problems can be modified to account for secondary phenomena that are routinely ignored at microscale systems. For those engaged in DEP biomedical applications, increasing the DEP platform accuracy is greatly desired and, in most cases, can be considered as vital. The opportunity to accurately utilize DEP forces can be worthy of investigation.

Chapter 3: Exploring the Role and Impact of Faradaic Reactions on Hemolysis in Non-Uniform AC Electric Fields

In electrokinetic microfluidic devices, metal electrodes and electrolytes can participate in undesirable surface Faradaic reactions, whose byproducts can alter solution composition and biocompatibility. This work explores the premise that these ionic byproducts are responsible for human red blood cell (RBC) lysis in non-uniform AC electric fields. Two strategies were explored to protect RBCs from surface Faradaic reaction byproducts: dielectric coating of electrodes and surfactant stabilization. A dielectric hafnium oxide (HfO_2) layer was used to prevent electron transfer between the electrodes and the electric double layer thus inhibiting surface Faradaic reactions. A low concentration of Triton X-100 surfactant was also explored as a tool to stabilize the cell membrane against ionic concentration shifts caused by Faradaic reaction products. Hemolysis extent was studied in non-uniform electric fields as a function of time, position, microdevice design (T-shaped and star-shaped), applied electric field ($0.06\text{--}0.20\text{ V}_{\text{pp}}/\mu\text{m}$), current ($30.2\text{--}47.8\text{ }\mu\text{A}$), frequency ($1\text{--}3\text{ kHz}$), with uncoated and HfO_2 coated electrodes (50 nm), and absence and presence of Triton X-100 ($70\text{ }\mu\text{M}$). Comparisons between uncoated and HfO_2 coated microdevices as well as untreated and surfactant treated RBCs were made to reveal the extent of surface Faradaic reaction byproducts.

3.1 Introduction

Lab-on-a-chip (LOC) platforms comprise multiple laboratory functions including reaction, separation, mixing, and detection in a single chip. When operational dimensions

reach the microscale, LOC advantages include high resolution, low cost, rapid analysis, and small sample consumption to perform quantitative chemical analysis, medical diagnosis, genetic abnormalities detection, and other analytical applications [2-10]. Microdevices have enabled insights into genetic sequencing, proteomic distributions, and cellular traits through the use of electrokinetic tools to manipulate and reproducibly distinguish charged cells, proteins, DNA, and other subcellular biomolecules [1].

Despite advancements in electrokinetic microdevices, portable diagnostics have not yet proven to be more reliable and dependable than lab-scale analytical tests. The ability to increase reliability is linked to fully understanding, and thus controlling, non-ideal phenomena that influence microscale electrokinetic phenomena. Since electrokinetic microdevices manipulate nanoliter sample volumes, the finiteness of ions within the system can dominate responses if sufficient buffer is not present to maintain local ion equilibrium [110]. The ability to consistently discern cellular and molecular-level differences in complex systems depends upon constant medium conditions [111, 112]. However, our work and others have shown that in electrokinetic microdevices, externally imposed electrical potentials can cause unbalanced ion migration yielding pH and other ion gradients in electrolyte solutions which impact analyte composition over time [16-19, 113-118].

Advantages attributed to utilizing alternating current (AC) electric fields within microdevices have included relatively constant medium conditions with respect to pH, ionic concentration, and ionic strength. Constant medium condition assumptions are based upon the premise that Faradaic reactions are insignificant within AC microdevices

[16-19, 113-118]. Faradaic reactions involve oxidation/reduction electrochemical reactions between the electrode and the electrolyte where ions are transferred into or out of the electric double layer (EDL). Faradaic reactions can be chemically reversible or irreversible, depending on the electrode, electrolyte, and electric field [119-121]. Depending upon the applied potential, electron transfer across the electrode/electrolyte interface may give rise to excess ions entering the electrolyte. Dissolved species resulting from Faradaic reactions at electrode/electrolyte interfaces include electrolysis byproducts [H^+] or $[OH^-]$, release of oxygen gas, and electrode oxidation [119-121]. Our group's prior research on electrode surface Faradaic reactions in non-uniform AC electric fields has revealed that ionic byproducts accumulate and transport within microdevice test chambers yielding non-constant media conditions [16, 17]. Therefore, time and spatial dependent media changes need to be explored further by quantifying the role and impact of Faradaic reactions on cellular functions to ultimately achieve reliability and reproducibility of electrokinetic microdevice applications.

Spatially non-uniform AC electric fields can yield dielectrophoretic (DEP) forces on objects. DEP is a nonlinear electrokinetic technique more commonly employed for larger bioparticle manipulation and has been extensively explored for precise cellular-level diagnostics and analysis.

Spatially non-uniform AC electric fields can yield dielectrophoretic (DEP) forces on objects. DEP is a non-linear electrokinetic technique more commonly employed for (bio)particle/cell manipulation. DEP technique has been extensively explored for precise cellular-level diagnostics and analysis over the course of a few milliseconds up to several

minutes experiment [122-127]. A spatially non-uniform AC electric field can induce a charge dipole resulting in a dielectrophoretic force (\vec{F}_{DEP}). Here, human red blood cells (RBCs) were utilized within a microfluidic platform. RBCs are biconcave disks filled with cytoplasm and can be well-described as single-shell oblate spheres [128, 129]. For a single-shell oblate spheres with radius, r , oriented parallel to the electric field [130, 131]:

$$\vec{F}_{DEP} = \frac{3}{2} V_c \epsilon_m \text{Re}[f_{CM}] \nabla \vec{E}^2_{rms} \quad (3-1)$$

where, V_c is the cell volume, ϵ_m is the medium permittivity, $\text{Re}[f_{CM}]$ is the real component of the Clausius–Mossotti factor (which is the effective polarizability of particle or cell relative to the surrounding medium) and $\nabla \vec{E}^2$ is the electric field gradient squared [130]. If the cells move in the direction of increasing electric field, this behavior is referred to as positive DEP (p-DEP). If DEP forces push the cells away from the high field regions, this is known as negative DEP (n-DEP). To induce dielectrophoretic force (\vec{F}_{DEP}), applied potential with frequency ranging from a few Hz to a few MHz over the course of a few milliseconds up to several minutes experiment. As shown in equation (3-1), the cell polarizability and resulting \vec{F}_{DEP} depend strongly upon the surrounding medium.

In microfluidic devices, an aqueous electrolyte is used commonly as a medium. The internal microfluidic channels carry net electric charge and when these surfaces are brought in contact with an electrolyte, counterions in the bulk electrolyte transport toward the oppositely charged electrodes. This gives a rise to formation of a layer called the electrical double layer (EDL). The Gouy-Chapman-Stern model (GCS) provides a

realistic description of the EDL interfacial phenomena via two layers: Stern layer and diffuse layer. The Stern layer is the region next to the surface where a layer of ions with a single layer of solvent molecules around each ion is specifically adsorbed to the surface. The Stern layer has two planes; the inner Helmholtz plane (IHP) and the outer Helmholtz plane (OHP). The IHP passes through the center of the specifically adsorbed ions while the OHP passes through the center of solvated ions at their closest distance to the surface. Finally, beyond the Stern layer the diffuse layer forms which merges into the bulk electrolyte. [132]. The presence of external potentials alter the electrical double layer into a new equilibrium. The EDL plays an important role in determining AC Faradaic reaction rates in microfluidic systems. Grahame discussed that ion reduction takes place within the EDL instead of the bulk medium. Thus, the reaction rate-related potential and concentration appear at the OHP instead of in the bulk medium [89]. The thickness of the EDL, or the Debye length λ_D , can be expressed as a function of the ionic strength, I , of the bulk electrolyte, which is a weighted sum of charges [133]:

$$\lambda_D = \sqrt{\frac{\varepsilon_0 \varepsilon_r k_b T}{2 N_A e^2 I}} \quad (3-2)$$

$$I = \frac{1}{2} \sum_{i=1}^N c_i z_i^2 \quad (3-3)$$

where ε_0 is the vacuum permittivity and equals to approximately 8.85×10^{-12} (F/m), ε_r is the relative permittivity of the medium, k_b is Boltzmann's constant, T is the absolute temperature in kelvins, N_A is the Avogadro's number, and e is the elementary charge. As shown in equation (3-3), the ionic strength, I , is a function of the concentration of all ions

in the solution where c_i is the molar concentration, and z_i is the charge number of the i^{th} ion. The EDL establishment depends on the charging frequency, f_c , as follows [49, 90]:

$$f_c = \frac{\sigma_m \lambda_D}{2\pi \epsilon_m L} \quad (3-4)$$

where σ_m is the conductivity of the medium and L is the characteristic length. Dielectrophoretic measurements utilize sub-hertz frequencies up to ~ 1 GHz to the appearance of α - (sub-Hz to kHz), β - (kHz to MHz range), and γ - (MHz to GHz range) dispersion within medium conductivity and permittivity of 0.001 to 0.250 S/m and $\sim \epsilon_0 80.00$ [66, 134, 135]. If the applied frequency, f , is lower than the charging frequency ($f/f_c \ll 1$), the counterions have sufficient time to migrate in and out of the EDL in response to each change in sign of the field direction and to form well-established EDL. On the other hand, at higher frequencies ($f/f_c \gg 1$) the polarization time is very short and not sufficient for counterions to follow the change in sign of the field direction and develop a well-established EDL [16, 91]. Previous research has focused predominantly on the impact of ions generated due to Faradaic reactions at extremes, e.g. high voltages and frequencies well below the charging frequency that yielded unique flow reversal patterns [19, 49, 136]. However, the impacts of Faradaic reactions and EDL formation dynamics are not limited to extreme conditions. Studies show that Faradaic reactions can still occur at frequencies slightly above f_c [16, 19]. In this work, phosphate buffer saline (PBS) solutions with 0.100 S/m conductivity and relative permittivity of 77.98 estimate the EDL as 1.91 nm thus yielding f_c up to 0.439 kHz and 0.862 kHz for T-shaped and star-shaped microdevices, respectively.

Faradaic reaction byproducts can travel into the medium via electromigration. To study ion concentration gradients induced by Faradaic reactions, the Nernst-Planck (NP) equation can be expressed as:

$$\text{Accumulation} = \text{Electromigration} + \text{Diffusion} + \text{Convection} + \text{Reaction} \quad (3-5-a)$$

$$\frac{\partial C_j}{\partial t} = \frac{Z_j e}{K_b T} D_j C_j \nabla^2 \Phi + D_j \nabla^2 C_j - C_j \vec{v} + R_j \quad (3-5-b)$$

where C_j is the ion concentration, D_j is diffusivity, \vec{v} is convective flux velocity, Φ is the electric potential, and R_j represents bulk liquid reactions. R_j is zero for strong electrolytes due to complete ion dissociation. At steady state, the Nernst-Planck equation simplifies to:

$$-D_j \nabla^2 C_j = \frac{Z_j e}{K_b T} D_j C_j \nabla^2 \Phi - C_j \vec{v} \quad (3-6)$$

In this equation, the electric potential (ϕ) is described by the Poisson equation: $\vec{\nabla} \cdot (\epsilon_0 \epsilon_r \vec{\nabla} \phi) = -\rho_f$ where ρ_f is the charge density and is summation of each ion charge (e_j) multiplied by the ion concentrations (C_j), $\rho_f = \sum_j e_j C_j$. The Nernst-Planck (NP) and Poisson equations are the continuum model of an electrolyte subjected to an electric field which describes ion fluxes as a result of diffusion, electromigration, and convection. Faradaic reactions can be represented as an electrode boundary condition in the Nernst-Planck equation. Electromigration, diffusion and convection are the three possible transport processes to generate ion concentration gradients in non-uniform electric fields. This work explores the impact of Faradaic reactions on ion concentration gradients, induced by an ion flux in equation (3-6), by tracking hemolysis patterns.

Cell lysis can occur via chemical, mechanical, thermal, optical, acoustical, osmotic, electrical, and electrochemical lysis. Electrical and electrochemical lysis are the most relevant to this study. Electrical lysis, a cell membrane breaching technique, relies upon ion transport and accumulation to achieve pore formation and consequently cell lysis. Electric potential and exposure time are important parameters for cell lysis. Generally, once the membrane voltage induced by an electric field exceeds a 0.2-1.0 V threshold, membrane pore formation occurs and leads to substantial rises in the cell's membrane permeability. The transition from pore formation to full cell lysis can be achieved when the cell membrane potential reaches $\sim 1.1\text{V}$, usually requiring an externally applied electric field of between ~ 0.02 to $80\text{ V}_{\text{pp}}/\mu\text{m}$ [62, 137-146]. Depending on electric field density, AC signals in the frequency range of a few kHz to a few MHz induce cell lysis within 50 ms to 20 min [62, 137-146]. The conditions explored in this work, $0.1\text{ V}_{\text{pp}}/\mu\text{m}$ at 1 kHz over 15 minutes, do overlap with the conditions favorable for electrical cell lysis.

An electrically induced cell lysis is not always a consequence of a strong electric field. When the electric current passes through the medium solution, Faradaic reactions can occur at the electrode and medium interface. In electrokinetic-based microfluidic systems, water electrolysis is often the most dominant Faradaic reaction as studied in previous works. In water electrolysis, pH changes are induced through formation of hydrogen ions $[\text{H}^+]$ at the anode and hydroxide ions $[\text{OH}^-]$ at the cathode. In addition to water electrolysis, electrode can undergo oxidation and dissolution during electrical stimulation and release trace quantities of toxic dissolved material into the medium

solution. Metal oxidation and dissolution can also create pH gradient. Bulk pH value has been reported to change and accumulate across the entire $6.3 \times 10^5 \mu\text{m}^2$ surface area of T-shaped microdevice chamber as quickly as 120 seconds at $0.05 V_{pp}/\mu\text{m}$ and 5 kHz [16]. It should be noted that the pH change is always accompanied with an unavoidable change in the ion concentration. When ions are dissociated and/or released into the medium tonicity deviates from the initial isotonic state and creates spatial ion concentration gradients as a function of experiment time. Ion concentration gradient establishment gradually create an osmotic pressure imbalance across the cell membrane. Changes in the ionic conditions has been reported to induce cell deformation at distances of 10 to 60 μm starting at time scales over 150 seconds in a T-shaped microdevice at $1.5 V_{pp}/\mu\text{m}$ and 500 kHz.

Relatively sudden or extreme changes in the pH and ionic conditions can be harnessed for a novel cell lysis technique, known as electrochemical lysis. In this technique, upon the application of electric field the produced hydroxide ions induce membrane permeabilization and cell lysis by cleaving fatty acids [78-82]. While electrode byproducts can be advantageous in some electrokinetic-based microfluidic applications, this is not uniformly desired. When the pH and/or ion concentration gradient are not taken into consideration, it is not only difficult to improve the experimental procedures, but this can also lead to misinterpretation of the results [147]. Since cells are sensitive indicators of both adverse pH and ion concentration (osmotic pressure gradient) shifts, cell lysis patterns can be used to explore the role and impact of Faradaic reactions in non-uniform AC electric fields. Thus, medium pH and ion concentration complications

from Faradaic reactions can be tracked via cell lysis patterns if proper electrical field controls are implemented. Thus, medium pH and ion concentration complications from Faradaic reactions can be tracked via cell lysis patterns if proper electrical field controls are implemented. The conditions explored in this work, $0.1 \text{ V}_{pp}/\mu\text{m}$ at 1 kHz over the course of 15 minutes overlap with the conditions favorable for cell lysis to study ion behavior.

Strategies to impede complications from ion behavior at the microscale include either preventing ion generation or protecting cells from tonicity changes. The first strategy employed herein was to physically isolate electrodes from the electrolyte to suppress Faradaic reactions and thus ionic byproducts at the electrode surface. In electrokinetic microdevices, electrode/electrolyte isolation has been achieved via contactless electrodes [148], membrane isolation [39], hydrogel layers [149], and passivation layers [46, 150]. Here, a passivation layer was utilized to create a physical barrier between electrodes and the electrolyte. Hafnium oxide (HfO_2) was selected because of its favorable thermal, chemical, mechanical stability, and optical transparency [44, 151-153]. The second strategy was to protect the cell by stabilizing the cell membrane. In non-electrokinetic and non-microdevice systems, low concentrations of non-ionic surfactant ($<1\%$) were observed to stabilize and protect cell membranes as the medium deviated from isotonic conditions [108, 154]. At low concentrations, surfactant molecules insert into the cell membrane causing cell enlargement by lowering the lateral surface tension. Surfactant molecule intercalations within the cell membranes modify internal and external ion concentrations to protect cells against environmental stressors. It

should be noted that at high concentrations above the critical micelle concentration (CMC), surfactant molecules sufficiently interfere with lipid bilayer interactions to induce cell rupture. Here, 70 μM Triton X-100, which is significantly less than the CMC of 240 μM , was employed to stabilize and protect cells from ion accumulations [108, 154].

Understanding these ionic and molecular interactions has implications in precise control of cell manipulations. This work fills a critical gap in electrokinetic microdevice knowledge by determining Faradaic reaction byproducts when (i) ion generation/transport pathways are impeded, and (ii) RBC membranes are stabilized against environmental stress. In the present work, hemolysis was studied as a function of time and position to discern and quantify strategies to impede ion generation and accumulation effects in non-uniform alternating current electric fields. Low-frequency dielectrophoretic fields near the electrode charging frequency were used to evaluate the impact of Faradaic reaction byproducts on hemolysis in uncoated and HfO_2 coated microdevices (T-shaped and star-shaped). Hemolysis in both microdevice designs were analyzed at both constant electric field and constant current conditions. Electrical signals were systematically compared and analyzed as a function of frequency (1-3 kHz) and applied electric field (0.06-0.20 $\text{V}_{\text{pp}}/\mu\text{m}$) to determine conditions for hemolysis in uncoated microdevices. To compare hemolysis between uncoated and HfO_2 coated microdevices, a constant current condition was identified via impedance spectroscopy. Lastly, a low concentration of Triton X-100 surfactant (70 μM) was explored as a cell treatment to obstruct the effect of released Faradaic reaction byproducts. In tandem, this

work provides multiple approaches to more reproducibly manipulate cells within electrokinetic microdevices.

3.2 Materials and Methods

3.2.1 Microdevice Design and Fabrication

To study Faradaic reaction effects, two different Cr/Au electrode configurations were designed, fabricated, and interfaced with a microfluidic chamber. As shown in Figure 3-1, T-shaped electrodes had one pair of 116 μm wide orthogonal electrodes spaced 100 μm apart with a thickness of 15 nm Cr/95 nm Au on $75 \times 25 \times 1 \pm 0.1$ mm glass microscope slide (AmScope.com). The star-shaped electrode design had four pairs of triangular electrodes converging symmetrically at a center point gap of 250 μm with a thickness of 10 nm Cr/ 95 nm of Au. Photolithography, sputtering, and lift-off were employed to fabricate the microelectrodes on glass microscope slides following published procedures [16, 17]. Experiments were conducted with and without a dielectric hafnium oxide (HfO_2) coating over the electrodes as a passivation layer. HfO_2 thin layer films were deposited via electrosputtering to a thickness of 50 nm [44]. Photolithography was employed to fabricate a master wafer from which Polydimethylsiloxane (PDMS) castings were obtained [16, 17]. Electrodes were overlaid by a $900 \mu\text{m} \times 800 \mu\text{m}$ and 70 μm high PDMS microfluidic chamber. Biopsy punches were utilized to create inlet and outlet ports of 3000 μm in diameters.

3.2.2 Chemicals and Preparation

Potassium phosphate monobasic (ACS, $\geq 99\%$) and potassium phosphate dibasic (ACS, $\geq 99\%$) were purchased from EMD Millipore (Billerica, MA, USA). Dextrose, (meets EP, BP, JP, USP specifications, anhydrous, $\geq 99.5\%$), and nonionic surfactant Triton X-100 (laboratory grade) were purchased from Sigma-Aldrich (St. Louis, MO, USA). Sodium chloride ($>99\%$, ACS) was purchased from Macron Chemicals (Center Valley, PA, USA).

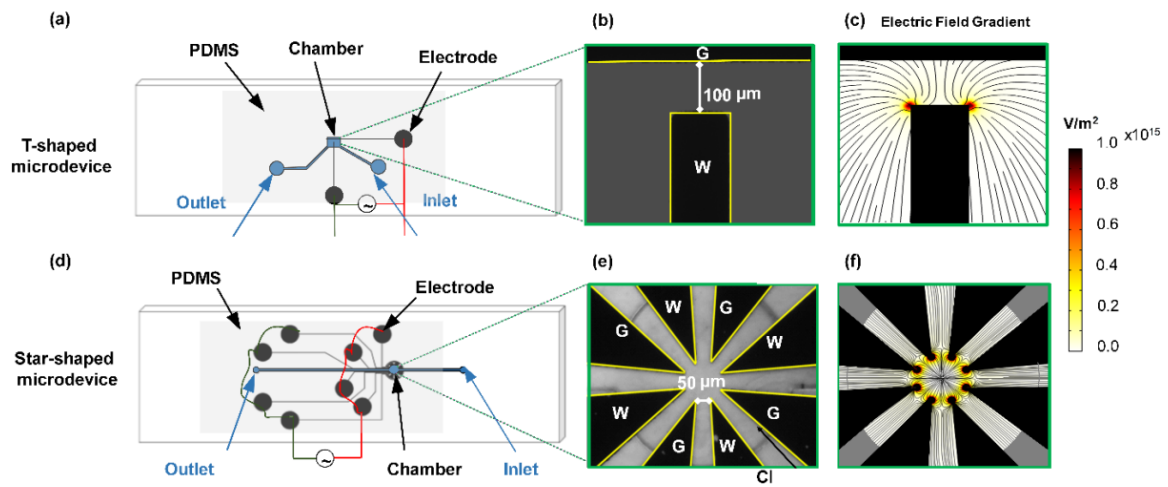


Figure 3-1: Microdevice designs. Schematics of the T-shaped (a), and star-shaped (c) microdevice designs. Electrodes microfabricated on glass slides are shown in black, fluidic channels (blue) are cast in PDMS (grey) and then plasma sealed together. Microscopy images of the working chambers are illustrated at 20 \times for the T-shaped device (b), and 10 \times the star-shaped device (d).

All RBC experiments were conducted in controlled isotonic phosphate buffer saline (PBS) solution with a conductivity of 0.1 S/m. To prepare PBS solution, 2.6 mM potassium phosphate monobasic, 2.6 mM potassium phosphate dibasic, 2.6 mM sodium chloride, and 274.3 mM dextrose were mixed in 24.9 mL E-pure water and stored at 4 °C for less than a week. For surfactant experiments, 135.9 mcg Triton X-100 was added to

the 0.1 S/m PBS to achieve 70 μ M solution without altering the conductivity. IRB-approved informed consent was obtained from donors before blood donation.

3.2.3 Sample Preparation

Human blood samples from anonymous donors were collected in Becton Dickinson lavender top EDTA vacutainers, stored at 4°C within 10 min after donation and tested on the same day of donation. IRB-approved informed consent was obtained from donors before blood donation. RBCs were centrifuged at 132 rcf for 5 min to separate RBCs from plasma. Supernatant was removed and RBCs were washed by centrifuging twice with isotonic 0.9 wt/v% NaCl solution. Packed RBCs were then mixed with 0.1 S/m phosphate-buffered to 1.0 v/v%.

3.2.4 Electrical Signal Optimization of the Uncoated Microdevice

Blood samples were introduced via ports to the relevant parallel, T-shaped, and star-shaped microdevices, which were viewed on a Zeiss Axiovert microscope (Zeiss, Oberkochen, Germany). Low frequency alternating current electric fields were applied via an Agilent 33250A Function/Arbitrary Waveform Generator (Agilent Technologies, Santa Clara, CA, US). RBC responses, before and after the potential was applied, were recorded at 20x (T-shaped, parallel) and 10x (star-shaped) magnification at 4 fpm for 15 minutes.

According to equation (3-1), DEP force is proportional to the electric field gradient intensity squared ∇E^2 . Changes in either the applied potential or the electrode configuration will alter the electric field gradient intensity and consequently cell lysis

efficiency. Thus, the applied potential was modified for each configuration. To determine optimum conditions for Faradaic reactions in uncoated T-shaped microdevices, the extent of RBC hemolysis was studied at 7 and 10 V_{pp} potential (0.07 to 0.10 $V_{pp}/\mu m$ electric field densities) and 1 to 3 kHz frequencies. For the star-shaped microdevice, conditions were 3 to 5 V_{pp} potential (0.06 to 0.20 $V_{pp}/\mu m$ electric field densities) and 1 kHz frequency. As a comparative control, hemolysis was studied in uniform electric fields generated via parallel electrodes at 0.10 $V_{pp}/\mu m$ and 1 kHz. The electric field density was calculated from the applied potential over the minimum distance for the T-shaped microdevice, and over the distance between opposing electrode tips for the star-shaped microdevice.

3.2.5 Simulations

COMSOL Multiphysics® (Burlington, MA, USA) simulation software was utilized to map the non-uniform electric field gradients of both T-shaped and star-shaped geometries. The 2D model geometries, shown in Figure 3-1-b and e, were duplicated filled with 0.1 S/m phosphate buffer saline solution (PBS). The *Electric Potential* boundaries were set to *Ground* for Au ground electrodes and 10 and 5 V_{pp} for the T-shaped and star-shaped Au working electrodes, respectively. All outer boundaries were set to *Electrical Insulation*. The electric field gradients were achieved by solving Laplace's equation using the Lagrange element method.

3.2.6 Electrical Signal Optimizations of the HfO₂ Microdevices

Experiments were conducted with 0.1 S/m PBS under both constant electric field and constant current for comparisons. To examine the contributions of the HfO₂ dielectric layer in each device, electrical impedance of both uncoated and HfO₂ coated electrodes were measured for both T-shaped and star-shaped microdevices. Figure 3-2-a and b illustrate the electrical/material configuration in the uncoated and HfO₂ coated microdevice cases. Figure 3-2-c shows the equivalent electric circuit model for an electrode/medium interface whereby the medium solution resistance is represented by R_s , the double-layer capacitance by C_{EDL} and the charge transfer resistance by R_{CT} . Electrodes uniformly coated with a defect-free dielectric layer will act as sheer capacitors [155]. However, most coating layers have permeability defects such as pinholes, that change the behavior to a parallel combination of a dielectric capacitor, C_{Coat} , and a defect resistor, R_{Defect} , as illustrated in Figure 3-2-d [155]. R_{Defect} and C_{Coat} increase electrical impedance and result in significant voltage loss at the electrode/medium interface. Electrical impedance was measured with a HP 4284A Precision Inductance Capacitance Resistance (LCR) meter ($N=3$). Both electrode geometries were tested over a 0.9 to 10 kHz frequency range. The T-shaped microdevice was operated at 0.10 V_{pp}/μm and 0.13 V_{pp}/μm while the star-shaped microdevice was operated 0.10 V_{pp}/μm and 0.16 V_{pp}/μm to explore constant electric field and constant current conditions.

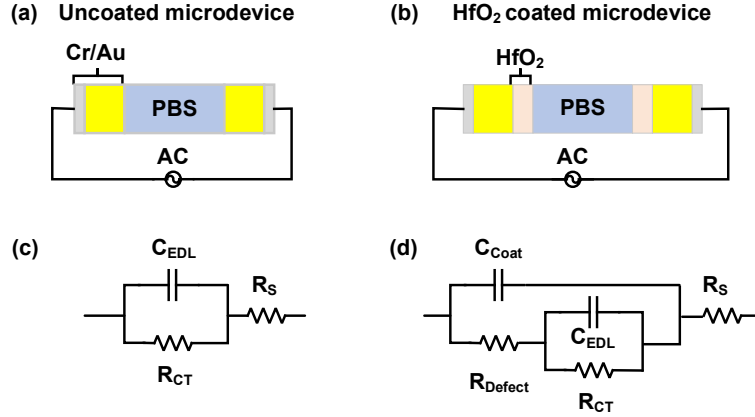


Figure 3-2: Electrical/material configuration in (a) uncoated microdevice and (b) HfO₂ coated microdevice. Equivalent electric circuit diagram for (c) uncoated device, and (d) HfO₂ coated microdevice with both permeable and impermeable defects [155].

3.2.7 Data Analysis

Hemolysis was observed in real time using video microscopy; when the membrane become compromised, the intracellular contents were released into the surrounding medium. The release changed the RBC's optical contrast such that image intensity analysis correlated with the transition from healthy to lysed cells. Video frames were analyzed with ImageJ® software to measure a cell-based intensity of each frame indicative of hemolysis. Intensities for each frame, I_i , were divided by initial ($i=0$) non-potential RBC intensities, I_o , to plot the normalized intensity \bar{I}_i versus time. Hemolysis percentage, H_i , was calculated using the normalized intensity \bar{I}_i .

$$\bar{I}_i = I_i / I_o \quad (3-7-a)$$

$$H_i = (1 - \bar{I}_i) \times 100 \quad (3-7-b)$$

H_i and \bar{I}_i have inverse trends, but the change from time zero can be used to track hemolysis. Final hemolysis percentage ($i = f$), H_f , was calculated using the final frame normalized intensity \bar{I}_f . MATLAB[®] was employed to plot contour maps of the positional hemolysis propagation over time for at least five repeats for both the T-shaped and star-shaped designs. Videos were analyzed frame by frame to track individual RBC location and hemolysis time. Locational dependencies were examined to ascertain proximity of Faradaic byproducts from the electrode. Due to symmetry, the T-shaped microdevice was analyzed over half of the chamber while the star-shaped device was analyzed over the entire chamber.

3.3 Results and Discussion

Optimal RBC hemolysis was obtained for uncoated T-shaped and star-shaped devices. The electrical signal optimizations for potential and frequency were compared and systematically analyzed in both constant current and constant voltage modes in both geometries. The HfO₂ layer on the Cr/Au electrodes was characterized by Faradaic impedance spectroscopy to determine an equivalent constant current experimental condition. Hemolysis was then studied in non-uniform electric fields as a function of time, position, device geometry (T-shaped and star-shaped), frequency (1-3 kHz), applied electric field (0.06-0.20 V_{pp}/μm), current (30.2-47.8 μA), with uncoated and HfO₂ coated electrodes (50 nm), as well as in the absence and presence of 70 μM Triton X-100 surfactant.

3.3.1 Electrical Signal Optimization of the Uncoated Microdevices

It was observed that RBC hemolysis can be maximized by fine-tuning the operating voltage and frequency. Hemolysis was tracked as a function of time for five or more repeats in non-uniform AC electric fields for two microdevice geometries: uncoated T-shaped and star-shaped microdevices. Applied potential and frequency optimizations were completed on the T-shaped device employing electric fields between 0.07 to 0.10 $V_{pp}/\mu m$ and frequencies between 1 to 3 kHz. The T-shaped microdevice had a minimum gap of 100 μm such that the electrode charging frequency was 0.439 kHz (equation 3-4). Frequencies were tested from 1 to 3 kHz because these were above the charging frequency where the EDL layer is not fully charged but retains EDL ion distribution and capacitance.

Figure 3-3-a shows hemolysis captured by the normalized intensity (\bar{I}_i) via equation (3-7-a) as a function of time between 0.07 to 0.10 $V_{pp}/\mu m$ at 1 kHz. RBCs remained intact and experienced weak n-DEP at 0.07 $V_{pp}/\mu m$. Above 0.08 $V_{pp}/\mu m$, n-DEP was still observed, but hemolysis became discernible as demonstrated by a smooth and gradual decrease of \bar{I}_i in -a (i.e. from 0 to 900 sec). The greatest change in intensity and thus hemolysis was observed at 0.10 $V_{pp}/\mu m$ for a fixed frequency of 1 kHz. A gradual decrease was observed up to 475 sec, followed by a more rapid decrease from 475 to 915 sec indicative of a hemolysis cascade. This transition at 475 sec was termed the threshold time. Figure 3-3-b illustrates the final extent of hemolysis, H_f , calculated from equation (3-7-b). As the frequency increased, the extent of hemolysis decreased significantly.

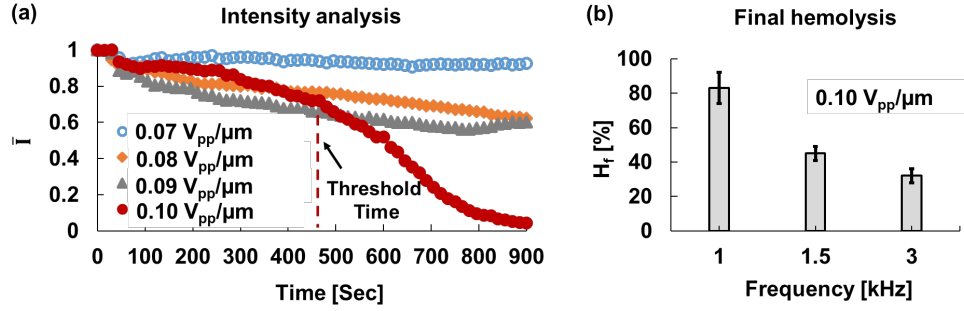


Figure 3-3: Intensity analysis of video microscopy images from the T-shaped microdevice to obtain a normalized intensity (\bar{I}_t) and subsequent final hemolysis, H_t , for RBCs diluted to 1.0 v/v %. (a) Intensity versus time dependence on potential for 0.07 to 0.10 $V_{pp}/\mu m$ field conditions. (b) Final hemolysis percentage versus frequency at 0.10 $V_{pp}/\mu m$. Optimal hemolysis conditions for the T-shaped microdevice were 0.10 $V_{pp}/\mu m$ and 1 kHz. Error bars represent standard deviation for $n \geq 5$ repeats.

For the star-shaped microdevice, the applied potential explored was from 0.06 to 0.20 $V_{pp}/\mu m$ due to differing electric field density patterns. Further, hemolysis experiments were conducted at a fixed frequency of 1 kHz since hemolysis decreased significantly above this frequency similar to the T-shaped microdevice. The star-shaped microdevice had a minimum gap of 50 μm such that the electrode charging frequency was 0.862 kHz. Insignificant hemolysis was observed at 0.08 $V_{pp}/\mu m$; at and above 0.20 $V_{pp}/\mu m$ electrolysis prevailed causing permanent instant damage to the electrodes. Thus, operational conditions were selected to avoid these more extreme, rigorous Faradaic reactions. Optimum hemolysis conditions for the star-shaped microdevice were also determined to be 0.10 $V_{pp}/\mu m$ and 1 kHz.

3.3.2 Electrical Signal Optimization of the HfO₂ Coated Microdevices

Incorporation of a thin HfO₂ layer between the electrode and electrolyte interface reduces Faradaic reactions [44, 151-153]. However, the HfO₂ layer over the electrodes also reduces the effective electric field and thus the current within the solution. The

electrical potential modulates the current; therefore, the electrical potential must be optimized to achieve a favorable balance between the HfO_2 barrier and current modulation. The electrical impedance, Z , and current, I , were measured to refine the electrical potential prediction necessary to obtain equivalent current between HfO_2 and uncoated devices. In Figure 3-4, impedance and current were plotted versus frequencies from 0.9 to 10 kHz for (i) uncoated T-shaped electrodes at $0.10 \text{ V}_{\text{pp}}/\mu\text{m}$, (ii) HfO_2 coated T-shaped electrodes at $0.10 \text{ V}_{\text{pp}}/\mu\text{m}$, and (iii) HfO_2 coated T-shaped electrodes at $0.13 \text{ V}_{\text{pp}}/\mu\text{m}$. The results showed that, in all three cases, as the frequency increased, the HfO_2 passed more current into the solution as evidenced by impedance decreases.

Optimum electrical signal conditions for hemolysis occurred at $0.10 \text{ V}_{\text{pp}}/\mu\text{m}$ and 1 kHz, resulting in currents of $47.4 \mu\text{A}$ and $47.8 \mu\text{A}$ for uncoated T-shaped and star-shaped microdevices, respectively. In the presence of HfO_2 , impedance increased from $73.6 \text{ k}\Omega$ to $112 \text{ k}\Omega$ for the T-shape microdevice. This corresponds to a current reduction from $47.4 \mu\text{A}$ to $31.4 \mu\text{A}$ (-34%). To compensate for the current loss, it was calculated that if the electric field density increased to $0.13 \text{ V}_{\text{pp}}/\mu\text{m}$, a current of $46.4 \mu\text{A}$ was measured within the HfO_2 coated T-shape microdevice. This was considered sufficiently close to the $47.4 \mu\text{A}$ measured from the uncoated microdevice. Therefore, for the HfO_2 coated T-shaped microdevice, hemolysis experiments were conducted at both $0.10 \text{ V}_{\text{pp}}/\mu\text{m}$ and $0.13 \text{ V}_{\text{pp}}/\mu\text{m}$ to compare both constant electric field density and constant current conditions, respectively.

In the star-shaped microdevices, currents measured at $0.10 \text{ V}_{\text{pp}}/\mu\text{m}$ and 1 kHz were reduced from $47.8 \mu\text{A}$ for uncoated to $30.2 \mu\text{A}$ for HfO_2 coated microdevices; this was a

current reduction of 78%. In the HfO₂ coated star-shaped microdevice, increasing the electrical field density from 0.10 V_{pp}/μm to 0.16 V_{pp}/μm increased the current from 30.2 μA to 45.6 μA, which was considered sufficiently close to 47.8 μA. Thus, for the HfO₂ coated star-shaped microdevice, hemolysis experiments were conducted at both 0.10 V_{pp}/μm and 0.16 V_{pp}/μm to achieve constant applied electric field density and constant current conditions, respectively.

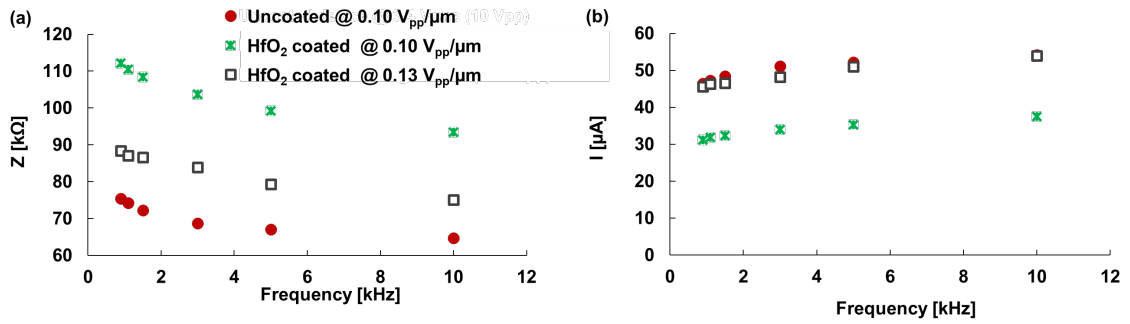


Figure 3-4: For T-shaped microdevices, (a) impedance, Z[kΩ], and (b) current, I[μA], plotted as a function of frequency. Data show an uncoated microdevice at 0.10 V_{pp}/μm compared to HfO₂ coated microdevices at 0.10 V_{pp}/μm and 0.13 V_{pp}/μm. As the frequency increased from 0.9 to 10 kHz, impedance reduced for all microdevice conditions. Consequently, current increased versus frequency. Subsequent hemolysis experiments were conducted at both 0.10 V_{pp}/μm and 0.13 V_{pp}/μm to compare constant voltage and constant current.

3.3.3 Time and Spatial Dependence of Hemolysis in Non-Uniform AC Fields

To investigate the impact of electrical cell lysis on RBC hemolysis, as a comparative control, hemolysis was studied in uniform electric fields generated via parallel electrode pairs at 0.10 V_{pp}/μm and 1 kHz. Figure 3-5-a, b, c and d (first row) show the still images before and while the potential is applied at 200, 550, and 915 sec. Prior to applying the potential, RBCs were uniformly distributed (Figure 3-5-a). After applying the potential, RBCs were pushed between the parallel electrodes towards the chamber center with low

electric field density, indicative of n-DEP (Figure 3-5-b, c, and d). The potential inducing cell lysis depends on the electric field strength, but not the gradients. Comparison of images at 915 seconds in Figure 3-1-d, Figure 3-1-g, and Figure 3-1-k illustrated no substantial hemolysis during the 915-sec uniform field experiment in the parallel electrode configuration at the same electric field and medium conditions as in the non-uniform case.

To investigate the impact of Faradaic reaction on RBC hemolysis, hemolysis was studied in non-uniform electric fields generated T-shaped and star-shape electrode configurations at $0.10 \text{ V}_{pp}/\mu\text{m}$ and 1 kHz. As shown in Figure 3-1-c and f, the both T-shaped and star-shape microdevice was designed to yield symmetric electric field non-uniformities to induces DEP motion in polarizable cells. Figure 3-5-e, f, g (row 2) and 5-i, j, k (row 3) show still images before and during applying the potential for the T-shaped and star-shaped geometries, respectively. Prior to applying the potential, RBCs were uniformly distributed in both microdevice chambers (Figure 3-5-e and i). After applying the optimal potential, RBCs were pushed toward regions with low electric field density, indicative of n-DEP. For the T-shaped electrode microdevice, cells moved towards the chamber sides, as illustrated in Figure 3-5-f, whereas cells were pushed between the electrodes and towards the chamber center in the star-shaped microdevice (Figure 3-5-j). Hemolysis was first observed in higher electric field density regions and spread to lower density regions. Figure 3-5-g and k illustrate that after 915 sec in the T-shaped microdevice, more than 95% of the RBCs were lysed. Figure 3-5-h and l show contour maps of the hemolysis propagation for five or more repeats for each geometry. Within

high field density regions, cells lysed in approximately 400 sec (blue in Figure 3-5-h and l); with increasing proximity from the electrode, the time to hemolysis increased such that the lowest electric field density regions required 915 sec (yellow Figure 3-5-h and l) to achieve lysis. Thus, hemolysis propagation was not only time dependent but also spatially dependent.

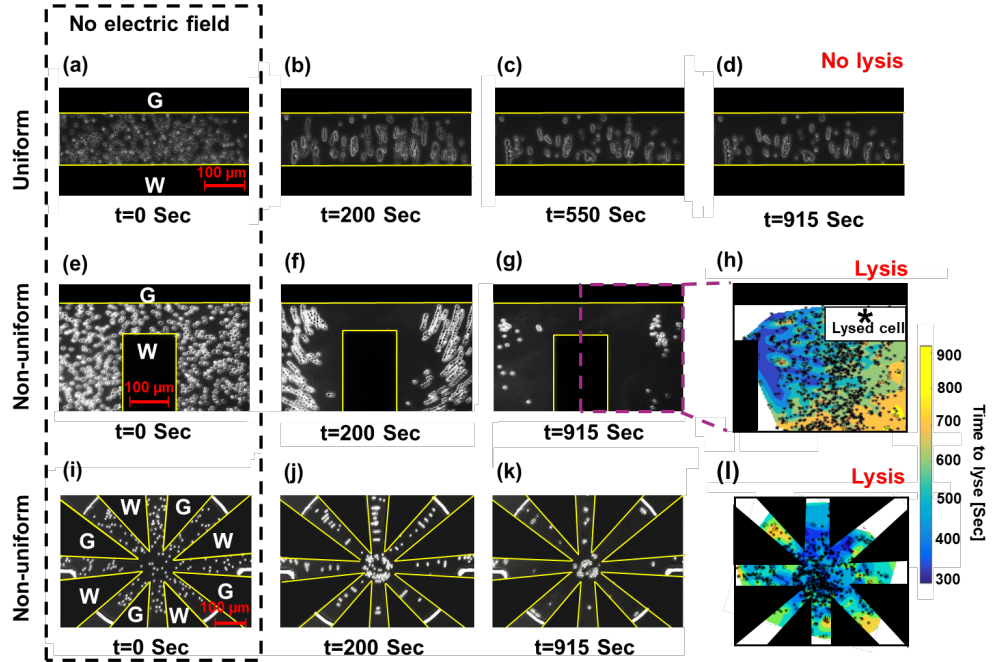


Figure 3-5: Time sequence of 1.0 v/v% red blood cells in 0.1 S/m isotonic PBS at 0.10 $V_{pp}/\mu m$ and 1 kHz applied potential for parallel (uniform), T-shaped (non-uniform), and star-shaped (non-uniform) electrode configurations. Images are shown at 0 sec (a, e, and i), 200 sec (b, f, and j), 550 sec (c), and 915 sec (d, g, and k). Cells disappear from the image upon hemolysis. Hemolysis propagation contour map of the T-shaped (h) and the star-shaped microdevices (l) illustrate cells rupture first in high electric field density regions and later in lower electric field density regions ($n \geq 5$). Scale bars are all 100 μm .

At frequencies above f_c , Faradaic reactions influence the local ion and pH (formation of $[OH^-]$ and $[H^+]$ ions) [16, 17]. These ion and pH changes have been shown to vary with time and position in the T-shaped microdevice (identical to the T-shape

microdevices in this study) [16, 17]. The Nernst-Planck equation (3-6) describes ion transport and concentration gradients in non-uniform electric fields [16, 17] whereby high electric field density regions have greater ion concentrations while lower electric field regions have bulk or reduced ion concentrations. The hemolysis cascade was discernable from the increased hemolysis rate after the noted threshold time (vertical line in Figure 3-3-a). Figure 3-5-h and l reinforce spatial dependent behavior of the ion concentration gradient since hemolysis began at regions closest to the electrodes (e.g. greater ion concentrations), and then expanded toward regions of lower electric field density (e.g. lower ion concentrations). DEP translation and alignment of RBCs were first observed followed by membrane rupture, which was attributed to unsustainable membrane polarizations. As cells ruptured, they released more conductive, ion-rich intracellular material into the solution, which likely contributed to the observed hemolysis cascade previously noted in Figure 3-3-a as the threshold time and beyond. Thus, the hemolysis observed can be attributed to both membrane polarization-induced hemolysis as well as to gradual increases in local ion concentrations that originate in and migrate from the electrode double layer then propagate out from these high electric field density regions to lower electric field density regions (N-P transport). The mechanisms contributing to hemolysis are then (i) excess ions polarizing the RBCs membrane, and (ii) destabilization of the membrane's lipid bilayer by those ions (e.g. tonicity changes). The following experiments were designed to prevent $[H^+]$, $[OH^-]$, $[Na^+]$, and $[Au^+]$ ion generation by halting Faradaic reactions on electrode surfaces.

3.3.4 Isolating Faradaic Reaction Contributions to Ion Concentration Changes

To test the hypothesis that ion generation from electrode surfaces via Faradaic reactions contributed to ion accumulations that destabilize RBCs, a dielectric HfO_2 layer was deposited over the electrodes and glass microdevice slide to prevent direct contact between the metallic electrode surface and the electrolyte solution. This dielectric layer shielded against electron transfer and thus prevented Faradaic reactions, but still enabled adequate potential to tunnel through the HfO_2 and into the solution.

Constant current and constant potential experiments were conducted to track and compare hemolysis between the HfO_2 coated T-shaped and star-shaped microdevices. Figure 3-6 shows intensity \bar{I}_t results (inversely proportional to hemolysis) with respect to time. Error bars indicate the standard deviation from at least five independent experimental repeats. Comparisons between uncoated and HfO_2 coated T-shaped microdevices illustrated that overall hemolysis was notably higher for uncoated microdevices at both constant current and constant potential conditions. At constant current ($I=46.4 \mu\text{A}$), the threshold time for the HfO_2 coated T-shaped microdevice occurred later ($t=600 \text{ sec}$) compared to the uncoated device ($t=475 \text{ sec}$) as shown in Figure 6-a. Similar trends occurred for constant potential ($0.10 \text{ V}_{pp}/\mu\text{m}$) where the threshold time occurred after 700 sec for HfO_2 coated compared to 475 sec for the uncoated microdevices. At the same current, final hemolysis H_f decreased by 30% when the microdevice was coated. Similarly, at constant potential, H_f decreased by 53% in the HfO_2 coated microdevice as shown in Figure 3-6-a and e.

As shown in Figure 3-6-b, the threshold time for the HfO_2 coated star-shaped microdevice happened later ($t=550 \text{ sec}$) compared to the uncoated microdevice ($t=300$

sec) at constant current ($I=45.6 \mu\text{A}$). At constant electric field ($0.10 \text{ V}_{\text{pp}}/\mu\text{m}$), the threshold time was 700 sec. At the same current, final hemolysis H_f decreased by 33% when the star-shaped microdevice was coated with a HfO_2 layer while at constant potential, H_f decreased by 41% in the HfO_2 coated microdevice as shown in Figure 3-6-b and f.

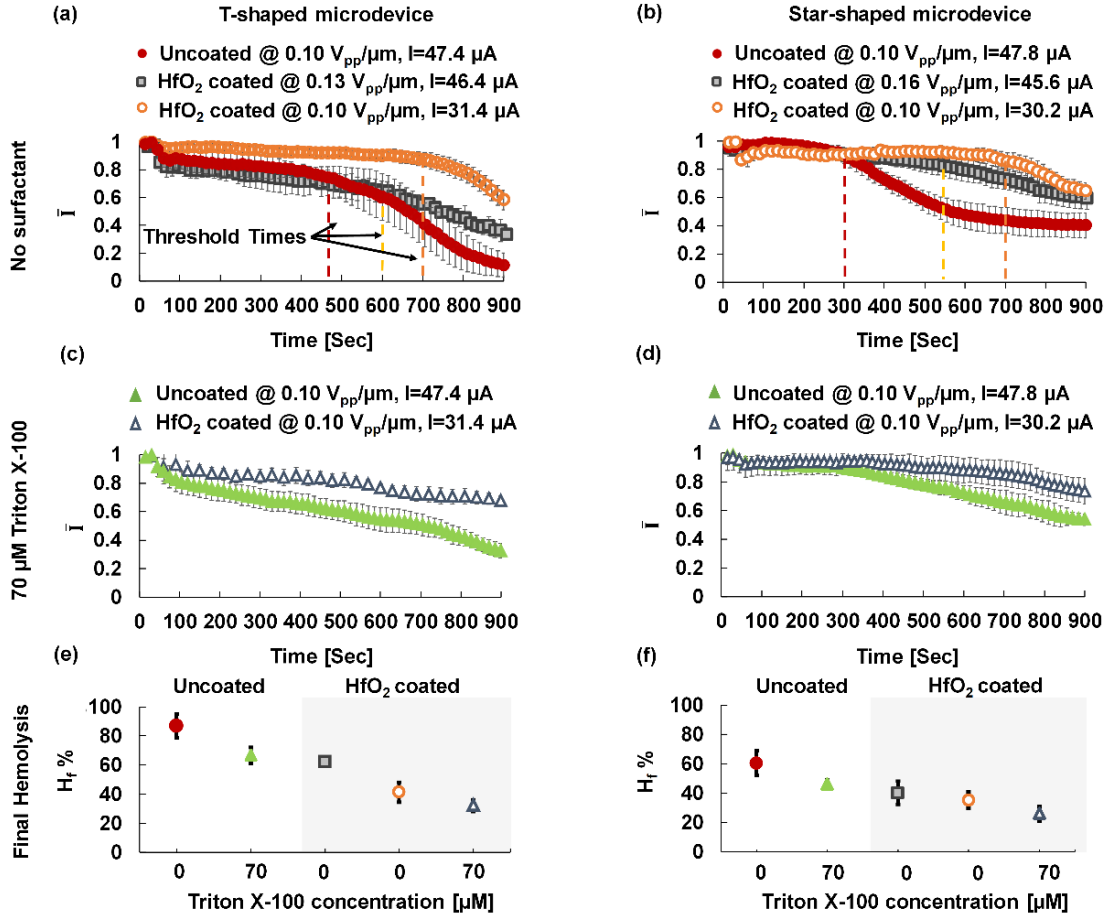


Figure 3-6: Comparisons between normalized intensity (I_t) with respect to time for T-shaped (left column) and star-shaped (right column) microdevices at 1kHz. Uncoated and HfO_2 coated microdevices are compared without 70 μM Triton X-100 (first row, a and b) and with Triton X-100 (second row c and d). Figures (e) and (f) summarize final hemolysis percentages for experiments with uncoated/coated electrodes, and absence/presence of Triton X-100 using the same symbols as (a), (b), (c), and (d). Hemolysis was greater in uncoated T-shaped and star-shaped microdevices. The presence of 70 μM Triton X-100 reduced hemolysis. Error bars depict

standard deviations from 5 independent experimental repeats. All experiments were conducted with AB- blood type.

When electrode surfaces were coated with HfO_2 (Figure 3-6-a, b, e and f), direct charge transfer between the electrode and the adjacent medium solution was shielded. For the HfO_2 coated microdevices at constant current, the cascade of cell rupture was observed later suggesting ion gradient formation was delayed or prevented within the chamber. Lower hemolysis at constant potential was attributed to both reductions in effective electric field strength as well as Faradaic reaction shielding effects with the HfO_2 film. Because HfO_2 coated microdevices displayed lower hemolysis for both constant current and constant potential conditions, these results support the hypothesis that the Faradaic reaction byproducts impact hemolysis behaviors.

At frequencies slightly above the charging frequency, applied potentials have sufficient time to allow ions to assemble more completely into electrical double layers (EDL) at the electrode surfaces. Within an established electrical double layer, ions have sufficient time to interact with the metal electrodes exchanging electrons via the Faradaic reaction pathways [16]. The resulting ionic byproducts are either transported into the bulk solution or recaptured into a transient EDL in the next half cycle of the reduction/oxidation sequence. In the conditions explored (0.10 to $0.16 \text{ V}_{pp}/\mu\text{m}$ and $30.2 \mu\text{A}$ to $47.8 \mu\text{A}$) which are centered around each microdevice's charging frequencies, Faradaic reactions at the electrode surfaces in non-uniform AC fields have been shown to change local ion concentration [16]; this work has extended this and shown the Faradaic reaction byproducts correlate with hemolysis trends.

3.3.5 Membrane Stabilization against Ion Fluctuations

To further explore membrane dynamics leading to hemolysis, the inclusion of surfactant molecules in the medium was also explored. Structurally, amphiphilic Triton X-100 was studied at low concentrations (70 μM) because this surfactant previously demonstrated lower hemolysis – without an electric field - compared to surfactant free controls [108]. All surfactant-comparison experiments were conducted at 0.10 $\text{V}_{\text{pp}}/\mu\text{m}$, 47.4-47.8 μA and 1kHz. As shown in Figure 3-6-e and f, the final hemolysis percentage was reduced by 23% with surfactant in both uncoated T-shaped and star-shaped microdevices. With surfactant and within HfO_2 coated microdevices, hemolysis observed was 50% and 27% in T-shaped and star-shaped uncoated microdevices, respectively. Combining the effects of both HfO_2 coated microdevices and Triton X-100, hemolysis was reduced by 62% for T-shaped and 57% for star-shaped microdevices. Prior research in non-electric field environments postulated that low concentration surfactants mimic the lipid environment of a cell membrane [154]; monomers incorporate into the lipid bilayer stabilizing the membrane against disruption from other forces [109]. Extending this mechanism into RBC solutions subjected to electric fields, results support attributing decreases in overall hemolysis to Triton X-100 protecting RBC membranes against ion accumulations and membrane destabilization. In uncoated devices without surfactant, threshold times were observed followed by a hemolysis cascade; this behavior differed when Triton X-100 was present as shown in Figure 3-6-c and d. \bar{I}_1 in Figure 3-6-c and d illustrates a gradual decrease without a threshold time for both T-shaped and star-shaped devices, which suggests that while Triton X-100 provides some protection, ion

accumulations gradually overpower the stabilized membrane causing RBC osmotic pressure rupture. Additional study is necessary to fully explore the molecular mechanisms of the surfactant's membrane stabilization and thus anti-hemolytic effect.

Membrane charge expression and thus polarization can also be influenced by surface markers including ABO and Rhesus (Rh) antigens [156]. ABO antigens are polysaccharide sugars, while Rh antigens are transmembrane proteins. Triton X-100 surfactant interactions with ABO and Rh blood cell antigens have not been previously explored. Since each ABO polysaccharide has a slightly different molecular structure [157], the interactions of the surfactant with the lipid bilayer membrane could be impacted and were thus explored. Four blood types (AB-, B+, A+, and O+) were tested with the absence/presence of 70 μM Triton X-100 in the T-shaped microdevice to examine surfactant interactions with ABO and Rh antigens. This enabled exploration of antigen/surfactant/ion interactions as well as antigen/surfactant interactions under the previous optimal rupturing conditions of 0.10 $\text{V}_{\text{pp}}/\mu\text{m}$ (constant potential) and 1 kHz.

Blood types B+, A+, and O+ displayed \bar{I}_1 rupture profiles similar to the AB- profiles shown in Figure 3-6, so only final hemolysis percentages, H_f , were compiled. Figure 3-7 illustrates box-and-whisker plots for samples with and without Triton X-100 in uncoated T-shaped microdevices. For all blood types, hemolysis was reduced in the presence of Triton X-100 suggesting that the surfactant's membrane stabilization properties persisted regardless of ABO-Rh expression. Although the presence of Triton X-100 lowered hemolysis for all blood types, the hemolysis reduction was more significant for blood types B+ and O+ (55% and 47%, respectively) than for A+ and AB- (19% and 23%).

Overall, blood type dependency results suggest additional complex membrane stabilization mechanisms between the membrane lipids and ABO-Rh antigens.

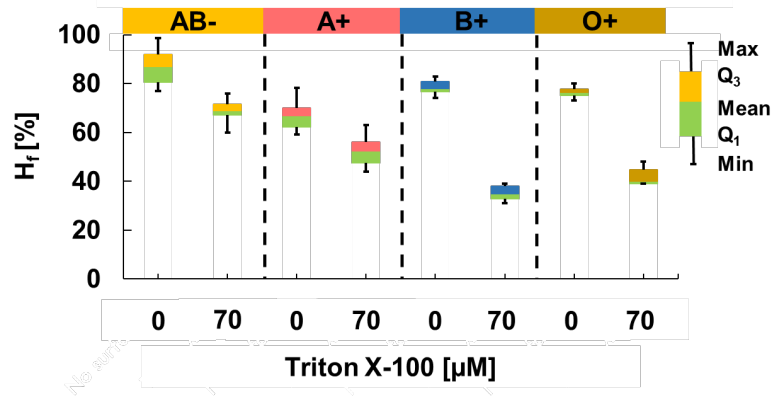


Figure 3-7: Hemolysis experiments were conducted at $0.10 \text{ V}_{pp}/\mu\text{m}$ and 1kHz ($n \geq 5$). Final hemolysis percentages are shown for AB-, A+, B+, and O+ for uncoated microdevices in the absence and presence of $70\mu\text{M}$ Triton X-100. Box-and-whisker representations allow 100% of the population to be represented. Hemolysis varied between different blood types and the surfactant Triton X-100 reduced hemolysis for all blood types.

3.3.6 Faradaic Reaction Effects at Electrode Surfaces

Additional side effects were observed from conditions where Faradaic reactions occurred. Figure 3-8-a, b, d, and e show the optical images of the uncoated and HfO_2 coated T-shaped electrodes before and after ~ 15 experiments at $0.10 \text{ V}_{pp}/\mu\text{m}$ and 1 kHz . Figure 3-8-c and f illustrate electrode height (z-dimension) with a profilometer at the red and green cross sections noted in Figure 3-8-a, b, d, and e. Comparisons of the uncoated point electrode in Figure 3-8-a and b illustrate that the Cr/Au electrode tip was corroded over time thus increasing the electrode gap to $120 \mu\text{m}$. The profilometer plot in Figure 3-8-c illustrates $\sim 25 \mu\text{m}$ Au layer degradation at the electrode edges with significant metal surface roughening in the middle.

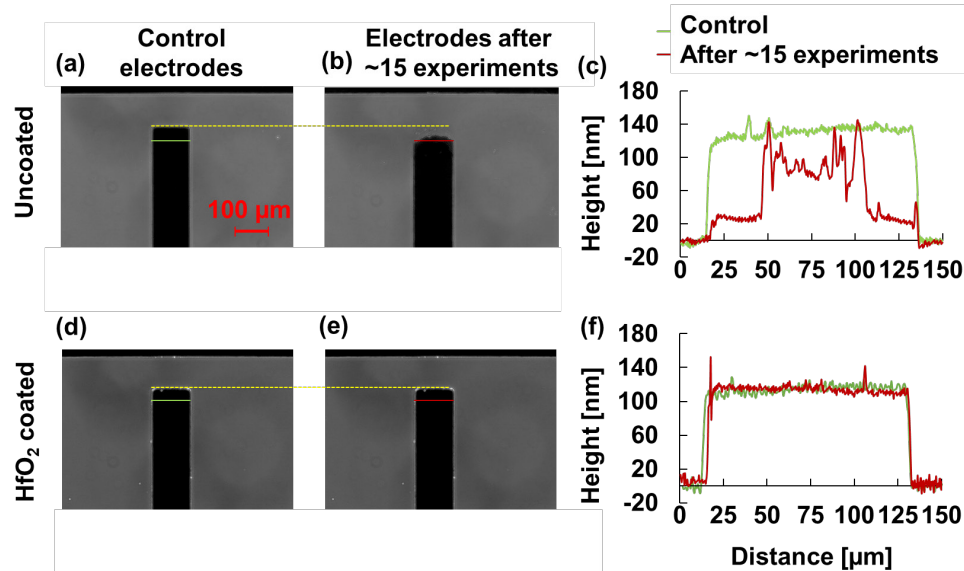


Figure 3-8: Optical images of T-shaped electrodes for both uncoated (a and b), and HfO₂ coated (d and e) electrodes before and after ~15 experiments at 0.10 V_{pp}/μm and 1 kHz. Profilometer was used to measure surface profiles for uncoated and HfO₂ coated T-shaped electrodes at the green and red cross-sections noted in the optical images. Uncoated T-shaped electrodes lost 25 μm of Au around the electrode edges, while the HfO₂ coated electrodes showed smooth cross-sections after ~15 experiments.

Representative HfO₂ coated electrodes show smooth profilometry cross-sections of the electrode tip in Figure 3-8-f. The 50 nm of hafnium oxide deposited over the Cr/Au electrodes prevented significant edge degradation and prevented electrode surface roughening. In the absence of HfO₂, applied potentials above 0.10 V_{pp}/μm at 1 kHz (just above the charging frequency) were observed to transfer electrons so energetically that metal dissolution visibly caused irreversible damage to the thin metal electrodes. Such microelectrode degradation is attributed to irreversible Faradaic reaction effects on the electrode metal [158, 159]. In summary, comparisons of experiments with and without Faradaic reaction pathways support our postulated mechanism that excess ions from Faradaic reactions contribute to ion concentration gradients which destabilize the RBC membrane to cause hemolysis. This result in context with hemolysis data in Figure 3-6

support the conclusion that Faradaic reactions occur between the medium and the energized electrodes releasing reaction byproducts into the medium.

3.4 Conclusions

This work explored the role and impact of Faradaic reactions on red blood cells in AC electrokinetic microdevices. Two different electrode arrays were utilized to create spatially non-uniform electric fields: traditional T-shaped and novel star-shaped microdevice designs. Temporal and spatial behaviors of RBC hemolysis were studied as an indicator of Faradaic reaction impacts on solutions and cellular function. Two strategies were employed to protect cells from electrode surface Faradaic reaction byproducts: dielectric coating of electrodes and surfactant stabilization of the cell membranes. Experiments were conducted with and without a dielectric coating of hafnium oxide (HfO_2) on the electrodes as well as with and without low concentration (70 μM) Triton X-100 surfactant. Conditions for hemolysis were systematically compared and analyzed both in constant potential and constant current modes. Under constant electric fields, optimum hemolysis conditions for both uncoated microdevices (T-shaped and star-shaped) were determined to be 0.10 $V_{pp}/\mu\text{m}$ and 1 kHz. Under constant current, the T-shaped microdevice was operated at 0.34 $V_{pp}/\mu\text{m}$ and 1 kHz while the star-shaped microdevice was operated at 0.16 $V_{pp}/\mu\text{m}$ and 1 kHz.

Physical mechanisms for hemolysis were systematically examined by comparing uniform and non-uniform electric field behaviors. Electrical cell lysis is potential dependent [137-139, 160-163]. However, insignificant hemolysis was observed in uniform fields, so this mechanism was not responsible for the observed hemolysis.

Comparisons between the T-shaped and star-shaped dielectrophoretic microdevices revealed spatial and temporal trends in cell hemolysis over a narrow range of frequencies around the electrode charging frequency. Hemolysis was spatially dependent with rupture propagating from the highest field density regions toward the lower field density regions. Temporal changes in hemolysis were also quantified including identification of a threshold time upon which cell rupture cascaded. Systematic comparisons between HfO₂ coated and uncoated microdevices revealed that the threshold and rupturing cascade occurred at a considerably later time in coated microdevices. Cells remained intact 125 sec longer for coated versus uncoated T-shaped microdevices and 250 sec longer for coated versus uncoated star-shaped microdevices. Overall hemolysis percentage was ~30% lower for both the T-shaped and star-shaped devices when the HfO₂ layer prevented direct electron transfer between the electrode and medium. Within a 0.1 S/m solution, the estimated electric double layer (EDL) was 1.91 nm, yielding an electrode charging frequency of 0.439 kHz and 0.862 kHz for T-shaped and star-shaped microdevices, respectively. We attributed the delayed threshold and reduced hemolysis in the HfO₂ coated devices to reduced Faradaic reaction byproducts. This rests upon the premise that the ionic byproducts from Faradaic reactions alter local ion concentrations adjacent to the electrodes. The ions migrate to form the previously experimentally quantified ion gradients [16, 17]. Such ion concentrations manifest as osmotic pressure differences across the cell membrane to induce rupture.

Comparative experiments were also conducted with and without the phospholipid mimicking surfactant Triton X-100 and revealed membrane protective abilities. At low

concentrations of 70 μM , Triton X-100 protected erythrocytes against hemolysis by 23% for T-shaped and star-shaped microdevices. Both reduced and normal Faradaic reaction rates as well as absence/presence of surfactant were tested with four different ABO-Rh blood types and revealed that surfactant protection trends were consistent across antigen expressions tested, but the extent of impact varied. Triton X-100 and similar surfactants may prove to be valuable tools to protect cell viability in electrokinetic microdevices.

The impact of Faradaic reactions on electrodes was explored via optical images and surface profiles for the uncoated and HfO_2 coated T-shaped electrodes before and after ~ 15 experiments at $0.10 \text{ V}_{\text{pp}}/\mu\text{m}$ and 1 kHz. The uncoated T-shaped electrodes lost 25 μm of Au layer around the electrode edge, while the HfO_2 coated electrodes show smooth cross-sections of the electrode after ~ 15 experiments.

In summary, the fundamental explorations discussed herein help inform the next generation of electrokinetic microdevices by exploring the effect of Faradaic reaction byproducts on buffer solutions and cells. This work adds additional insight to previously reported altered solution properties and cell behaviors [16, 17]. Our study fills a critical gap in determining the extent of Faradaic reactions around and above the electrode charging frequency in electrokinetic microdevices and in providing a) a plausible way to prevent electron transfer between electrodes and electrolyte solutions via a dielectric HfO_2 coating as well as b) a surfactant tool to protect cell membranes from ionic disruption.

Chapter 4: Investigating the Impact of Low Concentration Surfactant on Red Blood Cell Dielectrophoretic Responses

Cell dielectrophoretic responses have been extensively studied for biomarker expression, blood typing, sepsis, circulating tumor cell separations, and others. Surfactants are often added to the analytical buffer in electrokinetic cellular microfluidic systems to lower surface/interfacial tensions. In non-electrokinetic systems, surfactants influence cell size, shape, and agglomeration; this has not been systematically documented in electrokinetic systems. Impacts of Triton X-100 surfactant with human red blood cells (RBCs) were explored via ultraviolet-visible spectroscopy (UV-Vis) and dielectrophoresis (DEP) to compare non-electrokinetic and electrokinetic responses, respectively. UV-Vis spectra of Triton X-100 treated RBCs were dramatically different from that of native RBCs. DEP motion of RBCs were compared to RBCs treated with low concentrations of Triton X-100 (0.07-0.17 mM) to ascertain surfactant effects on dielectric properties. A star-shaped electrode design was used to quantify RBC dielectric properties by fitting a single-shell oblate cell model to experimentally-derived DEP spectra.

4.1 Introduction

Microfluidic and microdevice platforms leverage micron-scale dimensions for molecular and cellular analysis enabling lower sample consumption, lower-costs, and shorter responses and quantification times. Advances in microfluidic platforms could transform patient access via point of care medical diagnostics; the need for which was

recently articulated in the World Health Organization's List of Essential In Vitro Diagnostics and included blood hematocrit determination (#1) [51], blood typing (#9), [156], and malaria diagnosis (#21) [31, 164].

Microfluidics frequently employ electrokinetics due to simplicity and precise molecular control; dielectrophoresis (DEP) is a powerful and flexible tool capable of discerning molecular expression on cell membranes for blood typing [156], monitoring sepsis [165, 166], circulating tumor cell separations [167], and stem cell separations for therapeutic applications [70, 168]. DEP is field induced polarization and translational motion of polarizable particles or cells in non-uniform AC electric fields.[66] Microelectrodes positioned in a spatially non-uniform geometry delivering AC potential have achieved a plethora of particle/cell separations [169], trappings [170], and other manipulations [64, 171, 172]. Performing DEP within microfluidic platforms allows (sub)cellular electrical property characterizations such as permittivity and conductivity of membrane and cytoplasm. DEP frequency dependent responses have been used to obtain cell population distributions of surface biomarkers, cellular function, and biological mechanism via studying cell's membrane barrier functionality and cytoplasm composition [173, 174]. However, variations confound reproducibility and comparisons between platforms or patients [175].

Surfactants have been widely used in microdevice platforms to achieve droplet generation and stabilization [101], lyse cells [103], reduce Joule heating [102], control electrolysis [39], split conglomerated cells/particles [50, 52, 53, 86], and prevent biomolecule adsorption to aqueous, non-aqueous, or solid interfaces [86, 104]. Low

concentrations (<1%) of non-ionic surfactants are routinely added to cell-buffer solutions to increase accuracy and reproducibility within microfluidic platforms without disrupting protein content of cell membranes or cell viability [51, 54, 101-103]. However, in non-electrokinetic and non-microfluidic systems, surfactant molecules have been observed to interact with the cell membrane by disrupting the normal lipid bilayer architecture and reducing membrane surface tension. Therefore, the effect of surfactants on the cell membranes during electrokinetic manipulations should be investigated prior to using surfactants in microfluidics. DEP was employed to explore these effects because it can provide insights into the dielectric properties of the cell membrane.

Red blood cells (RBCs) are excellent models to study surfactant interactions with cell components such as membranes and cytoplasm because RBCs have a simpler structure lacking a nucleus [176]. In non-electrokinetic and non-microfluidic systems, surfactant and cell membrane interactions are concentration dependent. Above the critical micelle concentration (CMC), surfactants solubilize cell membranes yielding hemolysis, while they protect cell membranes below the CMC [54, 105-108, 154, 177]. This biphasic behavior has been observed for both ionic and non-ionic surfactants. However, microfluidic applications tend to utilize non-ionic surfactants to minimize conductivity disruptions, and protein conformational changes. Non-ionic examples include poly[oxyethylene (n) nonylphenol] [105], polyoxyethylene alkyl ethers [106], octyl- β -D glucopyranoside [107], and Triton [108]. Two different mechanism have been proposed to explain the osmotic resistance (e.g. reduced lysis) of RBCs below the CMC. At low concentrations, surfactant molecules insert into the cell membrane causing membrane cell

enlargement by lowering the lateral surface tension. Thus, RBCs swell and increase the critical lytic volume [178, 179]. The second proposed mechanism is an increase in membrane permeability due to diffusion rate changes through the cell membrane [178, 179]. Effective membrane permeability is an important parameter in cell electrophysiology, since it ultimately influences membrane dielectric constant and permittivity [180]. Thus, we hypothesize that surfactant molecules can intercalate within the RBC's membrane and potentially change both cell radius as well as membrane charge distribution and permittivity, both of which can be discerned from measured DEP spectra.

4.2 Dielectrophoresis Theory and Background

Dielectrophoresis utilizes AC signals to manipulate particles or cells within a medium. The dielectrophoretic force (\vec{F}_{DEP}) on a homogenous spherical particle (rough first approximation to a cell) is given by [66]:

$$\vec{F}_{DEP} = 2\pi r^3 \epsilon_m \text{Re}[f_{CM}] \nabla \vec{E}_{rms}^2 \quad (4-1)$$

where r is the outer particle (or cell) radius, $\text{Re}[f_{CM}]$ is the real part of the Clausius–Mossotti factor (f_{CM}), and $\nabla \vec{E}_{rms}^2$ is the electric field gradient squared. The Clausius–Mossotti factor predicated positive and negative DEP responses can be defined as follows [66]:

$$f_{CM} = \frac{\epsilon_p^* - \epsilon_m^*}{\epsilon_p^* + 2\epsilon_m^*} \quad (4-2)$$

where ϵ_p^* and ϵ_m^* are the complex permittivity of the particle and medium, respectively. Complex permittivity is dependent upon $\epsilon^* = \epsilon + \sigma/j\omega$, where ϵ is the permittivity, σ is the conductivity, ω is angular frequency, and j is $\sqrt{-1}$. If the particle's complex

permittivity is greater than the complex permittivity of the medium ($f_{CM} > 0$), the net force on the particle is toward the maximum electric field strength regions: up the electric field gradient with a positive DEP (p-DEP) force. If complex permittivity of the particle is lower than the medium ($f_{CM} < 0$), the net force direction is towards the minimum electric field strength regions: down the gradient with negative DEP (n-DEP) force. The frequency at which the net force is zero and cell responses gradually shift from n-DEP to p-DEP or from p-DEP to n-DEP spectra is termed the crossover frequency (f_{co}).

4.2.1 Single-Shell Oblate Particles

The magnitude and direction of DEP forces depend highly on cellular shape and composition [181]. Deviation from homogenous cell sphericity significantly reduces accuracy of equation (4-1). RBCs are biconcave disks filled with cytoplasm and no nucleus. Thus, RBCs can be described as single-shell oblate spheres with relatively conductive cytoplasm surrounded by thin dielectric membranes [128, 129]. Typically, the dielectric shell model, subjected to DEP forces, exhibits frequency dispersion. RBCs exhibit α - (sub-Hz to kHz), β - (kHz to MHz range), and γ - (MHz to GHz range) frequency dispersion. This work explores 300 to 700 kHz in the β -dispersion region whereby RBC membranes are conductive and polarized via Maxwell–Wagner interfacial polarizations [66]. Charge distributions on membrane surfaces change due to dynamic polarization effects as the frequency changes. Treating RBCs as a single-shell oblate spheroid with a long semi-major r radius and a semi-minor c radius, where c is the cell half-length, results in a DEP force expression as [30]:

$$\vec{F}_{DEP} = \frac{3}{2} V_c \epsilon_m \text{Re} [f_{CM}] \nabla \vec{E}_{rms}^2 \quad (4-3)$$

where V_c is the cell volume and the single-shell oblate spheroid f_{CM} is [30]:

$$f_{CM} = \frac{\epsilon_p^* - \epsilon_m^*}{3A_{oc}\epsilon_p^* + 3(1-A_{oc})\epsilon_m^*} \quad (4-4)$$

where A_{oc} is depolarization from outside the membrane to infinity which reflects the effects of outer membrane (shell) interactions and distortions to the local electrical field.

For a single-shell oblate model, the complex permittivity of the cell is function of the membrane complex permittivity (ϵ_{mem}^*) and the cytoplasm complex permittivity (ϵ_{cyto}^*) can be determined as follows [30, 32, 128]:

$$\epsilon_p^* = \epsilon_{mem}^* \frac{\epsilon_{mem}^* + (\epsilon_{cyto}^* - \epsilon_{mem}^*)[A_{IC} + v(1-A_{OC})]}{\epsilon_{mem}^* + (\epsilon_{cyto}^* - \epsilon_{mem}^*)[A_{IC} - vA_{OC}]} \quad (4-5)$$

where A_{IC} is the inner membrane depolarization factor, and v is the ratio of outer-membrane volume to inner-membrane volume and can be calculated via $v = r^2 c / [(r + d)^2 (c + d)]$ where d is membrane thickness. Since a RBC's thickness is three orders of magnitude less than its radius, the approximation $A_{IC} = A_{OC}$ is valid and can be calculated as follows [30, 32]:

$$A_{IC} = A_{OC} = -\frac{\gamma^2}{2(1-\gamma^2)} + \frac{\gamma\pi}{4(1-\gamma^2)^{1.5}} - \frac{\gamma}{2(1-\gamma^2)^{1.5}} \left[\text{Arctan} \left(\frac{\gamma^2}{1-\gamma^2} \right)^{0.5} \right] \quad (4-6)$$

where $\gamma = c/r$ for inner membrane depolarization, and $\gamma = (c + d)/(r + d)$ for outer membrane depolarization. For a spherical cell, $\gamma = 1$ and $A_{OC} = 0.33$, which means that equation (4-4) can be simplified to the f_{CM} expression presented in equation (4-2). Healthy human red blood cells have a semi-major radius $r = 3.2 \mu\text{m}$, $A_{OC} = 0.2361$ [30, 32]. Reported parameters for RBC (blood type unspecified) membrane conductivity,

cytoplasm conductivity, and media conductivity are $<10^{-6}$ S/m, 0.31 ± 0.03 S/m, and 0.1 S/m, respectively. The membrane permittivity, cytoplasm permittivity, and media permittivity reported were 10.5 ± 0.45 , 59 ± 6 , and 80, respectively [32].

4.2.2 Quantifying DEP Spectra from Cell Velocities

The DEP force (\vec{F}_{DEP}) acting on cells can be determined by measuring cell velocities (\vec{v}) [23]. If Brownian motion and buoyancy forces are neglected, the net DEP force is the sum of the Stokes drag force (\vec{F}_D) and the acceleration force (\vec{F}_A): $\vec{F}_{DEP} = \vec{F}_D + \vec{F}_A$. For an oblate spheroidal cell, the DEP force can be described as [182]:

$$\vec{F}_{DEP} = m\vec{a} + 6\pi\eta f r \vec{v} \quad (4-7)$$

where \vec{a} is acceleration, η is the fluid's dynamic viscosity, and f is the friction factor derived from the cell's size, shape, and surface roughness. For an oblate cell spheroid (with $\gamma < 1$) whose motion is perpendicular to the symmetry axis, f was derived analytically to be [131]:

$$f = \frac{8}{3} \left(\frac{3-2\gamma^2}{(1-\gamma^2)^{1.5}} \arcsin(1-\gamma^2)^{0.5} - \frac{\gamma}{1-\gamma^2} \right)^{-1} \quad (4-8)$$

One of the key elements of a DEP spectra is f_{CO} since cell's dielectric properties can be evaluated from this number. The crossover frequency is an easily discernable point from experiments that depends upon the cell dielectric properties relative to the suspending medium. Each cell has a unique dielectrophoretic spectra as a function of frequency that reflects molecular structure and dielectric properties of both the cell's surface and internal structure. A single-shell model has two interfaces: the inner interface between the cytoplasm and the membrane and the outer interface between the membrane

and the surrounding medium. Multiple interfaces lead to the possibility of multiple f_{CO} 's. The lower f_{CO} is determined by cell size, shape, and the outer membrane interface in the β -dispersion region, while the second, higher f_{CO} is influenced by the cell cytoplasm and inner interface. Using the lower f_{CO} in combination with the minima and maxima of the DEP response spectra, membrane dielectric properties (permittivity, conductance, and capacitance) can be estimated. RBC membranes can be assumed to be less conductive than the cytoplasm. Under these conditions, by setting $Re[f_{CM}] = 0$ in equation (4-4) we obtain the crossover frequency as follows [32]:

$$f_{CO} = \frac{A_{OC}}{2\pi br C_{mem}} \sqrt{\left[\sigma_m - \frac{br G_{mem}}{A_{OC}} \right] \times \left[\frac{1-A_{OC}}{A_{OC}} \sigma_m + \frac{br G_{mem}}{A_{OC}} \right]} \quad (4-9)$$

where $b = c / (2c + r)$ and C_{mem} and G_{mem} are the specific capacitance and conductance of the cell membrane, respectively [32]. Membrane capacitance is a measure of the membrane area that acts as a charge barrier, and depends upon the membrane thickness, composition/dielectric properties, and morphological complexity. Membrane conductance, on the other hand, reflects the net transport of ionic species across the membrane through pores, ion channels, and defects under the influence of the applied field. As equation (4-9) demonstrates, f_{CO} provides a means for monitoring localized changes in cell membrane capacitance and conductance. Thus, measuring cell DEP behavior can infer cell dielectric properties, which can then be judiciously harnessed to compare, identify, and separate cells of interest. Due to prior knowledge of RBC f_{CO} , the frequency range utilized in this study was from 700 kHz to 300 kHz, whereby Maxwell–Wagner polarizations occur at the interface between the cell membrane and the

suspending medium [66]. Therefore, it becomes possible to probe surfactant interactions with the RBC membrane by quantifying and analyzing the DEP spectra of RBCs.

We test this hypothesis by investigating the effects of non-ionic surfactant Triton X-100 on DEP responses of RBCs in microfluidic devices. Concentrations of Triton X-100 below the CMC (CMC= 0.22 to 0.24 mM) were added into isotonic RBC suspensions in phosphate buffer saline (PBS) subjected to non-uniform electric fields [183]. The impacts of low surfactant concentrations on RBCs were systematically compared across traditional non-electrokinetic cell characterization techniques (UV-Vis spectroscopy and optical microscopy) as well as via an electrokinetic pathway involving DEP characterizations. We calculated cell dielectric properties from experimentally quantified cell velocities converted into DEP force spectra as a function of frequency. This work provides mechanistic understanding into the chemical interactions between a non-ionic surfactant and RBC membranes inferred from DEP cell responses in a microfluidic platform.

4.3 Materials and Methods

4.3.1 Chemicals and preparation

Potassium phosphate monobasic (ACS, $\geq 99\%$) and potassium phosphate dibasic (ACS, $\geq 99\%$) were purchased from EMD Millipore (Billerica, MA, USA). Dextrose (anhydrous, $\geq 99.5\%$), and nonionic surfactant Triton X-100 (laboratory grade) were purchased from Sigma-Aldrich (St. Louis, MO, USA). Sodium chloride ($>99\%$, ACS) was purchased from Macron Chemicals (Center Valley, PA, USA).

Phosphate Buffered Saline (PBS) was made from the following salts. All RBC experiments were conducted in controlled isotonic PBS solution with a conductivity of 0.1 S/m. To prepare PBS stock solution, 2.7 g of potassium phosphate monobasic, 3.5 g of potassium phosphate dibasic, and 1.2 g of sodium chloride were mixed in 99.9 mL of E-pure water (18.2 $\Omega\cdot\text{cm}$, EMD Millipore Simplicity Ultrapure 185, Billerica, MA, USA). To formulate PBS solution with the conductivity of 0.1 S/m, 1.2 g of dextrose and 64.3 μL of PBS stock solution were mixed in 24.9 mL of E-pure water, stored at 4 °C and used within one week.

4.3.2 Microfluidics Design and Fabrication

To study the impact of Triton X-100 surfactant concentrations on red blood cells, a star-shaped electrode microfluidic device was used. The star-shaped electrode design had four pairs of triangular electrodes converging symmetrically at a center point [16, 17]. The planar electrodes were fabricated with a thickness of 95 nm of Au above 10 nm Cr sputtered onto 25×76×1mm glass microscope slides (AmScope.com). Photolithography, sputtering, and lift-off were employed to fabricate the microelectrodes on glass microscope slides following previously detailed procedures [16, 17]. Briefly, a master wafer was created by photolithography to obtain polydimethylsiloxane (PDMS) castings. Microelectrodes were then overlaid by the PDMS circular microfluidic chamber with a diameter of 590 μm and a depth of ~ 70 μm . Disposable biopsy punches (Robbins Instruments, Chatham, NJ, USA) were utilized to create inlet and outlet ports with diameters of 300 μm .

4.3.3 Blood Experiments

Human blood samples from anonymous donors were obtained following IRB-approved protocols (M0540, [318164-12]) and stored at 4°C, then tested on the day of donation. Blood was centrifuged at 132 rcf for 10 min. Supernatant plasma was removed, and the packed RBCs were washed twice with isotonic 0.9% wt/v NaCl solution via cycles of resuspension and centrifugal separation. For experiments, RBCs were mixed with 0.1 S/m PBS at 1.0% v/v. For the surfactant study, RBCs were also resuspended to 1.0% v/v while achieving final Triton X-100 concentrations of 0.00, 0.07, 0.11, 0.17, and 0.50 mM.

4.3.4 UV-Vis Experiments

Ultra Violet Visible absorption spectroscopy is one of the simplest, label-free techniques yielding direct insight into size, shape, chemical composition, and optical properties of cells and/or proteins [184, 185]. UV-Vis absorbance readings and spectral profiles were obtained using a Genesis 10 UV scanning spectrophotometer (Thermo Fisher Scientific, Waltham, MA, USA). UV-Vis was utilized as a non-electrokinetic technique to study both hemolysis and RBC integrity.

4.3.4.1 Hemolysis

The extent of hemolysis over time was studied by exposing different concentrations of Triton X-100 (0.00, 0.07, 0.11, 0.17, and 0.50 mM) to RBCs. Samples were kept in ambient conditions (25°C) and were performed in triplicate within cuvettes (Spectrocell Inc, Oreland, PA, USA). Negative controls were comprised of RBC suspensions in PBS

in the absence of Triton X-100 (0.00 mM). Positive controls were 0.50 mM RBC/Triton X-100 whereby 100% lysis was expected [186, 187]. After 2 hours, RBC surfactant and non-surfactant suspensions were centrifuged at 132 rcf for 10 min. The supernatant was collected and used to measure free hemoglobin absorbance readings at 380, 415, and 450 nm. A PBS blank control was used to correct absorbance of free hemoglobin ($Ab_{free\ hemoglobin}$) [186, 187]:

$$Ab_{free\ hemoglobin} = 2 \times A_{415} - (A_{380} + A_{450}) \quad (4-10)$$

Hemolysis extent was determined by measuring UV-Vis absorbance of free hemoglobin (Hb) released from the RBCs [186, 187]. Changes to the Hb absorption spectrum could be discerned using the Soret band ($\lambda_{max} = 415\text{ nm}$).

$$Hemolysis[\%] = \frac{Ab_{free\ hemoglobin\ of\ test\ sample}}{Ab_{free\ hemoglobin\ of\ positive\ control}} \times 100\% \quad (4-11)$$

Percent hemolysis was calculated relative to the 100% hemolysis positive control to compare across surfactant exposure conditions. Statistical analysis was conducted whereby * represents p-values <0.05 and ** represents p-values <0.01. Both * and ** were considered statistically significant differences.

4.3.4.2 RBC integrity and cell diameter

RBC health and integrity were studied by exposing different concentrations of Triton X-100 (0.00, 0.07, 0.11, and 0.17 mM) to RBCs over time (0, 30, 60, and 120 min). Samples were diluted in 0.25% v/v RBC/PBS and kept in ambient conditions (25°C) to

obtain the spectra. UV-Vis spectrums were obtained from 250–750 nm in 1 nm increments.

For each solution condition, RBC radii ($n \sim 100$) were concurrently measured with ImageJ® software (NIH, <https://imagej.nih.gov/ij/>) from 2D microscopy images Zeiss Axiovert microscope (Zeiss, Oberkochen, Germany). RBC cell radii histograms were plotted to represent the cell size distribution of each cell population. Mean and standard deviation of cell radius were also reported. Statistical analysis was conducted whereby * represents p-values <0.05 and ** represents p-values <0.01 . Both * and ** were considered statistically significant differences.

4.3.5 Data Acquisition and Analysis

RBC suspensions were introduced via ports to the dielectrophoretic microfluidic device mounted on the Zeiss Axiovert microscope. Low frequency alternating current electric fields were applied via a custom-built function generator (Microdevice Engineering Inc., Houghton, MI, USA). To monitor impacts on RBC membranes, experiments were conducted at 5 V_{pp} potential (electric field density = $0.1 \text{ V}_{pp}/\mu\text{m}$) over a frequency range from 700 kHz to 300 kHz and a frequency sweep rate of 2400 Hz/s. The electric field density was calculated from the applied potential over the distance between opposing electrode tips (50 μm). Once the potential was applied, cell movement was recorded at 10X magnification at 1 fpm for 167 seconds.

COMSOL Multiphysics® (Burlington, MA, USA) simulation software was utilized to map the non-uniform electric field distribution and gradient in star-shaped shape electrode designs. The *Electric Potential* boundaries were set to *Ground* and 5 V_{pp} for Au

ground and working electrodes, respectively, while all outer boundaries were set to *Electrical Insulation*. The electric field gradients were then achieved by solving Laplace's equation using the Lagrange element method. As shown in Figure 4-1, the star-shape device was designed to yield symmetric electric field non-uniformities to induces DEP motion in polarizable cells. Cells in red, orange, and yellow regions in Figure 4-1-c experienced a greater DEP force than cells in green, teal, and blue regions. Thus, to make appropriate comparisons, cells were selected for analysis from similar electric field gradient regions to accurately and reproducibly quantify cell displacement. This data was used to calculate cell velocity and subsequently individual cell's DEP force. Cells initially located in the electric field strength regions between lines marked I and II in Figure 4-1-c and Figure 4-1-d (inset) were tracked forward in time. Figure 4-1-d plots the electric field gradient along lines I and II. Cell velocities were only quantified for cells in the shaded region of interest.

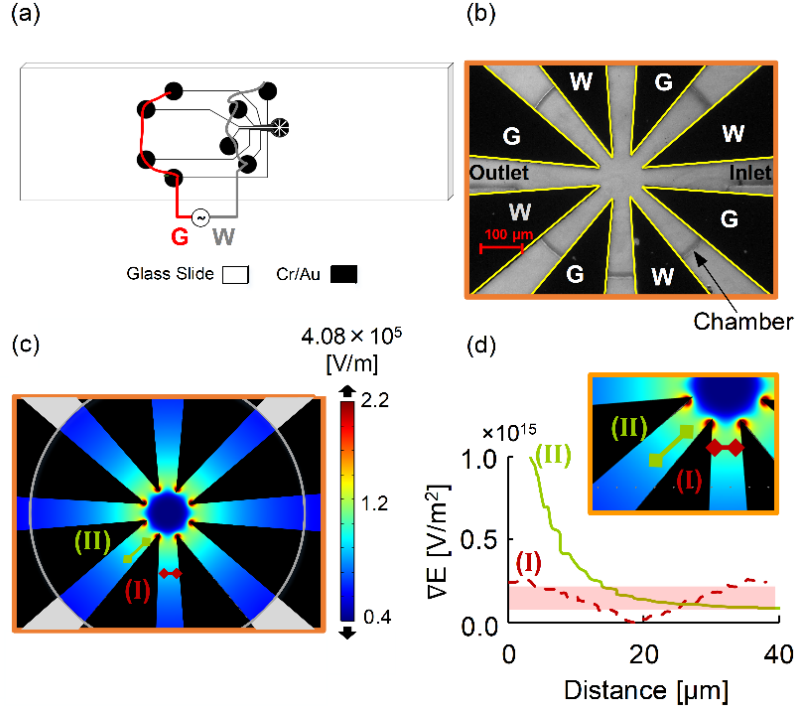


Figure 4-1: Microfluidic device configuration with a PDMS fluidic layer bonded on a Cr/Au electrode glass slide. (a) Macroscale schematic demonstrates the Cr/Au star-shaped electrode design in black on a glass slide. (b) Microscope (10X) image of the star-shaped microelectrodes within the circular chamber. (c) The electric field (V/m) distribution in the microfluidic chamber. Regions around electrode tips have the maximum field strength. (d) Plotted cutline of the electric field gradient approximately parallel to the electrode side is shown in green line marked II, while the electric field gradient (V/m²) perpendicular to the working and ground electrode is shown in dash red line marked I. Location of green and red cut lines are shown in (c) and inset (d).

Semi-automated and automated techniques were compared for analyzing cell displacement. The semi-automated technique with ImageJ® utilized recorded images to manually acquire cell displacement with time. Data was compiled into MATLAB to calculate the cell velocity and \vec{F}_{DEP} . The automated technique employed Tracker 4.11.0 software (<https://physlets.org/tracker/>) to directly obtain velocity profiles. Finally, equation (4-7) was utilized to calculate the dielectrophoretic force which was plotted for samples without and with Triton X-100 concentrations of 0.07, 0.11, and 0.17 mM. RBC sizes (measured previously) were utilized to adjust \vec{F}_{DEP} calculation.

4.4 Results and Discussion

This study examined the interactions of low concentrations of Triton X-100 surfactant below the CMC with human RBCs using UV-Vis spectroscopy for cell integrity, optical microscopy for cell size, and dielectrophoretic techniques for membrane dielectric properties.

4.4.1 Hemolysis and Cell Size Dependence on Triton X-100 Concentrations

Red blood cell integrity in the absence and presence of Triton X-100 was examined via traditional UV-Vis spectroscopy techniques [186, 187]. Figure 4-2-a shows hemolysis percentages obtained via equations (4-10) and (4-11). The positive control of 0.5 mM Triton X-100 was selected as more than twice the CMC = 0.22 mM and yielded 100% hemolysis [183]. The negative control of RBCs in isotonic PBS (0.1S/m) showed 4.05% hemolysis which can be attributed to slight osmotic pressure changes and/or stress from centrifugation. Hemolysis percentages of 1.20% and 1.67% for 0.07 and 0.11 mM Triton X-100 treated RBCs, respectively, were notably lower than native RBCs (negative control, *, p-value <0.05). In 0.17 mM Triton X-100, hemolysis was 5.94% which is considerably higher compared to 0.07 and 0.11 mM Triton X-100 (**, p-value <0.01). These results are consistent with previously reported biphasic phenomena [178, 179], and further suggest that below the CMC there is a narrow range of Triton X-100 concentrations whereby hemolysis is reduced from native conditions and the surfactant protects RBCs against rupture.

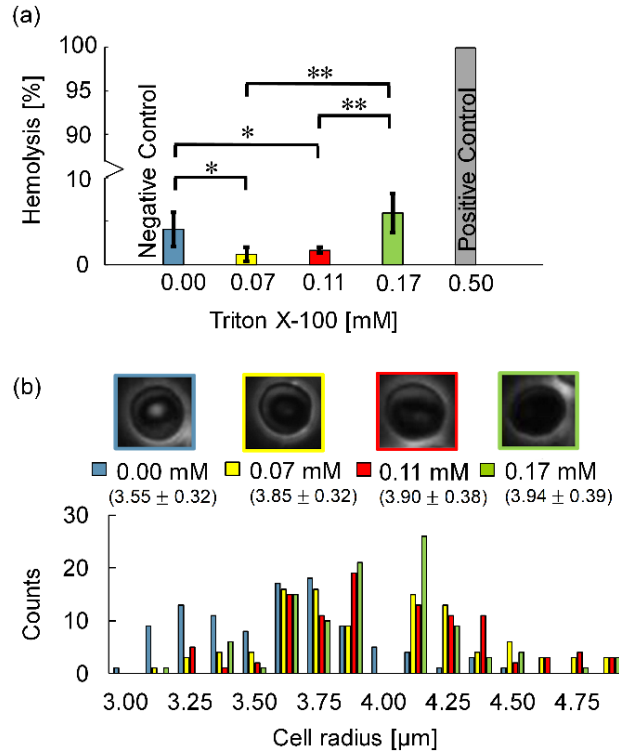


Figure 4-2: (a) The impact of 0.00, 0.07, 0.11, 0.17, and 0.50 mM Triton X-100 on percent hemolysis. Hemolysis is decreased by 2.9% upon adding 0.07 mM Triton X-100, then increases by 4.7% as the concentration of Triton X-100 increases from 0.07 to 0.17 mM. Significance of differences between hemolysis was determined by calculating p-values; * represents p-values <0.05 and ** represents p-values <0.01 . (b) Microscopy images of RBCs, mean and histogram of RBC radii at 0.00, 0.07, 0.11, and 0.17 mM Triton X-100 concentrations. RBC radii increased with Triton X-100 concentrations, which are also noted in Table 4-1.

As surfactant molecules intercalate into cell membranes [54, 105-108, 154, 177], they reduce strain within the membrane allowing cell volume to increase. This mechanism elevates the threshold for hemolysis, aka the critical lytic volume [178, 179]. When cell volume increases exceed the critical lytic volume, hemolysis occurs. Figure 4-2-b shows cell radii distribution histograms, cell morphology, and mean radii for the RBC populations in the absence and presence of sub-CMC Triton X-100 concentrations. Native RBCs typically have a biconcave shape with radii that range between 3.10 to 4.10

μm in isotonic physiological conditions [188]. In the absence of Triton X-100, 75% RBCs were between 3.10 and 4.10 μm . In 0.07 mM and 0.11 mM Triton X-100, this shifted such that 75% of the RBC population had a cell radius between 3.50 and 4.50 μm . As the Triton X-100 concentration increased to 0.17 mM, 85% had cell radii between 3.50 and 4.50 μm . Given the broader size distributions with both the 0.00 and 0.11 mM Triton X-100 treated RBC radii populations, a pair-wise statistical t-test analysis yielded a $p\text{-value} < 0.05$, which is classified as significant [189]. Increasing radii with increasing Triton X-100 concentrations were attributed to the surfactant's intercalation into the RBC membranes thus elevating the critical lytic volumes.

As radii increased, images showed that RBCs lost their biconcave morphology consistent with prior observations [178, 190]. As shown in Figure 4-2-b, RBCs transformed from biconcave with bright circular interiors to stomatocytes with linear slit-like profiles as Triton X-100 concentrations increased from 0.00 to 0.11 mM. At 0.17 mM Triton X-100 concentrations, most RBCs showed swollen spherocyte shapes. Cell size and morphology both influence the dielectrophoretic forces experienced by the cells. The stomatocyte shape can be modeled as oblate single-shell geometry for DEP calculations. To increase accuracy, the DEP model incorporated cell size and morphology as discussed in section E of the Results and Discussion.

4.4.2 RBC Integrity Analysis via UV-Vis Spectroscopy

Beyond the standard hemolysis analysis, UV-Vis absorbance spectra can provide additional insights into the effects of low concentrations of Triton X-100 on RBC membranes and integrity by examining peaks from interior proteins such as hemoglobin.

When a RBC membrane ruptures and the cell lyses, the interior contents of the cell are exposed to the surrounding media initiating secondary degradation reactions such as oxidation of hemoglobin [191, 192]. Figure 4-3 shows absorbance from 250 to 750 nm wavelengths for native and Triton X-100 treated RBC suspensions. Hemoglobin free in solution demonstrates characteristic absorption peaks of the Soret band at 415 nm and α and β bands at 576 and 541 nm, respectively (Figure 4-3) [193-201]. Hemoglobin proteins are comprised of four heme groups; two within α chains and two within β chains [184, 185]. As shown previously, Soret bands are indicative of free hemoglobin absorbance and can be used to calculate the extent of hemolysis (equations (4-10) and (4-11)) as well as hemoglobin monodispersity [186, 187]. Moreover, the peak shape, wavelength, and absorption maximum intensity of Soret and α/β bands can be utilized to monitor free hemoglobin, heme oxidation, orientation and protein denaturization [193-201]. Upon Triton X-100 addition to the RBC suspensions, the wavelength position of the Soret, α , and β bands did not change over 120 min for any concentration (Figure 4-3-a-d). Thus, changes in the peak shape and absorbance intensity of the Soret, α , and β bands were used to ascertain Triton X-100 surfactant impacts over time (Figure 4-3-a).

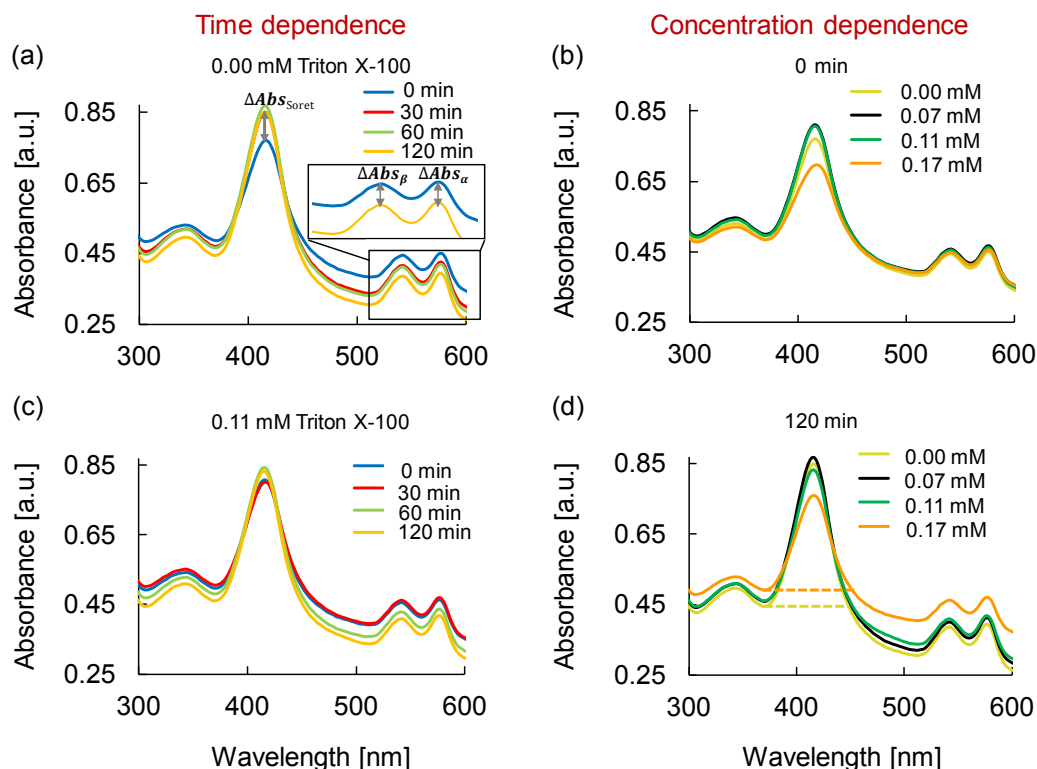


Figure 4-3: UV-Vis absorbance spectra of 0.25 v/v% RBC/PBS from 250 to 750 nm. Time dependence was studied for (a) native RBCs (0.00 mM Triton X-100) and (c) 0.11 mM Triton X-100 treated RBCs at 0, 30, 60, and 120 min. Concentration dependence was studied for RBCs treated at 0.00, 0.07, 0.11, 0.17 mM Triton X-100 at (b) 0 min and (d) 120 min. Changes in α and β peak absorption (ΔAbs_{α} and ΔAbs_{β}) indicate α and β heme chain oxidation/protein degradation while the Soret band (ΔAbs_{Soret}) provides information on the extent of hemolysis.

Comparison of spectra in Figure 4-3-a and Figure 4-3-c illustrate native RBCs (0.00 mM Triton X-100) and 0.11 mM Triton X-100 treated RBCs, respectively as a function of time. For native RBCs, the Soret peak intensity increased by 10.3% over 120 min, which is an indication of slight increase in free hemoglobin as a result of baseline hemolysis (negative control) [186, 187, 202]. Further, the intensity of the native α and β peaks at 576 and 541 nm decreased within 30 min, and after 120 min, the peaks decreased by 12.7% and 13.3%, respectively (Figure 4-3-a). These peak decreases are

indicative of baseline heme oxidation [196-198]. Spectra for 0.11 mM in Figure 4-3-c illustrate an increase of 3.10% for the Soret peak after 120 min. Comparison between these Soret band increases of 10.3% and 3.10% for 0.00 mM (native) and 0.11 mM is consistent with previously reported biphasic phenomena [178, 179] whereby the presence of Triton X-100 reduced free hemoglobin by reducing hemolysis.

Heme changes can be inferred from α and β peaks. Changes in α and β peak intensity occurred for 0.11 mM Triton after 30 min but before 60 min with decreases of 10.3% and 9.96%, respectively after 120 min. Thus, heme oxidation is hindered slightly in the presence of 0.11 mM Triton, consistent with the Soret band conclusion that RBC membranes remained intact for longer when Triton X-100 molecules were present. Similar heme UV-Vis spectral trends were obtained for 0.07 mM Triton X-100 treated RBCs [data not shown]; the Soret band increased by 7.03% while α and β peak intensities decreased by 12.0% and 12.8%. Trends differed slightly for 0.17 mM as discussed below.

Figure 4-3-b and Figure 4-3-d show the concentration dependent impacts for 0.00, 0.07, 0.11, and 0.17 mM Triton X-100 treated RBCs at 0 and 120 min, respectively. At time 0, the spectra are nearly identical for Triton X-100 concentrations from 0.00 to 0.11 mM with less than 4.59% variation in the 415 nm Soret band (Figure 4-3-b). However, the 0 min Soret band intensity decreased by 9.48% for 0.17 mM Triton X-100 compared to the native RBC sample. This result was puzzling and inconsistent with previous measures of hemolysis. However, previous work reports that a change in hemoglobin structure can cause a profound and abrupt decrease in the absorption maximum of the Soret band (Figure 4-3-b) [203]. The Soret peak shape broadened by ~12 nm with 0.17

mM Triton X-100, which is an indicator of protein denaturation via a conformational change within the heme region [200, 201]. From the initial reading at time 0 to 120 min, the Soret peak intensity for 0.17 mM Triton X-100 increased by 9.03% indicative of an increase in free hemoglobin (compare Figure 4-3-b and Figure 4-3-d). Further, the intensities of both α and β peaks changed by only 3.12% and 3.07% over the 120 min (compare Figure 4-3-b and Figure 4-3-d), which is considered insignificant oxidization.

In summary, UV-Vis spectral analysis of hemoglobin served as an indirect indicator of RBC membrane integrity because relative Soret, α and β peak absorptions changed once hemoglobin was released from the cell into the surrounding solution. Subsequent heme oxidation/protein degradation of the heme chains begin upon hemoglobin exposure to the PBS. In general, hemolysis increased with time and decreased with Triton X-100 concentrations. After examining RBCs in Triton X-100 via these traditional RBC characterization techniques (UV-Vis spectroscopy and optical microscopy), electrokinetic characterizations were explored.

4.4.3 Qualitative Dielectrophoretic Behavior

RBC membrane charge properties were further explored by correlating cell size and dielectrophoretic (DEP) responses of RBCs because these properties directly correlated with membrane polarization and integrity. The AC frequency range at which cells transition their movement from negative DEP to positive DEP was determined by applying a $0.1 \text{ V}_{pp}/\mu\text{m}$ signal with a frequency sweeping from 700 to 300 kHz between four pairs of converging triangular and planar Cr/Au electrodes (Figure 4-1). The frequency sweep was conducted from high to low frequency because the DEP forces cells

experience while undergoing p-DEP at higher frequencies are larger in magnitude than those trapped at electric field minima while experiencing n-DEP (equations (4-1) and (4-7)). All DEP experiments were conducted after RBCs were at steady state, which was contact with Triton X-100 concentrations for 2 hours. Previous studies revealed that p-DEP to n-DEP frequency sweep transitions yielded more reproducible and accurate results than static frequency tests [173].

The p-DEP to n-DEP transition was explored as a function of Triton X-100 concentrations below and approaching the CMC (0.22 to 0.24 mM) since isolated and dispersed surfactant molecules show minimal lysing effects [54, 105-108, 154, 177], while surfactant molecules assembled into micelles impact RBC integrity [178, 179, 183]. Figure 4-4 shows images of RBC locations in the microfluidic chamber before, during, and after applying the frequency sweep. Prior to applying the potential, RBCs were uniformly distributed in the chamber (Figure 4-4-a, e, i, and m). Upon applying the sweeping frequency signal, RBCs were pulled toward regions with high electric field density, indicative of p-DEP, then transitioned toward lower electric field density regions indicative of n-DEP. For native (0.00 mM) RBCs, p-DEP occurred from 700 kHz down to 492 kHz (Figure 4-4-a, b, c, and d). DEP forces diminished to zero at the crossover frequency, f_{CO} , of 360 kHz (Figure 4-4-c) and then DEP forces gradually increased to then push the RBCs away from the electrodes towards the electric field minima at the chamber center (Figure 4-4-d). At the low Triton X-100 concentration of 0.07 mM, the p-DEP response was strong, but the crossover was a lethargic transition between 359-381 kHz (Figure 4-4-e, f, g, and h) before achieving n-DEP at 300 kHz. As the surfactant

concentration increased to 0.11 mM (Figure 4-4-i, j, k, and l), a few cells exhibited n-DEP throughout the frequency sweep, while the majority of RBCs exhibited a lethargic f_{CO} between 365-385 kHz and again demonstrated n-DEP at 300kHz. Triton X-100 at 0.17 mM caused cells to uniformly exhibit n-DEP from 700 down to 300 kHz (Figure 4-4-m, n, o, and p). Literature indicates that 0.17 mM Triton X-100 is the lowest concentration to sufficiently permeabilize the RBC membrane prior to complete cell lysis at 0.22 mM (CMC) [204]. Such permeabilization would effect DEP polarizations. Further, UV-Vis spectral results (Figure 4-3) indicated Triton X-100 impacted hemolysis as well as hemoglobin structure at 0.17mM.

RBC size and morphology is also apparent in Figure 4-4-d, h, l, and p whereby the smaller native RBCs tightly pack for n-DEP and comprise a larger portion of the chamber for 0.11 mM Triton X-100. In addition, RBC uniformity is altered for 0.17 mM Triton X-100.

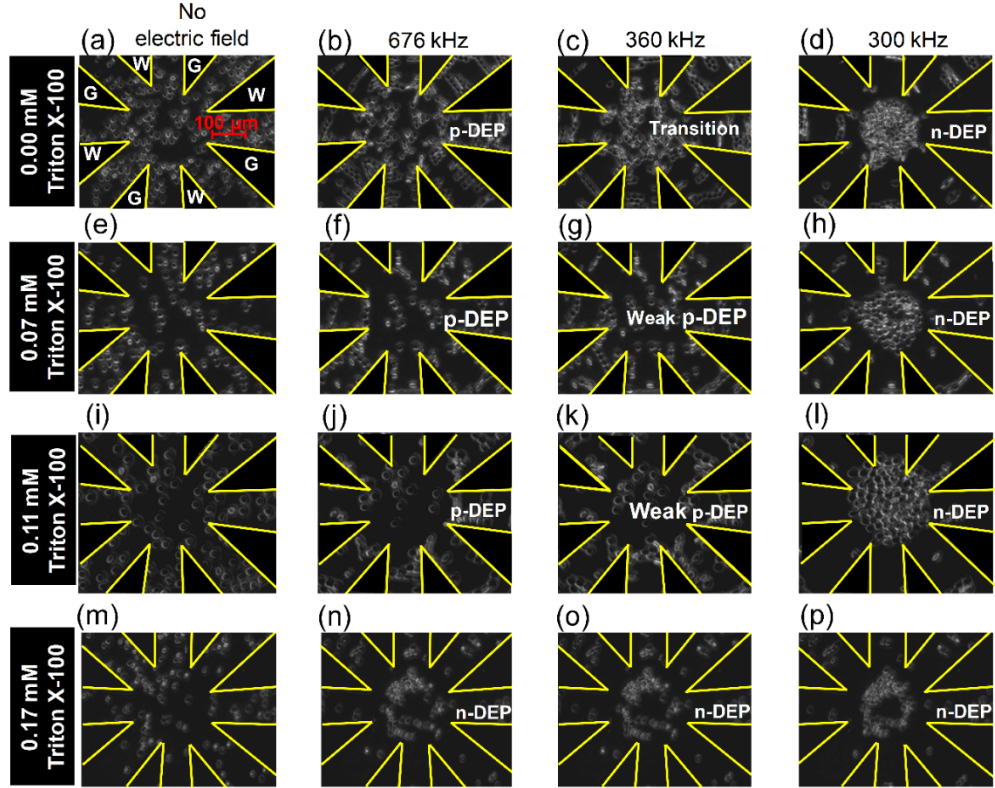


Figure 4-4: Video microscopy images illustrating the time sequence of 1.0 v/v% red blood cells in 0.1 S/m isotonic PBS medium at 0.00 (first row), 0.07 (second row), 0.11 (third row), and 0.17 mM (fourth row) Triton X-100 concentration at $0.1 \text{ V}_{pp}/\mu\text{m}$ from 700 kHz to 300 kHz within star-shaped microfluidic devices. Images are shown at 0 sec (a, e, i, and m) corresponding to no field, 10 secs corresponding to 676 kHz (b, f, j, and n), 142 sec corresponding to 360 kHz (c, g, k, and o), and 167 sec corresponding to 300 kHz (d, h, l, and p). Images illustrate that the p-DEP to n-DEP crossover frequency shifts to lower frequencies with increasing Triton X-100 concentrations. Images also reveal changes in RBC radii and shape as previously quantified in Figure 4-2.

4.4.4 Quantitative Dielectrophoretic Spectra

To better understand surfactant and RBC membranes interactions, DEP spectra were quantified to approximate DEP force versus frequency via both semi-automated and automated analysis techniques as described in the materials and methods section. Agreement between the two analyses was excellent with consistent, but small bias of <10

kHz in the crossover frequency (f_{co}) prediction. Thus, only the automated technique is reported here.

Figure 4-5 shows the DEP force profile inferred from the cell velocities via equation (4-7) of native and Triton X-100 treated RBC suspensions via a box-and-whisker-plot-inspired representation. As the key illustrates in Figure 4-5, the red to grey patterned regions show the first, second, and third interquartile ranges, with boundary lines illustrating the min, median, and max. The min and max lines (or whiskers) bounding the patterned area show the full range of the DEP force. This representation is a concise tool to illustrate the motion of every cell in the microdevice chamber's region of interest.

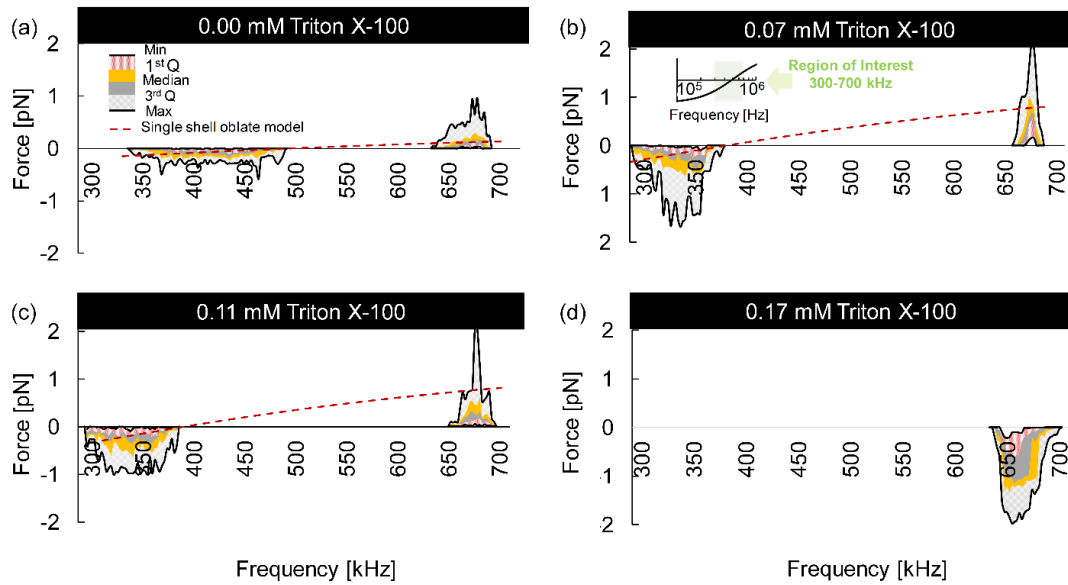


Figure 4-5: Dielectrophoretic force as function of frequency from 300 to 700 kHz of 0.00 mM (native) (a), 0.07 mM (b), 0.11 mM (c), and 0.17 mM (d) Triton X-100 treated RBCs. DEP force profiles were calculated from the cell velocities and represented via a box-and-whisker-inspired representation whereby the colored regions show the interquartile ranges, while the min and max lines for the whiskers show the full force range (patterned area) at all cells in test region. The median force is the boundary between yellow and grey.

The crossover from p-DEP to n-DEP behavior occurs at successively lower frequencies as the Triton X-100 concentration increases. Native cells yielded a f_{CO} of 482 ± 10 kHz while the 0.07 mM treated RBCs yielded 370 ± 11 kHz and 0.11 mM yielded 375 ± 10 kHz. Also apparent is the increase in the magnitude of the maximum positive DEP force, \vec{F}_{DEP} , obtained for Triton X-100 treated samples. Native RBCs experienced an average positive \vec{F}_{DEP} of +0.25 pN and an average negative \vec{F}_{DEP} of -0.15 pN. Treatment at 0.07 mM had the average positive and negative \vec{F}_{DEP} increased to +0.75 and -0.50 pN, respectively. However, Triton X-100 treatment at 0.11 mM only increased DEP forces to +0.65 and -0.50 pN. No f_{CO} was observed for 0.17mM since n-DEP occurred for all frequencies tested. Triton X-100 treatment at 0.17 mM increased the average DEP forces to -1.17 pN. These results suggest that low concentrations of surfactant impacted the strength of RBC membrane polarizations. Several possible membrane polarization mechanisms are capable of shifting the dielectrophoretic spectra and are discussed below.

4.4.5 Single-Shell Oblate Dielectrophoretic Force Model

MATLAB was used to model dielectrophoretic spectra by adjusting parameters in equation (4-9) to best approximate experimentally obtained spectra in the presence and absence of Triton X-100. The single-shell oblate model was used to examine the relative contributions of RBC parameters including radius (r), membrane permittivity (ϵ_{mem}) and conductivity (σ_{mem}), cytoplasm permittivity (ϵ_{cyto}) and conductivity (σ_{cyto}), and medium permittivity (ϵ_m) and conductivity (σ_m). Medium conductivity strongly impacts the cell behavior in the β -dispersion region; however, in our DEP force model, medium

conductivity is kept constant to match the experimental condition. For high frequency AC systems, medium conditions including pH, ionic concentration and ionic strength are assumed relatively stable over time due to negligible electrochemical reactions [16, 17]. Also, in the β -dispersion region, cytoplasm permittivity and conductivity have been shown to have no significant influence on crossover frequency (f_{CO}) [30]. Reported parameters for RBC (blood type unspecified) membrane, cytoplasm, and media conductivity are $<10^{-6}$ S/m, 0.31 ± 0.03 S/m, and 0.10 S/m, respectively [32]. The membrane, cytoplasm, and media permittivity reported were 10.5 ± 0.45 , 59.0 ± 6 , and 80, respectively [32]. Thus, σ_m , σ_{cyto} , and ϵ_{cyto} were held constant in the model at 0.10 S/m, 0.31 ± 0.03 S/m, and 59.0 ± 6 values, while parametric sweeps were conducted for σ_{mem} , r , and ϵ_{mem} . Membrane conductivity was explored over 2 orders of magnitude greater than those of native RBC membranes (10^{-6} S/m) without significantly shifting f_{CO} ; further, when σ_{mem} was reduced to 10^{-4} S/m, f_{CO} shifted down only by 10 kHz, which does not account for the 110 kHz f_{CO} shift observed experimentally. Thus, σ_{mem} was fixed at 10^{-6} S/m for subsequent parametric sweeps exploring the impact of cell radius, and membrane permittivity.

Maxwell-Wagner interfacial polarizations govern cell responses in the β -dispersion region whereby the electric field interacts with ions in the medium causing them to move and align around the cell. Cell size is critical to interfacial polarization; the larger the cell is, the longer the timescale for ions to move around, align, and induce cell polarization. Equations (4-7) and (4-9) explain how cell radius impacts DEP force magnitude and f_{CO} ,

respectively. For this analysis, cell size is accounted for in the radii and quantified from Figure 4-2-b.

Cell radii for 0.00 and 0.07 mM Triton X-100 are shown in Table 4-1. Average radii were utilized as the starting parameters for model fits to the experimental DEP spectra in Figure 4-5. As the cell radius increased from 3.55 to 3.85 μm upon increasing Triton X-100 from 0.00 to 0.07 mM, the computed crossover frequency (f'_{CO}) decreased from 482 to 444 kHz. However, f'_{CO} does not match the experimentally observed $f_{CO} = 370$ kHz. Thus, cell enlargement is not sufficient to account for the decrease in f_{CO} in the presence of 0.07 mM Triton X-100. Similarly, for 0.11 mM Triton X-100 treated RBCs, the model required radii values (5.2 μm) outside the range of experimentally observed cell radii, essentially requiring a 7.3% cell volume increase, which is not feasible without cell lysis.

In addition to cell size effects, the movement and alignment of ions around the cell are influenced by the content and properties of the cell membrane. Thus, as the cell surfaces changes it affects polarization in distinctive ways and cause cells to display discretely different DEP spectra. One possible mechanism is that membrane permittivity solely causes interfacial polarization changes in the presence of Triton X-100. As the membrane permittivity was increased from 10.5 to 13.4, f'_{CO} decreased from 482 to 370 kHz to match the experimentally observed f_{CO} of 370 kHz in the presence of 0.07 mM Triton X-100. Similarly, for 0.11 mM, a membrane permittivity value of 13.3 could achieve $f_{CO} = 375$ kHz. These results suggest that the presence of Triton X-100 makes RBC membranes less permissive.

Table 4-1: Optimized parameters for single-shell oblate DEP polarization model for 0.00, 0.07, 0.11 and 0.17 mM treated RBCs in 0.1 S/m isotonic PBS. Experimentally measured crossover frequency is shown as f_{co} while the model-derived crossover frequency is f'_{co} . Bold parameters were varied (normal font parameters were fixed) in the model to achieve the best agreement with experimental data.

<i>Triton X-100</i> [mM]	f_{co} [kHz]	r^{***} [μm]	ϵ_{mem}	f'_{co} [kHz]	C_{mem} [mF/m ²]
0.00	482 ± 10	3.55 ± 0.32			
*Optimizing cell size and ϵ_{mem} on f_{co}		3.55	10.5	482	11.51
0.07	370 ± 11	3.85 ± 0.32			
Optimizing cell size on f_{co}		3.85	10.7	444	
Optimizing ϵ_{mem} on f_{co}		3.55	13.4	370	
*Optimizing cell size and ϵ_{mem} on f_{co}		3.85	12.7	370	14.05
0.11	375 ± 10	3.9 ± 0.38			
Optimizing cell size on f_{co}		3.9	10.7	432	
Optimizing ϵ_{mem} on f_{co}		3.55	13.3	375	
*Optimizing cell size and ϵ_{mem} on f_{co}		3.9	12.3	375	13.61
0.17	N/A **	3.94 ± 0.39	N/A	N/A	N/A

* Parameters utilized in model DEP spectra fits in Figure 4-5.

** Not applicable.

*** Statistical analysis between cell radius of 0.00 and 0.17 mM Triton X-100 treated RBC populations revealed the p-value <0.05 which indicates a significant difference.

Although the contribution of membrane permittivity is a promising explanation for the observed shift in DEP spectra, cell size can also cause DEP spectral variations. Thus, the optimal mechanism likely includes both cell radius and membrane permittivity contributions to DEP spectral changes. The average cell radius was utilized as a starting parameter in the single-shell oblate model. In the presence of 0.07 mM Triton X-100 as the cell radius was increased from 3.55 to the experimentally measured 3.85 μm, the predicted f'_{co} changed from 482 to 444 kHz (a decrease of 8.6%). Thus, membrane permittivity would need to increase from 10.7 to 12.7 to achieve a f'_{co} drop from 444 to the experimentally observed 370 kHz (a 16% further decrease). This translates to a specific membrane capacitance increase from 11.51 mF/m² for native to 14.05 mF/m² for

0.07 mM Triton X-100 treated RBCs. Similar observations were obtained for 0.11 mM as shown in Table 4-1 whereby C_{mem} decreased to 13.61 mF/m². Cell membrane capacitance depends on the cell dielectric properties, size, shape, and cell surface morphology associated with membrane blebbing or microvilli [205]. These characteristics of membrane folding or smoothing change how charges distribute between the membrane surface and the medium, which shift as a function of frequency and thus contribute to a cell's DEP frequency spectra [206]. Results support the hypothesis that the DEP force acting on a cell in the β -dispersion region was strongly influenced by both the cell radius and membrane permittivity, which ultimately reflected in the cell membrane capacitances report in Table 4-1.

The RBC parameters shown in Table 4-1 are the best fits for the single-shell oblate DEP model to experimentally measured DEP spectra for different Triton X-100 concentrations. The optimized model fit is also shown as the red dashed curve in Figure 4-5-a-d. Using the parameters in Table 4-1, the DEP force spectra agreed in sign and order of magnitude with experimental observations within p-DEP and n-DEP regions. Since the 300 to 700 kHz range is narrow, the model fit appears slightly linear as shown in the inset. One limitation with the cell velocity analysis approach to ascertain DEP force is that the cells move rapidly to an equilibrium position, especially with strong DEP responses. Once in that equilibrium position, additional cell movement is not detected although the DEP force on the cell remains high. This is apparent when comparing Figure 4-5 and Figure 4-4 where a strong negative DEP response is observed, but no additional cell velocities are measured below ~ 650 kHz. Thus, in these steady state periods,

deviations between the experimental data and the DEP polarization model are not real, but a manifestation of the measurement approach.

A DEP force of -1.17 pN for 0.17 mM Triton X-100 was inferred from the initial results between 700 and 640 kHz. As non-ionic Triton X-100 surfactant molecules become more prevalent within the cell membrane structure [54], it follows that the cell membrane's propensity to polarize would be altered. There is evidence supporting this. HeLa cell membranes were reported to become permeabilized after 20 min of exposure to 0.17 mM Triton X-100 [204]. At 0.17 mM Triton X-100, more RBCs experienced irreversible damage from the surfactant as shown in Figure 4-4 whereby the cells lost integrity and collapsed. The increase in overall hemolysis and cell radii indirectly suggest pore formation within the RBC membranes in the presence of 0.17 mM Triton X-100. Changes in the membrane permeability have a cascading effect by not only changing the membrane polarization but also altering internal cytoplasm conductivity and permittivity. Here, since the DEP tests were completed in the β -dispersion region, the DEP responses were not able to provide insight into changes in the RBC cytoplasm.

In summary, as shown in Figure 4-5, the increased cell size and permittivity of Triton X-100 treated RBCs increased the exerted \vec{F}_{DEP} and decrease f_{CO} . This trend was also apparent in Table 4-1 showing membrane capacitance changes of 11.51, 14.05, and 13.61 mF/m² for 0.00 mM, 0.07 mM, and 0.11 mM Triton X-100 treated cells, respectively. The strong media/membrane polarization dependency in the presence of Triton X-100 suggests that interactions between cells and surfactants alter

dielectrophoretic polarizations and should be independently tested and controlled for in electrokinetic applications.

4.5 Conclusions

Surfactants are regularly added to cell-buffer solutions to reduce cell sticking to surfaces and improve reproducibility between experimental runs. However, surfactant interactions with cell membranes and influences on the cell dielectric behaviors have not previously been explored in electrokinetic systems. This work investigated the impact of Triton X-100 surfactant interactions with RBC membranes using dielectrophoresis over the β -dispersion frequency region from 300 to 700 kHz where cell polarizations are membrane-dominated. RBCs were treated with low concentrations of Triton X-100 (0.07-0.17 mM) below the critical micelle concentration; beyond the CMC, hemolysis is prevalent.

Traditional cell characterization techniques (UV-Vis spectroscopy and optical microscopy) were reproduced as comparison controls to previously reported non-electrokinetic measures of RBC integrity and viability. Increasing Triton X-100 (0.00-0.17 mM) increased the RBC cell size from 3.55 ± 0.32 to 3.94 ± 0.39 μm . Concentrations of 0.07 and 0.11 mM displayed compromised cell membrane integrity as deduced from Soret and α and β chain peaks in UV-Vis spectra.

Dielectrophoretic responses of RBCs pretreated with the same four Triton X-100 concentrations were then measured. Upon increasing Triton X-100 from 0.00 to 0.07 mM, the experimentally observed DEP spectra shifted the f_{CO} from 482 ± 10 to 370 ± 11 kHz. The f_{CO} decreased to 375 ± 10 kHz in the presence of 0.11 mM Triton X-100

and no f_{CO} was observed was observed at 0.17 mM Triton X-100 because the cells only displayed n-DEP.

A single-shell oblate model was utilized to fit parameters to experimentally measured cell velocity and DEP force data. In the presence of Triton X-100 (0.07 and 0.11 mM), cell enlargement was found to decrease the predicted f'_{CO} by $\sim 8.6\%$ while membrane permittivity increase was able to decrease f'_{CO} further by $\sim 16\%$ to match experimental data. Membrane capacitance increased from 11.51 mF/m² for native (0.00 mM) to 14.05 mF/m² for 0.07 mM Triton X-100 treated cells, respectively, while it only increased to 13.61 mF/m² for 0.11 mM Triton X-100 treated cells. It is valuable to note that the DEP force magnitude was increased by 25% across all Triton X-100 concentrations. Mechanisms for these changes are two-fold including cell enlargement as well as increasing the cell membrane permittivity. This work elucidated that surfactant molecules traditionally added to mediate microfluidic device wall properties also dynamically interact with cell membranes and alter electrokinetic responses.

Since electrokinetic microfluidic systems are gaining commercial traction for portable medical diagnostic applications, it is important that the effects of the secondary chemical interactions between cells and surfactants be further explored. This work sets a foundation for measuring these phenomena and should be separately attributed to cellular response data in order to accurately catalog cell properties and engineer reliable microfluidic electrokinetic devices.

Chapter 5: Dielectric Changes in Membrane Properties of Porcine Kidney Cells Before and After Porcine Parvovirus Infection

A comprehensive level of understanding led us to utilize dielectrophoresis in its full capacity as a tool to monitor the state and progression of virus infection as well as antiviral activities of regenerative compound. The ability to monitor the state and progression of virus infection is important for the generation and development of new antiviral drugs. Previous research illustrated osmolyte glycine capability as a natural antiviral compound to reduce porcine parvovirus (PPV) infection in porcine kidney (PK-13) cells. It was postulated that the osmolyte glycine altered the virus-host interactions through stabilizing capsid protein and preventing them from assembling into viable virus particles. However, the kinetics of membrane perturbation mechanism was poorly understood. Elucidating the membrane-related kinetics of these novel antiviral compounds are crucial to their development as potential therapeutic drugs. Frequency-dependent responses of biological cells can be used to obtain information about membrane barrier functionality and thus may help ascertain virus-host-osmolyte mechanisms. Dielectrophoresis (DEP) was utilized to characterize non-infected, PPV-infected, glycine-treated/non-infected, and glycine-treated/PPV-infected PK-13 cells. Dielectrophoretic spectra were compiled from cell velocities to determine DEP force and crossover frequency (f_{co}) for non-infected and infected cells in the presence and absence of osmolyte glycine. Data were collected while applying a $0.1 \text{ V}_{pp}/\mu\text{m}$ signal with 0.1-0.9 MHz frequencies at 0, 1.5, 4, 8, and 10 hours post infection.

5.1. Introduction

In the life and medical sciences, there is a growing demand for preventive care, early diagnosis, and high-quality treatment with less invasive and more accurate procedures. Electrokinetic microfluidic devices are a cutting-edge platform for point-of-care diagnostics and pharmaceutical tests with fundamental features and potential advantages such as low sample consumption, low-cost, short response, and quantification times, and low labor demands [1, 207, 208].

Electrokinetic microfluidic platforms enable cell manipulation, characterization, separation, and concentration [209-211]. One versatile electrokinetic technique is dielectrophoresis (DEP), which can induce directional motion of cells within spatially non-uniform electric fields [22, 66, 210]. DEP responses are directly dependent on ion mechanisms leading to charge buildup and cell polarizability within electric fields [212]. Dielectrophoresis-based microfluidic devices allow (sub)cellular characterization based on the dielectric properties of the cell. The dielectric properties that can be monitored via DEP technique include changes of cell morphology, membrane surface area arising (e.g. the appearance of microvilli or blebs), membrane conductivity associated with a membrane structural degradation, and cytoplasm conductivity associated with ions leakage. All these features contribute to the frequency spectrum of the cell's dielectrophoretic behavior, which can be exclusively characteristic of a particular cell [32, 173].

The cell's dielectrophoretic behavior has been proven to carry a verity of useful information about cell pathological status [13-15, 31, 69, 148, 156, 213-218]. The cell's

transition from a healthy to a diseased state is often associated with changes in the dielectric properties of the cell. Extensive studies have shown that healthy [148, 156], drug-treated [213], parasite-infected [31, 218], virus-infected [13-15], cancerous [69, 214, 215], and bacteria cell exhibit characteristic DEP signatures associated with dielectric properties of the cells [216, 217]. According to the World Health Organization (WHO), viral diseases are listed among the top ten essential in vitro diagnostic initiatives [164]. As the viral disease progress, there are certain complex changes that occur in the cell membrane which can be used as a disease electrophysiological marker to diagnose disease, track disease progression, and help vet more tailored treatment strategies [13-15]. Although considerable effort has been expended on studying virus-host interaction through pathological observation and DEP techniques [219], much less is known about the kinetics of membrane perturbation mechanism during the infection cycle. Thus, tools such as DEP are needed in this field to better understand membrane-related kinetic mechanisms without requiring invasive and expensive cell dissections. The ability to utilize dielectrophoretic does not limit to disease diagnostic. Dielectrophoresis-based microfluidic devices have been utilized to screen for new drug candidates in a high-throughput manner [213].

Recently, there is a growing interest in leveraging natural compounds for therapeutics; since viruses are starting to show resistivity to current drugs [219]. Osmolytes have been studied as potential natural antiviral compounds. Osmolytes are small organic compounds that are found in the cells of many organisms with the ability to stabilize intracellular proteins against environmental stress, such as extreme temperature

or high osmotic pressure [220]. Betaine, sucrose, alanine, trehalose, glycine, and trimethylamine N-oxide (TMAO) osmolytes were utilized against the non-enveloped porcine parvovirus (PPV) with glycine and TMAO demonstrating the greatest antiviral activity [219]. PPV is responsible for pig intestine infections, which is the most frequent cause of swine reproductive failure [221]. This virus is also often used as a model for the human B19 parvovirus, which is associated with a number of conditions, such as the fifth disease in children and arthritis and arthralgias in adults [222]. This study focused on the osmolyte glycine impact on membrane-related kinetics of PPV.

Studying mechanistic origin of disease during the virus infection cycle can help to elucidate the membrane-related kinetics of PPV. The PPV infection cycle has been pieced together from traditional pathological observation techniques. Briefly, upon infection, viruses bind to specific target receptors on the cell membrane surface where the parvovirus capsid is internalized through clathrin-coated pits and then transferred through the endocytic path. Then, the capsid is uncoated, and the genome is released and translocated to the nucleus for genome replication and transcription and protein expression. The viral DNA becomes replicated; the expressed genes enable progeny viral genomes to form newly assembled capsids within the nucleus. Post-capsid assembly and genome packaging, newly formed virions must exit the nucleus and traffic to the cell surface for another round of infection [221, 223]. Here, we hypothesize that cell's transition or disruption from a healthy to a diseased state changes cell membrane polarization and permittivity, which can be discerned from measured DEP spectra.

5.2. Dielectrophoresis Theory and Background

Dielectrophoresis employs AC signals to manipulate particles or cells toward high or low electric field regions within a medium. The dielectrophoretic force, \vec{F}_{DEP} , on a homogenous spherical particle (a rough first approximation to a cell), can be described by a geometry term, a frequency-dependent dielectric term, and a non-linear electric field term as follows [111]:

$$\vec{F}_{DEP} = 4\pi r^3 \epsilon_m \text{Re} [f_{CM}] \nabla \vec{E}_{rms}^2 \quad (5-1)$$

where r is the outer particle (or cell) radius, $\text{Re} [f_{CM}]$ is the real part of the Clausius–Mossotti factor, and $\nabla \vec{E}_{rms}^2$ is the electric field gradient squared. Within non-uniform electric fields, particle motion can be described by the f_{CM} [224-226]:

$$f_{CM} = \frac{\epsilon_p^* - \epsilon_m^*}{\epsilon_p^* + 2\epsilon_m^*} \quad (5-2)$$

$$\epsilon_i^* = \epsilon_i + \frac{\sigma_i}{j\omega} \quad (5-3)$$

where ϵ_i^* is the complex permittivity, ϵ_i is the permittivity, σ_i is the conductivity, and the subscript i represents either the particle ($i = p$) or the medium ($i = m$). The complex permittivity, ϵ_i^* , is also dependent upon the angular frequency (ω) with j representing the imaginary number ($j = \sqrt{-1}$) [224]. In equation (5-2), if the f_{CM} is positive, the particles move up electric field gradients. This behavior is recognized as positive DEP (p-DEP), indicating that the particles are more polarizable than the suspending medium $\epsilon_p^* > \epsilon_m^*$ [224]. If the f_{CM} is negative, the particles move down electric field gradients. This is known as negative DEP (n-DEP), reflecting lower cell polarizability than the suspending medium $\epsilon_p^* < \epsilon_m^*$ [224]. In the case where the f_{CM} is zero, the particle is not polarized.

The frequency at which cells transition from experiencing n-DEP to p-DEP or p-DEP to n-DEP is called the crossover frequency (f_{CO}) and manifests in experiments as little or no motion in the electric field [226].

The f_{CM} used in the DEP force expression equation (5-1) is fairly accurate in describing homogeneous spherical particles; however, biological cells have a more complex heterogeneous structure [181]. Thus, deviation from a homogeneity will reduce equation (5-1) accuracy. The cell polarization response can be modeled using a series of equations where cell's complexity can be added to the DEP model by introducing structural layers (i.e. cell membrane and cytoplasm). Here, the porcine kidney (PK-13) is our focus. When in suspension, PK-13 cells are spherical in shape. Thus, PK-14 cells can be approximated to a conductive cytoplasm bounded by an insulator-like cell membrane. The following section will focus on the single-shell spherical DEP polarization model.

5.2.1 Single-Shell Spherical DEP Polarization Model

Equation (5-2) can be modified for the single-shell spherical DEP polarization model by incorporating the intrinsic effects of a shell (i.e. the cell membrane) and core (i.e. the cytoplasm). For a sphere the effective complex dielectric permittivity ϵ_c^* as a function of cell components is [224, 226]:

$$\epsilon_c^* = \epsilon_{mem}^* \frac{\left(\frac{r}{r-d}\right)^3 + 2\left(\frac{\epsilon_{cyto}^* - \epsilon_{mem}^*}{\epsilon_{cyto}^* + 2\epsilon_{mem}^*}\right)}{\left(\frac{r}{r-d}\right)^3 - \left(\frac{\epsilon_{cyto}^* - \epsilon_{mem}^*}{\epsilon_{cyto}^* + 2\epsilon_{mem}^*}\right)} \quad (5-4)$$

where d is the cell membrane thickness, ϵ_{mem}^* is the membrane complex permittivity, and ϵ_{cyto}^* is the cytoplasm complex permittivity. In the presence of electric fields, the cell

exhibits frequency dependent dielectric dispersions which can be characterized by the α - (sub-Hz to kHz), β - (kHz to MHz), and γ - (MHz to GHz) dispersion. Dielectric dispersions originate from the electrical polarization at different length-scales of the cellular system [227]. This can be used to track changes in the cell's dielectric properties as a function of frequency. Here, we explore 0.1 to 0.9 MHz in the β -dispersion region. Maxwell-Wagner interfacial polarizations govern cell responses at the β -dispersion region. Here, the cell's dielectric dispersion is influenced by the interfacial polarization between an insulator-like cell membrane and the medium. A wide range of information can be obtained about a cell population with intact membranes or compromised membranes at radio frequencies regions (kHz to MHz) [23, 66]. This allows researchers to deduce characteristics of cell damage, apoptosis, necrosis, and drug-induced cell protection or demise from DEP spectra [66, 228].

Our team has optimized frequency sweeps as a tool to generate near continuous DEP spectra, greatly reducing the number of experiments necessary and increasing DEP spectral resolvability [229, 230]. DEP experiments are conducted while visually monitoring the cell's motion as a function of frequency in the non-uniform electric fields. The charge distribution on membrane surfaces due to polarization changes as the frequency sweeps from high to low values enabling near real-time tracking of interfacial charge relaxation shifts. Quantification of motion determines DEP dispersion maxima and minima and crossover frequency (f_{co}), basically the key components of the DEP spectra.

5.2.2. Quantifying DEP Force Spectra on Bioparticles by Velocity Tracking Measurements

In case that the shape and radius of the cell are known, the DEP force spectra can be determined by measuring the cell/particle velocity (\vec{v}) [231]. If Brownian motion and the buoyancy force are neglected, the net DEP force is the sum of the Stokes drag force (\vec{F}_D) and the acceleration force (\vec{F}_A): $\vec{F}_{DEP} = \vec{F}_D + \vec{F}_A$. For spheroidal cell the Stokes drag force is [232]:

$$\vec{F}_{DEP} = m\vec{a} + 6\pi\eta r\vec{v} \quad (5-5)$$

where \vec{a} is acceleration and η is the fluid's dynamic viscosity. One of the key elements of a DEP spectra is crossover frequency (f_{CO}). The f_{CO} is an easily discernable point from experiments since cell's transition from n-DEP to p-DEP or p-DEP to n-DEP can be visualized using 2D microscope. This zero-polarization state can be calculated by setting $\text{Re}[f_{CM}]$ equal to zero in equation (5-4) and rearranging [66, 123]:

$$f_{CO} = \frac{1}{\sqrt{2}} \frac{\sigma_m}{\pi r C_{mem}} \sqrt{1 - \frac{r G_{mem}}{2\sigma_m} - 2 \left[\frac{r G_{mem}}{\sigma_m} \right]^2} \quad (5-6)$$

where C_{mem} and G_{mem} are the cell membrane capacitance and conductance, respectively and are given by:

$$C_{mem} = \frac{\epsilon_{mem}}{d} \quad (5-7-a)$$

$$C_{mem} = \frac{\sigma_{mem}}{d} \quad (5-7-b)$$

As the DEP force changes polarity, the cell's dielectric properties (i.e. cell membrane capacitance and conductance) can be estimated using crossover frequency (f_{CO}) along with other data points from the DEP spectra. The membrane capacitance term

reflects how strongly the membrane acts as a charge barrier and is a function of membrane area, thickness, composition/dielectric properties, and morphological complexity. Membrane conductance reflects the net transport of ionic species across the membrane through pores, ion channels, and defects under the influence of an applied field. In equation (5-6), the medium dielectric properties are known and can be controlled. Once the f_{CO} is determined experimentally, the membrane capacitance and conductance can be calculated. Each cell has a unique dielectrophoretic spectrum as a function of frequency that reflects the molecular structure and dielectric properties of both the cell's surface and internal structure. The practical applications of observing f_{CO} include being able to determine the dielectric properties of the cell resulting from cell damage, apoptosis, necrosis, and drug-induced cell protection or demise.

This work utilized dielectrophoresis-based microfluidics as a label-free platform to characterize non-infected, PPV-infected, glycine-treated/non-infected, and glycine-treated/PPV-infected PK-13 cells. Dielectrophoretic spectra were compiled from cell trajectories and velocity within a microfluidic device to determine DEP force and crossover frequency (f_{CO}). Data was collected while applying a $0.1 \text{ V}_{pp}/\mu\text{m}$ signal with 0.1-0.9 MHz frequencies at 0, 1.5, 4, 8, and 10 hours post infection in the absence and presence of glycine.

5.3. Materials and Methods

5.3.1. Chemicals and Preparation

Porcine parvovirus (PPV) was a generous gift from Dr. Ruben Carbonell, North Carolina State University. Potassium phosphate monobasic (ACS, $\geq 99\%$), and potassium

phosphate dibasic (ACS, $\geq 99\%$) were purchased from EMD Millipore (Billerica, MA, USA). Sodium chloride ($>99\%$, ACS) was purchased from Macron Chemicals (Center Valley, PA, USA). Dextrose ($P \geq 99.5\%$) were purchased from Sigma-Aldrich (St. Louis, MO, USA).

All DEP experiments were conducted in controlled isotonic phosphate buffer saline (PBS) solution with a conductivity of 0.1 S/m. To prepare PBS solution, 2.6 mM potassium phosphate monobasic, 2.6 mM 201 potassium phosphate dibasic, 2.6 mM sodium chloride, and 274.3 mM dextrose were mixed in 24.9 mL E-pure water ($18.2 \Omega \cdot \text{cm}$, EMD Millipore Simplicity Ultrapure 185, Billerica, MA, USA) stored at 4°C and used within one week.

5.3.2. Cell Culture, Virus Infection, and Osmolyte Treatment

PK-13 cells were grown in minimum essential medium (MEM). MEM is supplemented with 10% fetal bovine serum (FBS) and 1% penicillin/streptomycin. Multiple flasks of PK-13 cells were cultured for DEP tests including non-infected (control), PPV-infected, glycine-treated/non-infected (glycine control), and glycine-treated/PPV-infected flasks. PK-13 cells were seeded into tissue culture flasks with a concentration of 9×10^5 cells per flask. Cells were then incubated at 37°C , 5% CO_2 , and 100% humidity for 48 hours to obtain 70% confluence. After 48 hours, the culture medium was removed from the flasks. To prepare non-infected (control) flasks, the culture medium was replaced by 1 mL of fresh culture medium and then the flasks were rocked for 1 hour on a table. To prepare PPV-infected flasks, 1 mL of Log 7 PPV was added to each flask and then the flasks were rocked for 1 hour on a table to ensure

immediate cell infection. After one hour, 9 mL culture medium was added to both non-infected (control) and PPV-infected flasks then the flasks were incubated at 37°C, 5% CO₂, and 100% humidity. For osmolyte treatment, glycine was prepared as a stock solution of 0.20 M in the culture medium. Next, 10 mL of 0.20 M glycine was introduced the non-infected and PPV-infected flasks. To investigate the impact of glycine on the PK-13 cells, the glycine control experiments were conducted at 0, 1.5, 4, 8, and 10 hours.

5.3.3. Microfluidics Design and Fabrication

A star-shaped electrode design was used to study non-infected and PPV-infected PK-13 cells before and after glycine treatment. As shown in Figure 5-1-a, the star-shaped electrode design had four pairs of triangular electrodes converging symmetrically at a center point. The shortest and longest distance between the electrodes are 50 µm and 125 µm, respectively. Photolithography, sputtering, and lift-off were employed to fabricate the microelectrodes on glass microscope slides following previously detailed procedures [16, 17]. The star-shaped electrodes were fabricated with a thickness of 95 nm of Pt above 10 nm Cr plated onto 25×76×1mm glass microscope slide ([AmScope.com](http://www.AmScope.com)). Photolithography was utilized to create a master wafer from which polydimethylsiloxane (PDMS) castings were obtained. Electrodes were then overlaid by a PDMS circular microfluidic chamber. The circular microfluidic chamber had a diameter and depth of 590 µm and ~70 µm, respectively. Disposable biopsy punches (Robbins Instruments, Chatham, NJ, USA) were utilized to create inlet and outlet ports of 300 µm in diameters.

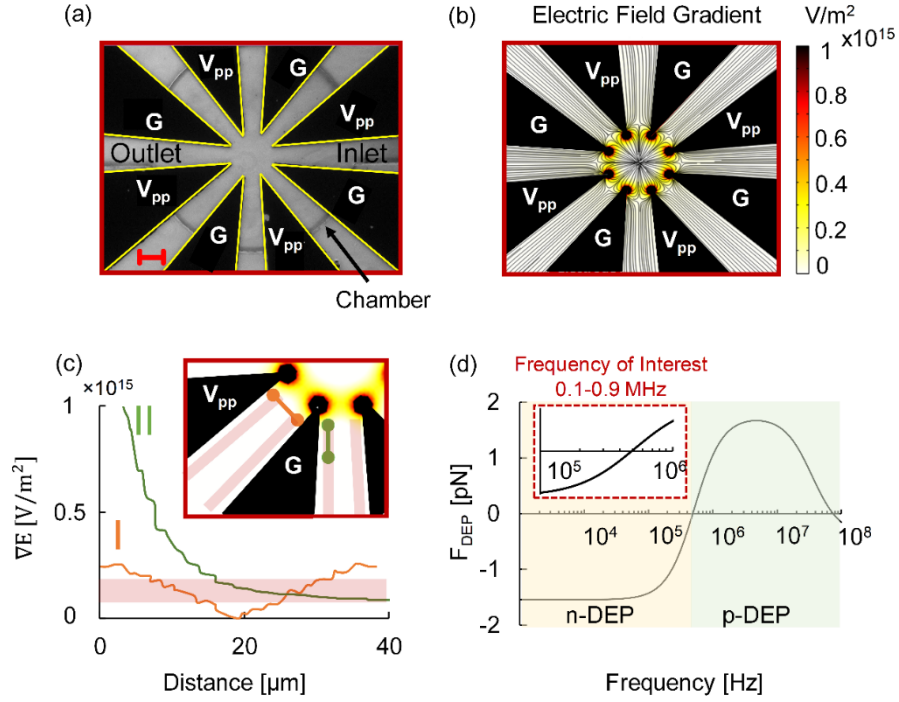


Figure 5-1: Microfluidic device configuration with a PDMS fluidic layer. (a) The microscale image of the electrodes overlaid by a circular microfluidic chamber. The circular microfluidic chamber has a diameter of 590 μm . The red scale bar is 50 μm . (b) The electric field gradient (V/m^2) was simulated using COMSOL Multiphysics® simulations in 0.1 S/m medium at 0.1 $V_{pp}/\mu\text{m}$. (c) Plotted cutline of the electric field gradient parallel to electrodes is shown in green, while the electric field gradient perpendicular to the working and ground electrode is shown in orange. (d) The single-shell spherical DEP model for a Pk-13 predicts a low 0.45 MHz crossover frequency in 0.1 S/m medium.

5.3.4. DEP Solution Preparation and Experiments

The culture medium was removed from the flasks. Next, 3 mL of PBS was added and removed from the flasks to adjust the pH to 7.2. To detach PK-13 cell, 3 mL of trypsin was added to each flask. The flasks were incubated at 37°C, 5% CO_2 , and 100% humidity for 10 minutes. To inactivate the trypsin, 3 mL of culture medium was added. The PK-13 suspension was transferred to sterile tubes and centrifuged for 3 minutes at 415 rcf in a Sorvall ST16R centrifuge (Thermo Scientific, Pittsburgh, PA). The

supernatant was then removed, and PK-13 cells were resuspended in 500 μL of DEP suspension medium with the conductivity 0.1 S/m.

Samples were introduced via inlet port into the microfluidic chamber. The dielectrophoretic microfluidic device was mounted on a Zeiss Axiovert microscope (Zeiss, Oberkochen, Germany). An AC potential was applied via a custom-built function generator (MicroDevice Engineering Inc., Houghton, MI, USA). Experiments were conducted at 5 V_{pp} (electric field density = $0.1 V_{pp}/\mu\text{m}$) with decreasing frequency from 0.9 to 0.1 MHz at a rate of 2400 Hz/s. The electric field density was measured from the externally applied potential over the shortest gap between the electrodes (50 μm). Cell movement was recorded via 10X magnification video microscopy at 1 fpm for 343 seconds.

5.3.5. Cell Viability Assessment

The viability of the PK-13 population was determined by trypan blue dye. Trypan blue is negatively charged dye. Trypan blue does not interact with cells unless the cell membrane is damaged. Briefly, 0.4% trypan blue stock solution was prepared in phosphate buffered saline solution. Next, 0.1 mL of trypan blue stock solution was added to 0.1 mL of non-infected and PPV-infected PK-13 cell before and after glycine treatment at $t = 0, 1.5, 4, 8,$ and 10 hours. A drop of the trypan blue stained cells was placed in the middle of a clean glass microscope slide. To spread a sample, a coverslip was placed gently over the drop without applying pressure. Images of the cells were taken with an Olympus IX51 microscope with a DP72 camera (Olympus, Center Valley, PA, USA).

5.3.6. Cell Selection and Data Acquisition

As shown in Figure 5-1, the electric field in the star-shaped device is non-uniform. COMSOL Multiphysics® (Burlington, MA, USA) simulation software was utilized to demonstrate the non-uniform electric field gradient in star-shaped shape electrode designs. The *Electric Potential* boundaries were *Ground* and 5 V_{pp} for Pt ground and working electrodes, respectively. Outer boundaries were set to *Electrical Insulation*. The electric field gradients were accomplished by solving Laplace's equation using the Lagrange element method. This electric field non-uniformity induces motion in polarizable cells. Cells located in black, red, and dark orange regions in Figure 5-1-b experience a greater DEP force than cells in light orange, yellow, and white regions. Thus, cells were selected within regions where equal force was exerted on the cells. Thus, comparisons only reflect cell properties and not spatial field properties. Cells were selected that fell within the similar electric field gradient shown in Figure 5-1-c then tracked to accurately and reproducibly quantify displacement to determine cell velocity and subsequently DEP response. Non-infected (control), PPV-infected, glycine-treated/non-infected (glycine control), and glycine-treated/PPV-infected PK-13 cell DEP behaviors were quantified with Tracker 4.11.0 software (<https://physlets.org/tracker/>) to calculate the cell velocity. Then, using equation (5-5) the dielectrophoretic force (\vec{F}_{DEP}) was calculated and plotted. Cell size was obtained by capturing 2D microscopy images of 50 cells per experiment and measuring the cell diameter using ImageJ®. Statistical analysis was conducted whereby * represents p-values <0.05. P-values <0.05 was considered statistically significantly different.

Cell's dielectrophoretic responses, R_c , were analyzed before and after glycine treatment at 0, 1.5, 4, 8, and 10 hours. Here, the cell's dielectrophoretic responses are categorized into three subpopulation groups: n-DEP, p-DEP, p- to n-DEP. R_c (%) was calculated by dividing the number of cells in each group, n_i , exhibiting n-DEP or p-DEP (where i = n-DEP, p-DEP, p- to n-DEP) by the total number of cells, n_T :

$$R_c(\%) = \frac{n_i}{n_T} \times 100 \quad (5-8)$$

Cell's optical contrast can be correlated with the cell's transition from the healthy to dead cells. Video frames were analyzed with ImageJ® software (NIH, <https://imagej.nih.gov/ij/>) to measure the cell-based intensity of each frame. Briefly, the intensity density of each cell, I , was normalized with respect to the maximum intensity density of the cell population, I_m . Histogram graphs were utilized to plot the cell's dielectrophoretic response (R_c) versus the normalized intensity density \bar{I} .

$$\bar{I} = \frac{I}{I_m} \quad (5-9)$$

5.4. Results and Discussion

This study examined the state and progression over time of PPV viral infection of PK-13 cells as well as implications of an antiviral compound glycine using cell property techniques including optical microscopy, intensity analysis, trypan blue stain test, and dielectrophoresis. Membrane dielectric properties were calculated to elucidate the membrane-related kinetic mechanism during the viral infection in the absence and presence of the osmolyte glycine.

5.4.1. Qualitative Dielectrophoretic Behavior

To establish DEP response spectra, frequency sweeping measurements were explored from 0.1 to 0.9 MHz at $0.1 \text{ V}_{pp}/\mu\text{m}$. The frequency sweep was conducted from high to low frequency because the forces cells experience while undergoing p-DEP at higher frequencies are larger in magnitude than those forces cells experience when trapped at electric field minima while experiencing n-DEP. Experiments were performed ($n > 9$) over 10 hours of observation at 0, 1.5, 4, 8, and 10 hours. Figure 5-2 shows images extracted from the video of PK-13 cell DEP responses with the electric field off and at 0.8, 0.3, and 0.1 MHz (columns); field strength was fixed to $0.1 \text{ V}_{pp}/\mu\text{m}$ in 0.1 S/m PBS solution. Prior to applying the potential, non-infected PK-13 cells (control) were uniformly distributed in the chamber. After applying the signal, the majority of the non-infected Pk-13 cell population were pushed toward the high electric field density regions, indicating p-DEP. The non-infected PK-13 cells exhibited mainly p-DEP from 0.9 MHz down to $\sim 0.48\text{-}0.46$ MHz. The cells then experienced a directional shift in force through the crossover frequency, f_{CO} , to then push the PK-13 cells towards the electric field minima between the electrodes and the chamber center. In the second row of Figure 5-2, the PPV-infected PK-13 cells also first experience p-DEP, but then crossover to n-DEP behavior below ~ 0.3 MHz. Glycine-treated/non-infected PK-13 cells (glycine control, third row) showed behavior similar to non-infected PK-13 cells (control, first row). For glycine-treated/PPV-infected cells shown in the fourth row, a lethargic transition to n-DEP was first observed below ~ 0.3 MHz. The DEP time-dependent videos revealed

significant changes in crossover frequency and cells' dielectric properties by 10 hours after the treatment.

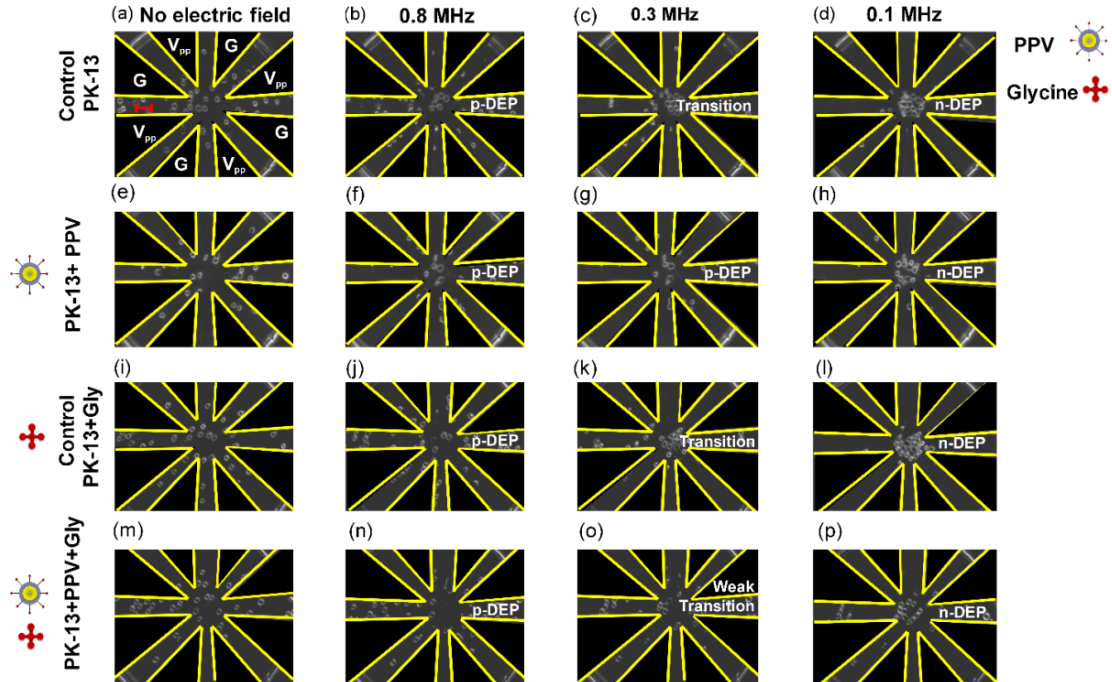


Figure 5-2: Time sequence of PK-13 cells in 0.1 S/m isotonic phosphate buffer saline at 0.1 $V_{pp}/\mu m$ with frequencies from 0.9 MHz to 0.1 MHz. All cell populations are 10 hours after infection and/or glycine addition. Images are shown at 0 sec and no electric field (a, e, i, and m), 42 sec corresponding to 0.8 MHz (b, f, j, and n), 250 sec corresponding to 0.3 MHz (c, g, k, and o), and 334 sec corresponding to 0.1 MHz (d, h, l, and p). Positive DEP and negative DEP are noted along with the directional transition.

5.4.2. Cell Population Analysis

Here, the dielectrophoretic behavior of the whole cell population is divided into three subpopulation groups: n-DEP, p- to n-DEP, and p-DEP. The three subpopulation groups maintained their individual dielectric properties throughout the whole Maxwell-Wagner interfacial polarizations shift. The changes in bulk dielectric properties of the cells might be better modeled as shifts in cells between different dielectric

subpopulations, rather than assuming a homogeneous dielectric population. Figure 5-3-a and c illustrate the stacked column representation of cell's dielectrophoretic responses, R_c (%), for PPV-infected/PK-13 cells before and after glycine treatment. Cells that exhibit n-DEP over the whole frequency range were grouped as n-DEP (yellow color in Figure 5-3). The cell group with both p-DEP and n-DEP responses were clearly observable and classified as p- to n-DEP (grey color in Figure 5-3). Finally, blue is used to identify cells only showing p-DEP. Upon applying the potential, most of the cell population ($\sim 80\%$, grey and blue) experienced p-DEP. These cells showed brighter intensity than the background with well-defined rounded structures. Some cells ($\sim 20\%$, yellow areas) were pushed toward the low electric field density region between the electrodes at the chamber center, showing n-DEP. These cells were not as bright as the grey and blue groups and some contained visibly deformed membranes.

Normalized intensity density analysis, \bar{I} , was utilized to quantify cellular brightness within each subpopulation. Normalized intensity density, \bar{I} , ranged from 0.2 as the lowest intensity with the darkest cell contrast to 1 as the highest intensity with the brightest cell contrast. Figure 5-3-b inset shows the optical images of representative PK-13 cells from the darkest ($\bar{I}=0.2$) to the brightest ($\bar{I}=1$) contrast within one experimental run. Figure 5-3-b and d show the histogram plot of cell dielectrophoretic responses, R_c (%), versus normalized intensity density, \bar{I} , for PPV-infected PK-13 cells before and after glycine treatment at 0 and 4 hours. There were significant differences between the subpopulation showing n-DEP over the frequency range of interest and the other two subpopulation groups, p- to n-DEP and p-DEP. The results suggest that the n-DEP subpopulation

exhibits $\bar{I} \leq 0.7$ while sub-populations of p- to n-DEP and p-DEP have $\bar{I} \geq 0.7$. No significant differences were observed between p- to n-DEP, and p-DEP groups. Thus, to compile DEP spectra, only individual cells experiencing both p-DEP and n-DEP were screened over the frequency range of interest.

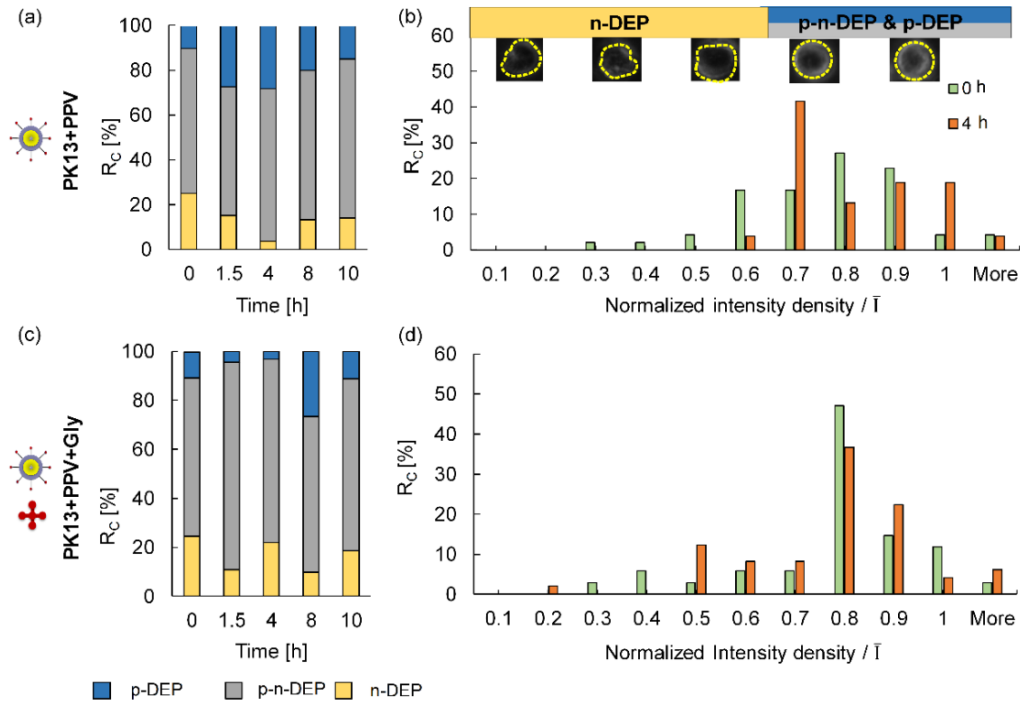


Figure 5-3: Cell's dielectrophoretic response, R_c (%) stacked into a column chart for PPV-infected PK-13 cells (a) before and (c) after glycine treatment. Cells that exhibit n-DEP over the whole frequency range were grouped as n-DEP (yellow color) while cells show p-DEP group (blue color). The notation p-n DEP indicates cells that initially exhibit p-DEP and then transit to n-DEP (grey color). The histogram plot of cell's dielectrophoretic response (R_c) versus normalized intensity density for PPV-infected PK-13 cells before (b) and (d) after glycine treatment at 0 and 4 hours.

5.4.3. Cell Viability Assessment

To discriminate cells' subpopulation independent of the DEP measurements, membrane viability of the cells was monitored by their ability to exclude trypan blue dye. PK-13 cells were treated with trypan blue before and after glycine treatment for both the

non-infected PK-13 and PPV-infected PK-13 cells at incubation time points $t = 0, 1.5, 4, 8,$ and 10 hours. Figure 5-4 shows color-scale images for the non-infected (control) and PPV-infected PK-13 at $t=10$ hours.

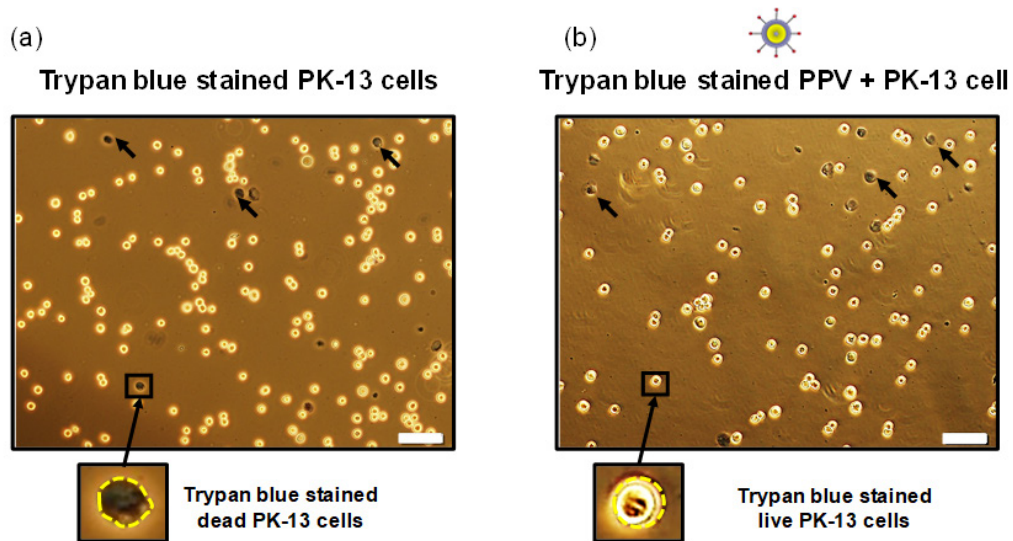


Figure 5-4: Trypan blue staining in PK-13 cells (a) before and (b) after PPV infection at $t=10$ hours. Cells including trypan blue (dead cells) are stained in blue and marked with arrows. The dark blue cells delineated with black arrows represent dead cells while the bright centered cells are considered live. White scale bar is 20 μm .

A break in the integrity of the plasma membrane immediately compromises the fundamental structure of the membrane as a barrier, and this can kill the affected cell. Generally, two main processes leading to cell death are necrosis and apoptosis. Necrosis is the premature death of a cell which initiated by cell trauma where the cell membrane loses its membrane integrity and swells leading to cell lysis. Apoptosis, also known as programmed cell death, is a biochemically regulated process. Blebs appear on the cell membrane while shrinking, leading to cell fragmentation. Previous research has documented that parvovirus infection usually induces apoptosis. Apoptotic cells at the early stages of the infection cycle exclude trypan blue, whereas late apoptosis or necrotic

cells are quickly stained with trypan blue due to their extensive membrane damage. Zhang et al showed that PPV infection induces apoptosis in PK-15 cells through activation of p53 via a mitochondria-mediated pathway [233]. Without osmolyte glycine addition, the infectious virus began to appear extracellularly after 15 hours and intracellularly after 10 hours [219]. Here in this study the earlier stages of the infection cycle (the first 10 hours) was studied.

The dark blue cells delineated with black arrows represent dead trypan blue positive cells which presumably represent the end-stage of apoptotic cell death or necrotic cells while the bright centered cells are considered live. As shown in Figure 5-4, the bright centered cells have well-defined rounded structures while the dark blue cells visibly have deformed membranes. The trypan blue assay showed high estimates of the viable cell with well-defined rounded structure during early infection cycle. Here, changes in viability of a small portion of the cell population are due to cell physiology [234], chemical abnormalities [108], medium pH and tonicity [235], mechanical forces [236], and rapid temperature changes [237]. Also, to compare color-scale and grayscale images were acquired from the same sample solution with both Olympus and Zeiss microscopes to compare color-scale and grayscale images, respectively. The results show that dark blue cells in color-scale images are the ones with the darkest cell contrast in grayscale images that exhibit n-DEP over the whole frequency range [data not shown].

5.4.4. Quantitative Dielectrophoretic Spectra

Velocities were measured from videos of PK-13 cell DEP responses to frequency sweeps from 0.9 MHz to 0.1 MHz [229, 238]. Cell velocities were compiled, converted

to force via equation (5-5) and then used to assemble PK-13 DEP response spectra. Time-dependent changes in the DEP response spectra of PK-13 cells were tracked after infection for both untreated and glycine-treated PK-13 cell populations at incubation time points $t = 0, 1.5, 4, 8,$ and 10 hours. DEP forces were compiled only for cells experiencing both p-DEP and n-DEP (Figure 5-5).

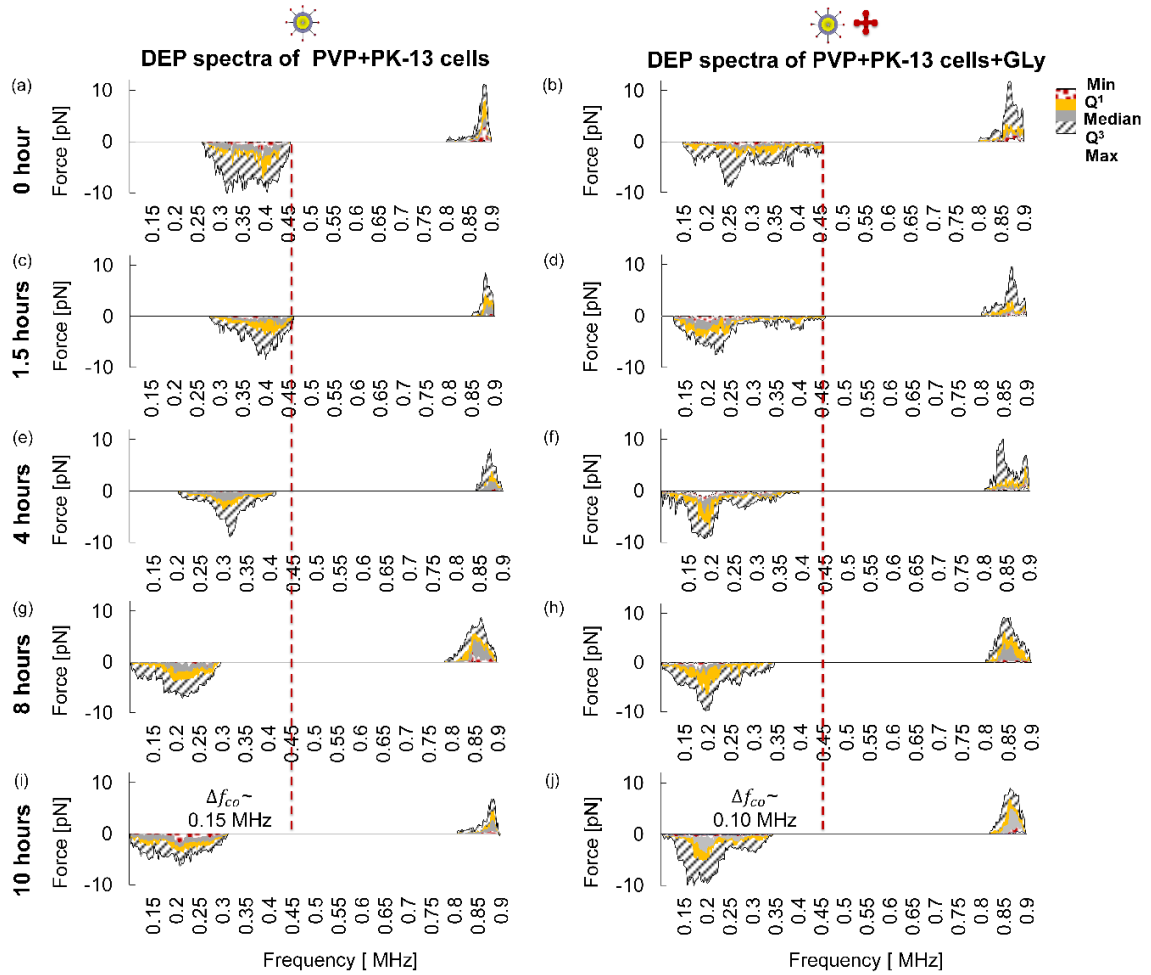


Figure 5-5: Dielectrophoretic force spectra of untreated (first column) and glycine-treated (second column) PK-13 cells post infection as function of frequency 0.9 to 0.1 MHz after (a and b) 0, (c and d) 1.5, (e and f) 4, (g and h) 8, and (i and j) 10 hours. DEP force profile inferred from the cell velocities of PK-13 samples via a box-and-whisker-inspired representation. Grey and yellow

colored regions show the first, second (aka median), and third interquartile ranges, while the min and max lines for the whiskers show the full force range (patterned area) at all cells in test region.

The Figure 5-5 uses a continuous box-and-whisker-plot representation whereby the grey and yellow colored regions show the first, second (aka median), and third interquartile ranges, while the black solid lines for the whiskers show the full force range (patterned area). This representation is a concise tool to illustrate the motion of every cell in the chamber's field of view. Each frequency's data represents 14 to 22 individual cells.

Insignificant differences were observed between the DEP spectra of non-infected PK-13 (control) and glycine-treated/non-infected PK-13 (glycine control) cells over 0, 1.5, 4, 8, and 10 hours. Non-infected PK-13 cell and glycine-treated/non-infected PK-13 cell populations consistently yielded f_{CO} of 0.45 ± 0.02 MHz and 0.44 ± 0.01 MHz, respectively (data included in supplemental information). Upon PPV infection, the DEP spectra including the f_{CO} remained unchanged for the first 1.5 hours. After 4 hours, the infected cell's f_{CO} decrease from 0.45 ± 0.02 MHz to 0.38 ± 0.02 MHz. Previous studies showed that the DNA virus capsid and then the newly formed infectious virus were discernable intracellularly after 8 and 10 hours, respectively [219, 221]. However, the DEP spectra shifted after 4 hours as shown in Figure 5-5, which suggests that the earlier stages of infection were discernable via dielectrophoretic responses including virus binding to the cell membrane and traveling into the cell [219, 221]. At 8 and 10 hours, the infected PK-13 DEP spectra then shifted lower yielding f_{CO} of 0.26 ± 0.02 MHz and 0.27 ± 0.01 MHz, respectively.

Glycine control spectrum for PK-13 cells yielded stable f_{CO} at 0.44 ± 0.01 MHz over the full 10 hours. For glycine-treated/PPV-infected cells, the DEP spectrum was similar

to that of PPV-infected cells for the first 4 hours suggesting glycine did not impede virus penetration into the cell. However, after 8 and 10 hours, the glycine-treated/PPV-infected cells displayed attenuated f_{CO} shifts only down to 0.33 ± 0.02 MHz at both 8 and 10 hours. This suggests that glycine improvements occur post cell infection, but since the virus still penetrates the cell, DEP spectral shifts are still observed compared to the control.

5.4.5. Cell Membrane Capacitance

The cell's transition from a healthy to a diseased state is often associated with changes in the dielectric properties of the cell (i.e. membrane capacitance). Membrane capacitance can be used as a disease electrophysiological marker to diagnose disease, track disease progression, and help vet more tailored treatment strategies. As shown in equation (5-6), the membrane capacitance is a function of medium conductivity (σ_m), crossover frequency (f_{CO}), and cell radii (r). Medium conductivity, σ_m , strongly effects the cell behavior in the β -dispersion region. In our DEP model, σ_m is kept constant at 0.1 S/m to fit the experimental conditions. As shown previously (Figure 5-5), the crossover frequency was determined experimentally and quantified from the cell velocities and would not be discussed in depth here. Thus, to accurately calculate membrane capacitance the impact of cell radius was also studied.

Maxwell-Wagner interfacial polarizations govern cell responses in the β -dispersion region whereby the electric field interacts with ions in the medium causing them to move and align around the cell. Cell size is critical to interfacial polarization; the larger the cell is the longer the characteristic time is for ions to move around, align, and induce

membrane polarization and thus cell movement. Equations (5-1) and (5-6) explain how cell radius impacts DEP force magnitude and f_{CO} , respectively. Figure 5-6-a and c are the box-and-whiskers-plots of cell radii for non-infected (controls) and PPV-infected PK-13 cells before and after glycine treatment at $t = 0, 1.5, 4, 8$, and 10 hours. The box-and-whiskers-plots illustrate the distribution of data based on the median, first quartile (grey), third quartile (yellow), and minimum and maximum values. The mean and standard deviation were utilized to develop a statistical measure of cell radius.

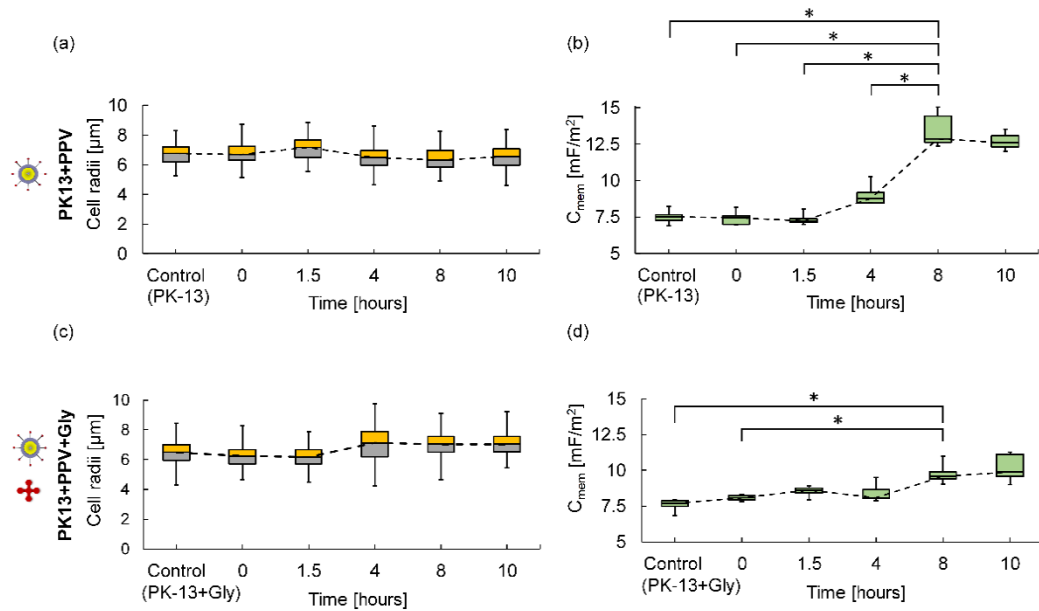


Figure 5-6: The box-and-whiskers-plots of cell radii for non-infected (controls) and PPV-infected (a) before and (c) after glycine treatment. Cell radius of PPV-infected and glycine treated/PPV-infected are shown at $t = 0, 1.5, 4, 8$, and 10 hours. The box-and-whiskers-plots illustrate the distribution of data based on the median, first quartile (grey), third quartile (yellow), and minimum and maximum values. The box-and-whiskers-plots of cell membrane capacitance of non-infected (controls) and PPV-infected (b) before and (d) after glycine treatment. The first quartile and third quartile are shown in green color.

The cell radius of non-infected PK-13 cells (control) was $6.67 \pm 0.70 \mu\text{m}$. Upon infection, the cell radius was 6.76 ± 0.73 and $6.54 \pm 0.75 \mu\text{m}$ at 0 and 10 hours,

respectively. The observed difference in cell radii is not statistically significant. In the presence of glycine, the cell radius of non-infected PK-13 cells (glycine control) was $6.45 \pm 0.83 \mu\text{m}$. The radius of glycine-treated/PPV-infected cell was 6.22 ± 0.81 and $7.12 \pm 0.88 \mu\text{m}$ at 0 and 10 hours, respectively. The radius of glycine-treated/PPV-infected cell was minimally statistically different ($p\text{-value}=0.86$). The observed slight increase in cell diameter after glycine treatment can be explained by the accumulation of the glycine and unassembled capsid protein inside the cell. Cell radius variation was found to be insufficient to explain the DEP spectra alterations at 10 hours post-infection (Figure 5-6-a).

Figure 5-6-b and d are the box-and-whiskers-plots of cell membrane capacitance for non-infected (controls) and PPV-infected PK-13 cells before and after glycine treatment at $t = 0, 1.5, 4, 8,$ and 10 hours. The first and third quartiles are shown in green color. The mean and standard deviation were utilized to show the cell membrane capacitance statistical value. The cell membrane capacitance of non-infected PK-13 cells (control) was found to be $7.4 \pm 0.4 \text{ mF/m}^2$. Upon infection, the cell membrane capacitance was initially similar to the non-infected PK-13 cells (control). The cell membrane capacitance began to increase after 4 hours suggesting that infection-induced PK-13 cells can be identified as early as 4 hours post-infection. The membrane capacitance of PPV-infected cells increased to $13.3 \pm 1.0 \text{ mF/m}^2$ after 8 hours and settled to $12.7 \pm 0.4 \text{ mF/m}^2$ at 10 hours. The statistical analysis, shown in Figure 5-6-b, revealed significant differences between the cell membrane capacitance of the PPV-infected cells at $t = 0, 1.5,$ and 4 compared to the cells at $t=8$ and 10 hours (*, $p\text{-value} < 0.05$). The results show that C_{mem}

increased by more than 70% over the 10 hours. The membrane capacitance is successfully reflecting charge imbalances during virus membrane infusion, viral component synthesis, and assembly of progeny virus. Similar observation has been reported for different cell lines and viruses [14, 15].

Upon glycine treatment, non-infected PK-13 cells had the membrane capacitance of $7.5 \pm 0.2 \text{ mF/m}^2$. The cell membrane capacitance increased from an initial value of 7.5 ± 0.2 to $8.4 \pm 0.6 \text{ mF/m}^2$ after 4 hours and then up to $9.8 \pm 0.6 \text{ mF/m}^2$ and $10.1 \pm 1.1 \text{ mF/m}^2$ at 8 and 10 hours, respectively. These membrane capacitance values with glycine are lower than without glycine. As shown in Figure 5-6-d, the most significant capacitance decrease was observed for glycine-treated/PPV-infected cells at $t = 8$ and 10 hours whereby the membrane capacitance decreased only by 35.7% and 25.7%, respectively. The markedly reduced membrane capacitance following glycine therapy suggests that this osmolyte drug can significantly halt charge imbalances across the infected membrane.

Previous studies have shown that characteristic capacitance and cell dielectric properties are highly correlated in the viral infection cycles [13-15]. Both increases and decreases in the membrane capacitance have been reported. Differences in characteristic capacitance and cell dielectric properties appear to be specific to the type of virus (enveloped/non-enveloped), viral size, intracellular location of viral protein/capsid assembly, and cell line/size [14]. Further, different trends appear to be associated with membrane composition and membrane folding. Higher values of membrane capacitance

indicate more blebs, folds, ruffles, and microvilli in the cell membrane while lower values demonstrate the loss of microvilli and membrane smoothing [66].

Another potentially valuable application of the DEP technique is viral drug screening through ascertaining the crossover frequency to then determine cell membrane capacitance shifts. As drug molecules penetrate through the cell membrane, the ionic imbalance across the membrane changes, causing the crossover frequency and the cell membrane capacitance to alter. The markedly reduced membrane capacitance following glycine therapy suggests that the drug reduces the complexity of the membrane topography as the infection progress. This study has demonstrated that complexing DEP technology with pathological-based observations increases the quantification and resolvability when monitoring progression of disease electrophysiological markers to vet tailored therapeutic treatment strategies, and possibly even diagnose disease and track disease progression.

5.5. Conclusions

In this study, the membrane-related kinetic mechanism was studied during cell's transition from a healthy to a diseased state in the absence and presence of the antiviral compound. Here, we focused on the membrane properties (i.e. membrane capacitance) of PK-13 cells after PPV infection using dielectrophoresis-based microfluidic devices. To calculate the cell membrane capacitance, differences in DEP spectra of non-infected and PPV-infected PK-13 cells were explored before and after glycine treatment at incubation time points $t = 0, 1.5, 4, 8, \text{ and } 10$ hours. DEP forces were then compiled for cells

experiencing both p-DEP and n-DEP. To calculate the cell membrane capacitance, the f_{CO} and cell size were measured.

Non-infected PK-13 cell populations consistently yielded f_{CO} of 0.45 ± 0.02 MHz. Upon 10 hours of PPV infection, the f_{CO} decreased to 0.27 ± 0.01 MHz. Previous studies showed that virus attachment, penetration, and DNA virus capsid assembly occurs intracellularly over 10 hours post infection [219, 221]. Upon glycine treatment, the DEP spectra displayed attenuated f_{CO} shifts only from 0.44 ± 0.01 MHz down to 0.33 ± 0.02 MHz for the glycine-treated/non-infected and glycine-treated/PPV-infected PK-13 cells, respectively. This suggests that glycine improvements occur post cell infection, but since the virus still penetrates the cell, DEP spectral shifts are still observed compared to the glycine control.

The cell radius was 6.67 ± 0.70 and 6.45 ± 0.83 μm for non-infected PK-13 and glycine-treated/non-infected PK-13 cells, respectively. Upon infection, the measured cell diameters were 6.54 ± 0.75 and 7.12 ± 0.88 μm at 10 hours, correspondingly. Cell size did not change significantly over the 10 hours infection cycle. However, the glycine-treated/PPV-infected PK-13 cells were slightly larger in size, which can be attributed to the accumulation of the glycine and unassembled capsid protein inside the cell.

Finally, each cell population was analyzed to obtain a characteristic pattern of cell membrane capacitance. Upon infection, C_{mem} increased by more than 70% over the 10 hours. Glycine treatment decreased the cell membrane capacitance by 35.7% and 25.7% at 8 and 10 hours, respectively. Our results suggest that glycine improvements occur post cell infection, but since the virus still penetrates the cell, DEP spectral shifts were still

observed relative to the control. The DEP results obtained in this study highlight significant changes in the membrane capacitance earlier in the infection cycle. Our results show that near real-time monitoring of cell membrane capacitance is an excellent indicator of the cell's pathological state. This work linked the dielectric observations with the pathological and as a consequence, the knowledge gained has the potential for dielectric only measurements to be used to infer the pathological state.

Chapter 6: Low Concentration Surfactant Impacts on Red Blood Cell Membrane Integrity and Cellular Viability

6.1. Introduction

Surfactants are traditionally added to alter microfluidic device wall properties making them less apt to bind biomolecules or cells [86, 104]. Results described in Chapter 4 suggest that surfactant molecules can also interact with cell membranes and alter electrokinetic responses. Additional effort was made to further study low concentration surfactant impacts on the red blood cell membrane by correlating membrane integrity and viability alongside dielectrophoretic (DEP) responses. Previous studies have utilized both non-fluorescent and fluorescent dyes to measure cell membrane integrity and viability [239, 240]. Calcein-AM passively crosses the cell membrane of viable cells and converts into the green-fluorescent calcein by cytosolic esterase. Calcein-AM can only be retained by the cells with intact cell membranes while dying or damaged cells with compromised membrane integrity cannot retain calcein-AM and thus do not fluoresce [103].

Cell membrane integrity and viability can be detected and measured based on the fluorescence detection technique such as flow cytometry and microscopy. The calcein-AM loaded red blood cell membrane integrity, viability, and age was studied via flow cytometry [241]. To study membrane integrity, the calcein-AM was measured in the presence and absence of saponin. The saponin was used as a control to initiate cell death. Calcein fluorescence loss was discernable in saponin-treated RBCs with damaged cell membrane compared to the untreated RBCs with an intact cell membrane [241]. The calcein fluorescence intensity of old RBCs decreased which was associated with the

reduction in the esterase activity [241]. When coupled with microscopy, calcein-AM can provide information on the function of the cell membrane and cytoplasm as well [242]. The fluorescence microscopic images of calcein-AM loaded non-infected and malaria-infected RBCs revealed that fluorescence time is sensitive to the local hemoglobin concentration, an iron-containing oxygen-transport metalloprotein in the red blood cells. Calcein-AM has become valuable tools for cell biology and biochemistry. Here, native (0.00 mM) and Triton X-100 treated RBC solutions (0.07-0.17 mM) were tested using non-fluorescent calcein-AM dye to discriminate RBCs based on the intact state of their membranes.

6.2. Materials and Methods

To assess RBC membrane integrity and viability, the membrane-permeable calcein-AM dye (Thermo Fisher Scientific, Waltham, MA, USA) was prepared as a stock solution to 2 mM in dimethyl sulfoxide (Sigma-Aldrich, St. Louis, MO, USA) [239]. Next, 0.2 μ L of calcein-AM stock solution was added to the 1.0% v/v RBC/PBS suspension to a final concentration of 40 μ M. To enable calcein-AM diffusion into intact RBCs, the RBC suspension was immediately vortexed and incubated at 37°C for 30 min. To remove the excess calcein-AM dye in the medium, RBC suspensions were washed with PBS solution via two cycles of centrifugal separation and resuspension. RBCs were then mixed with PBS to 1.0% v/v and exposed to different concentrations of Triton X-100 (0.00, 0.07, 0.11, and 0.17 mM). Finally, images were acquired at 0, 30, 60, and 120 min using a Zeiss Axiovert 200M fluorescence microscope. Calcein-AM was excited with a 485 ± 25 nm bandpass filter, and emissions filtered with a 515 nm long pass filter.

A 510 nm beam splitter was used with the FITC filter to simultaneously acquire video microscopy images and monitor the experiment progression in real time.

Intensity analysis was conducted on the video microscopy images using Image-J software. Cells of interest were selected in the software. Then, the integrated density of the selected cell was measured to find the cell's total fluorescent. To accurately record the total fluorescent of the cell, the measured intensity density was subtracted from the fluorescent background readings. A histogram with an overlaid normal distribution curve also known as Gaussian distribution was utilized to plot the underlying frequency distribution of the measured intensity density. The total fluorescent of each individual cell (I) was divided by the maximum fluorescence value within the cell population, I_m , to calculate the normalized intensity density of the cell population, \bar{I} . Next, the normalized intensity density of the cell population was split into intervals, called bins, ranging from 0.0 to 1.0 for visual representation. The lowest normalized intensity density ($\bar{I} = 0.0$) correlated with the darkest cell contrast while the highest normalized intensity density ($\bar{I} = 1.0$) correlated with the brightest cell contrast. Each bin covered a range of intensities, and the value associated with each bin was the probability of observing a normalized intensity density whose value fell within that bin. Here, the frequencies in each bin were also normalized to the total number of cells in the sampled population.

6.3. Results and Discussion

Intensity analysis of calcein-AM images provided addition insight into the effects of low concentrations of Triton X-100 on RBCs by examining cell membrane integrity and viability. Figure 6-1 shows the frequency bin distribution of the normalized intensity

density of the native and Triton X-100 treated RBC suspensions post calcein-AM staining. Comparison of Figure 6-1-a and Figure 6-1-c illustrate differences between native RBCs (0.00 mM Triton X-100) and 0.17 mM Triton X-100 treated RBCs after calcein-AM staining, respectively. For the native RBC sample, a small nearly insignificant shift was observed for the normalized intensity density after 120 min (Figure 6-1-a). The peak locations of \bar{I} occurred at 0.30 ± 0.14 , 0.27 ± 0.13 , 0.27 ± 0.14 , and 0.32 ± 0.13 at 0, 30, 60, and 120 min, respectively.

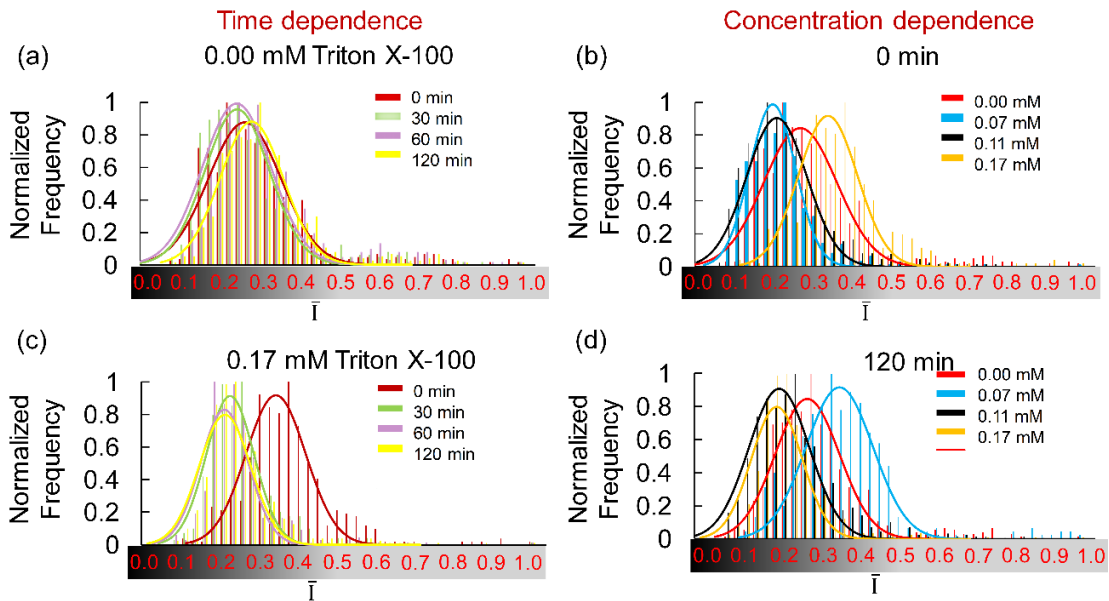


Figure 6-1: Histogram and overlaid normal/Gaussian distribution line of normalized intensity density, \bar{I} , of 1.0% RBC/PBS for time dependent study of (a) native RBC suspensions and (c) 0.17mM Triton X-100 treated RBCs at 0, 30, 60, and 120 min. Calcein-AM was utilized to assess membrane permeability of the RBCs after Triton X-100 treatment. Histogram plot for different concentrations of Triton X-100 treated RBCs at 0.00, 0.07, 0.11, and 0.17 mM at (b) 0 min, and (d) 120 min.

The 0.17 mM data in Figure 6-1-c, illustrates that the normalized intensity density displaced toward lower value of \bar{I} . The \bar{I} of 0.17 mM Triton X-100 RBCs was statistically different at $t=0$ min compared to $t = 30, 50$ and 120 min ($p\text{-value} < 0.06$). At 0.17 mM

Triton X-100 treated RBCs, the peak locations of \bar{I} were at 0.36 ± 0.11 , 0.25 ± 0.09 , 0.24 ± 0.09 , and 0.24 ± 0.10 at 0, 30, 60, and 120 min, respectively. This effect demonstrated that the cell membrane integrity was compromised for a much greater number of cells. Previous studies showed that 0.17 mM Triton X-100 produce pores within HeLa (cancer) cell membranes within 20 min [204]. Drastic reductions in the cells ability to retain the calcein-AM suggests that 0.17 mM Triton X-100 compromised membrane integrity.

Figure 6-1-b and Figure 6-1-d show the concentration-dependent impact of 0.00, 0.07, 0.11, and 0.17 mM Triton X-100 treated RBCs post-calcein-AM staining at 0 and 120 min, respectively. At time 0, normal/Gaussian distribution curves of 0.07 and 0.11 mM concentration overlapped with each other (Figure 6-1-b). The peak locations of \bar{I} were at 0.21 ± 0.09 and 0.22 ± 0.12 for 0.07 and 0.11 mM concentration, respectively. At time 0, normal distribution curves of 0.00 and 0.17 mM Triton X-100 treated RBCs did not show a similar trend to that of 0.07 and 0.11 mM concentration. The peak locations of \bar{I} occurred 0.30 ± 0.14 and 0.36 ± 0.11 for 0.00 and 0.17 mM concentration, respectively. These results show that the presence of Triton X-100 can interfere with esterase activity during an early stage of the RBCS calcein-AM labeling.

As mentioned above, the normal distribution curve of 0.00 mM concentration did not change significantly compared to the normal distribution curve over 120 min (Figure 6-1-a and d). Over 120 min, 0.07 and 0.11 mM Triton X-100 concentration \bar{I} shifted toward higher value, an increase of 43% and 13%, respectively (compare Figure 6-1-b and Figure 6-1-d). The increase in \bar{I} value at 0.07 and 0.11 Triton X-100 concentration showed that the RBC membranes did not compromise over 120 min (Figure 6-1-b and

Figure 6-1-d). These calcein-AM results corroborate with previous findings whereby minimal cell integrity changes occurred at 0.07 mM and 0.11 mM. The increase of calcein-AM in the presence of 0.07 and 0.11 mM Triton X-100 can be due to the RBC morphological responses. At $t = 120$ min, as the Triton X-100 concentration increases from 0.00 to 0.11 mM, RBCs transformed from biconcave with bright circular interiors to stomatocyte shapes and linear slit-like interior profiles (Figure 4-2-b). Previous studies show that fluorescence variation depends on the pH, intracellular concentration of free iron, hemoglobin, and other pigmented molecules [243]. Finally, the decreases in \bar{I} value at 0.17 mM Triton X-100 concentration is due to calcein leakage into the surrounding medium.

In summary, calcein-AM staining was used as an indicator of RBC membrane integrity and viability. Our results here were consistent with the previously discussed DEP behavior in chapter 4. This work has not yet moved toward publication; but it will be further developed and expanded for publication in the future.

Chapter 7: Conclusions and Future Works

7.1 Introduction

Microfluidic devices have been developed to miniaturize one or multiple analytical and diagnostic techniques for fast, label-free, low-cost, and accessible applications [1]. In combination with the electrokinetic techniques, microfluidic systems have made analytical and diagnostic techniques more ubiquitous [2-10]. In the 1950s, Pohl first demonstrated particle motion could be induced by non-uniform AC electric fields, which was later termed dielectrophoresis [244, 245] from the origins of two behaviors (di), electric-field induced (electro) and motion (phoresis). In the past two decades, dielectrophoresis has expanded extensively into biomedical science after its potential in numerous diagnosis, therapeutics, and drug discovery areas was demonstrated [11-15]. Dielectrophoretic behavior has proven to be highly dependable on medium conditions consistent between both theoretical and experimental analyses. In most published work, medium conditions around the target analyte have been assumed to be constant with respect to pH, ionic concentration and ionic strength, and that the medium has minimal dynamic interactions with the analyte (e.g. cell, (bio)molecule) [30, 51, 206]. However, the large ratio of surface area to volume of microfluidic devices creates the possibility for the microenvironment to be changed rapidly with surface area driven effects [246]. Subsequently, the target bioanalyte (i.e. cells) can inherit the properties of its microenvironment [66]. Previous research in our lab demonstrated that unwanted secondary phenomena can influence the [66] medium and thus alter a previously comfortable physiological state for cells in the medium [16, 17]. Research in traditional

biological lab settings have demonstrated that medium changes can ultimately affect cellular metabolomics, properties and viability [247]. Dielectrophoretic studies have demonstrated cell status is discernable from cell responses to different electric fields including live/dead yeast cells , malaria infected/healthy blood cells [31, 32], etc. In this dissertation, multiple non-ideal unwanted secondary phenomena that affected cellular properties and viability were investigated in two AC dielectrophoresis-based microfluidic devices. The first undesired secondary phenomenon that was studied in this dissertation (Chapter 3) was the generation and release of Faradaic reaction byproducts within the medium that lead to biocompatibility changes in spatially non-uniform AC dielectrophoresis-based microdevice. In the second part of this dissertation (Chapters 4 and 6), Triton X-100 surfactant impact on the medium solution was explored. Finally, a comprehensive level of understanding led us to utilize dielectrophoresis in its full capacity as a tool to monitor the state and progression of virus infection in cells in the presence and absence of an antiviral compound (Chapter 5). Glycine was examined as an antiviral compound to reduce porcine parvovirus (PPV) infection in porcine kidney (PK-13) cells.

7.2 Biocompatibility Change in Spatially Non-uniform AC DEP

The research performed in Chapter 3 described the human red blood cell hemolysis in the presence and absence of medium complications resulting from Faradaic reactions. Strategies to impede complications from ion behavior at the microscale included either preventing ion generation or protecting cells from pH and/or tonicity changes. The first strategy employed herein was to physically isolate electrodes from the medium with a

HfO₂ passivation layer to suppress Faradaic reactions and thus ionic byproducts at the electrode surface. It was shown that HfO₂ layer can successfully suppress Faradaic reactions. The second strategy was to protect the cell by stabilizing the cell membrane with Triton X-100. It was shown that low concentrations of non-ionic surfactant (<1%) stabilized and protected cell membranes as the medium deviated from isotonic conditions. Through comparisons against multiple control experiments, it was proven that red blood cell swelling, and hemolysis was induced by the change of fluid biocompatibility. The impact of Faradaic reactions on electrodes was studied via optical surface profiles for the uncoated and HfO₂ coated T-shaped electrodes before and after ~15 experiments. The uncoated T-shaped electrodes lost 25 μm of Au layer around the electrode edge, while the HfO₂ coated electrodes show smooth cross-sections of the electrode after ~15 experiments.

Potential future work still needs to be completed on this topic:

- The work in Chapter 4 only studied Faradaic reaction byproducts impact on human red blood cells in non-uniform AC electric fields. This theory can be examined on cell wall structures different than RBCs such as bacteria, yeast, cancer, and other mammalian cells. Similarities and differences between the RBC and other cellular systems can help to achieve a more complete understanding of Faradaic reaction influences on cell lysis.
- Scanning electrochemical microscope (SECM) can be used for direct spatial imaging of Faradaic reaction products and their mass transport through a microchamber. SECM can be utilized to map the local solution pH and

conductivity versus time and proximity from the dielectrophoretic electrodes. Mapping the solution pH and conductivity in two dimensional space would provide additional information about the ionic distribution and would provide direct information about ions that are not measured indirectly via hemolysis.

- Cellular properties and viability are affected by numerous other factors such as added salts, sugars, pH and ion buffers, amino acids and proteins within the medium. Various cell culture media include chemical additives to maintain cells in a physiologically viable state as well as to enhance the performance of the microfluidic platform. These media solutions could be further examined to better understand the buffering capabilities of additives.

7.3 Interactions Between Biological Cell and DEP Medium Additives

Surfactants are regularly added to cell-buffer solutions to improve reproducibility and are assumed to not visibly disrupt protein composition of cell membranes or cell viability. In nonelectrokinetic systems, surfactants have been shown to intercalate into cell membranes [54]. Previous studies have shown that surfactant molecules can protect red blood cells against hypo-osmotic lysis at low concentrations; however, at higher concentrations, surfactant can rupture red blood cells and release their contents into the surrounding medium [108, 178]. In electrokinetic systems, surfactants have been shown to reduce interfacial tensions and prevent analyte sticking [50-54]. However, no previous study has explored whether surfactants added in electrokinetic systems alter cell properties. Investigations to explore whether a surfactant could alter cell properties was essential to accurately monitor and subsequently control precise DEP behavior of cells. In

Chapter 4 and 6, we studied the impacts of Triton X-100 surfactant with human red blood cells (RBCs) via traditional biological tools such as ultraviolet-visible spectroscopy (UV-Vis), fluorescent viability markers, and dielectrophoresis (DEP) to compare non-electrokinetic and electrokinetic responses, respectively [publication pending].

Increasing Triton X-100 (0.00-0.17 mM) increased the RBC cell size by 11%. UV-Vis spectroscopy of Triton X-100 treated RBCs were dramatically different from that of native RBCs. Further, the presence of low concentrations of Triton X-100 shifted RBC's DEP spectra yielding lower crossover frequencies (f_{CO}). Membrane capacitance increased from 11.51 mF/m² for native (0.00 mM) to 14.05 mF/m² for 0.07 mM Triton X-100 treated cells, respectively, while it only increased to 13.61 mF/m² for 0.11 mM Triton X-100 treated cells. The single-shell oblate model revealed that cell radius and membrane permittivity were the dominant influences on DEP spectral shifts and cell membrane capacitance alteration.

In chapter 6, we further studied the impact of Triton X-100 on the cell membrane integrity and viability via calcein-am. Cell membrane integrity and viability did not change significantly at 0.11 mM and 0.07 mM Triton X-100 concentrations. At 0.17 mM Triton X-100 concentration, significant loss of calcein-AM indicated more lysis and compromised cell membrane integrity.

Potential future work still needs to be completed on this topic:

- The frequency dependencies inspected in Chapter 4 and 6 were in the kHz range, which do not provide insights into internal cell structure. Attempts should be

made on higher frequencies (i.e, MHz range) to explore changed to the cell cytosol.

- In this research, frequency sweep rate was utilized to rapidly collect data for the cell's DEP frequency spectrum. Semi-automated and automated techniques were utilized to analyze the collected. The semi-automated and automated techniques were performed with ImageJ® Tracker 4.11.0 software, respectively. Although the automated technique provided improvement in cell analysis, it was still time-consuming since each cell had to be introduced manually to the Tracker 4.11.0 software. For further improvements, MATLAB code could be written and implemented to automatically select cells of interest. Such a technique would remove human bias in cell selection.
- Other surfactants including ionic surfactants should be researched to further study the roles and impacts common surfactants in electrokinetic microdevices may experience and their role on cell dielectric properties (membrane and cytosol).
- In this research, we employed the single-shell oblate DEP polarization model to calculate and ascertain the dielectric properties of Triton X-100 treated RBCs. Models approximating cell geometries could be further explored by employing a numerical method to fully incorporate the RBC biconcave shape or other analytical/numerical approximations for other cell types.

7.4 Utilize Dielectrophoresis-Based Microfluidics in its Full Capacity

The knowledge gained from ion and surfactant behaviors were applied in Chapter 5, where my research explored the ability to monitor the state and progression of virus

infection in the absence and presence of the osmolyte glycine. Glycine was previously examined as a natural antiviral compound which was proven to reduce porcine parvovirus (PPV) infection in porcine kidney (PK-13) cells [219]. Here, we studied the time dependent membrane perturbation mechanism of the virus in the presence and absence of the antiviral osmolyte, glycine. Dielectrophoretic spectra were compiled from cell velocities to determine DEP force and crossover frequency (f_{co}) for non-infected and PPV-infected PK-13 cells in the presence and absence of glycine. The results suggested that the cell membrane capacitance, which can be derived from the cell membrane polarization, was increased with PPV infection over the time progression of virus attachment, penetration, and capsid protein production and assembly [publication pending]. For glycine-treated/PPV-infected cells, cells displayed attenuated cell membrane capacitance shifts from the PPV-infected cells making the DEP profile similar to non-infected PPV cells. This work indicates DEP's potential to passively monitor membrane-related mechanisms throughout viral infection. This work further demonstrated that it could serve as a rapid, noninvasive tool to explore the efficacy of antiviral compounds including classes of natural compounds.

Potential future work still needs to be completed on this topic:

- In this research, we studied the membrane-related time-dependent mechanisms during early viral infection in the absence and presence of the osmolyte glycine. Future work should focus on other antiviral compounds (ribavirin [248], interferon- α (IFN- α) [248], 6-azauridine [248], glycyrrhizin [248], and iminocyclitol [249]) and their DEP behavior. Since the time dependent changes

are discernable, this tool provides insight into the mechanisms by which antiviral compounds work.

- In this research, we explored frequencies that ranged from 0.1 to 0.9 MHz in the β -dispersion region. At higher frequencies from this range, the DEP behavior depends upon the relaxation time of the medium and cytoplasm [30]. Future work could focus on the cell interior by studying DEP behavior over higher frequency ranges from MHz into GHz. Especially with the virus replication cycle and antiviral compounds, this may provide insights into the replication and encapsulation stage of viral infections.
- Early diagnosis can result in early treatment and increase survival rates against deadly viruses. Future work should focus on optimizing device design, ease of use, and performance in order to build towards a clinically applicable method.

7.5 Contribution of Our Work to Dielectrophoresis Field

Exploring the role and impacts of microscale phenomena on electrode, microdevice, and cellular function will likely have significant impacts on future generations of microdevices. Understanding the underlying microscale phenomena, to either strategically induce or suppress it, will lead to more reliable, reproducible electrokinetic (including DEP) tools. Unwanted secondary phenomena are more pronounced in microscale systems due to small fluid volumes and large interfacial areas. This study filled a critical gap in knowledge by determining the extent and impacts of one class of unwanted secondary phenomena in electrokinetic microdevices: Faradaic reactions and ion motion. This research explored the fundamental behaviors of ionic byproducts

released into the medium within microchambers including their impact on biological cells in dielectrophoretic fields. This research also demonstrated the importance of solution biocompatibility properties on cell properties and viability.

We also showed that changes in cell membrane properties with surfactant intercalation alters cell response to an AC electric field. The DEP results obtained in this study highlight significant changes in the membrane capacitance in the presence of low concentration Triton X-100. Since DEP-based microfluidic systems are gaining commercial traction for portable medical diagnostic applications, it is important to include the effects of the secondary chemical interactions between cells. This work showed the importance of measuring and addressing these phenomena in order to accurately catalog cell properties and engineer reliable microfluidic DEP devices.

Finally, we were able to show comprehensive correlation between dynamic cell property changes observed with traditional cell observation techniques and electrokinetic techniques. This correlation strategy led us to utilize dielectrophoresis in its full capacity as a tool to monitor the state and progression of virus infection in PK-13 cells as well as anti-viral activities of an osmolyte compound.

This work collectively raised the rigor and ability to obtain more accurate and reliable dielectric property data from microfluidic systems. It demonstrated attention should be paid to electrochemical reactions at electrode surfaces and that care should be taken when designing future electrokinetic systems with embedded metal electrodes. This research also demonstrated that operational conditions should be selected carefully to avoid non-ideal unwanted secondary phenomena. This work was the first to demonstrate

that surfactants alter cell properties in electrokinetic microdevices and thus should be separately controlled for in future experiments employing these additives to reduce sticking. Lastly, controlling for these variables enabled precise monitoring of the viral infection cycle and osmolyte anti-viral activity, which has previously not been demonstrated.

References

- [1] A.R. Minerick, The rapidly growing field of micro and nanotechnology to measure living cells, *AIChE journal*, 54 (2008) 2230-2237.
- [2] D.R. Walt, Miniature analytical methods for medical diagnostics, *Science*, 308 (2005) 217-219.
- [3] G.M. Whitesides, The origins and the future of microfluidics, *Nature*, 442 (2006) 368.
- [4] K.-H. Han, R.D. McConnell, C.J. Easley, J.M. Bienvenue, J.P. Ferrance, J.P. Landers, A.B. Frazier, An active microfluidic system packaging technology, *Sensors and Actuators B: Chemical*, 122 (2007) 337-346.
- [5] M.A. Burns, Everyone's a (future) chemist, *Science*, 296 (2002) 1818-1819.
- [6] H. Shafiee, J.L. Caldwell, R.V. Davalos, A microfluidic system for biological particle enrichment using contactless dielectrophoresis, *JALA: Journal of the Association for Laboratory Automation*, 15 (2010) 224-232.
- [7] A. Salmanzadeh, L. Romero, H. Shafiee, R.C. Gallo-Villanueva, M.A. Stremler, S.D. Cramer, R.V. Davalos, Isolation of prostate tumor initiating cells (TICs) through their dielectrophoretic signature, *Lab on a Chip*, 12 (2012) 182-189.
- [8] J. Zhu, X. Xuan, Curvature-induced dielectrophoresis for continuous separation of particles by charge in spiral microchannels, *Biomicrofluidics*, 5 (2011) 024111.
- [9] B.H. Lapizco-Encinas, M. Rito-Palomares, Dielectrophoresis for the manipulation of nanobioparticles, *Electrophoresis*, 28 (2007) 4521-4538.
- [10] E.D. Pratt, C. Huang, B.G. Hawkins, J.P. Gleghorn, B.J. Kirby, Rare cell capture in microfluidic devices, *Chemical engineering science*, 66 (2011) 1508-1522.
- [11] M. Alshareef, N. Metrakos, E. Juarez Perez, F. Azer, F. Yang, X. Yang, G. Wang, Separation of tumor cells with dielectrophoresis-based microfluidic chip, *Biomicrofluidics*, 7 (2013) 11803.
- [12] K.A. Graham, H.J. Mulhall, F.H. Labeed, M.P. Lewis, K.F. Hoettges, N. Kalavrezos, J. McCaul, C. Liew, S. Porter, S. Fedele, M.P. Hughes, A dielectrophoretic method of discrimination between normal oral epithelium, and oral and oropharyngeal cancer in a clinical setting, *Analyst*, 140 (2015) 5198-5204.
- [13] S. Archer, H. Morgan, F.J. Rixon, Electrorotation studies of baby hamster kidney fibroblasts infected with herpes simplex virus type 1, *Biophysical journal*, 76 (1999) 2833-2842.
- [14] E. Petiot, S. Ansorge, M. Rosa-Calatrava, A. Kamen, Critical phases of viral production processes monitored by capacitance, *Journal of biotechnology*, 242 (2017) 19-29.
- [15] B. Yafouz, N.A. Kadri, H.A. Rothan, R. Yusof, F. Ibrahim, Discriminating dengue-infected hepatic cells (WRL-68) using dielectrophoresis, *Electrophoresis*, 37 (2016) 511-518.
- [16] R. An, K. Massa, D.O. Wipf, A.R. Minerick, Solution pH change in non-uniform alternating current electric fields at frequencies above the electrode charging frequency, *Biomicrofluidics*, 8 (2014) 064126.
- [17] R. An, D.O. Wipf, A.R. Minerick, Spatially variant red blood cell crenation in alternating current non-uniform fields, *Biomicrofluidics*, 8 (2014) 021803.
- [18] P. García-Sánchez, A. Ramos, A. González, N.G. Green, H. Morgan, Flow reversal in traveling-wave electrokinetics: An analysis of forces due to ionic concentration gradients, *Langmuir*, 25 (2009) 4988-4997.
- [19] W.Y. Ng, Y.C. Lam, I. Rodríguez, Experimental verification of Faradaic charging in ac electrokinetics, *Biomicrofluidics*, 3 (2009) 022405.

- [20] E. De Leo, L. Galluccio, A. Lombardo, G. Morabito, Networked labs-on-a-chip (NLoC): Introducing networking technologies in microfluidic systems, *Nano Communication Networks*, 3 (2012) 217-228.
- [21] S. Nahavandi, S. Baratchi, R. Soffe, S.-Y. Tang, S. Nahavandi, A. Mitchell, K. Khoshmanesh, Microfluidic platforms for biomarker analysis, *Lab on a Chip*, 14 (2014) 1496-1514.
- [22] T.B. Jones, T.B. Jones, *Electromechanics of particles*, Cambridge University Press, Place Published, 2005.
- [23] H. Morgan, N.G. Green, *AC electrokinetics*, Research Studies Press, Place Published, 2003.
- [24] A. Bandopadhyay, D. Tripathi, S. Chakraborty, Electroosmosis-modulated peristaltic transport in microfluidic channels, *Physics of Fluids*, 28 (2016) 052002.
- [25] R. Zhang, S. Wang, M.H. Yeh, C. Pan, L. Lin, R. Yu, Y. Zhang, L. Zheng, Z. Jiao, Z.L. Wang, A streaming potential/current-based microfluidic direct current generator for self-powered nanosystems, *Advanced Materials*, 27 (2015) 6482-6487.
- [26] D. Tripathi, S. Bhushan, O.A. Bég, Analytical study of electro-osmosis modulated capillary peristaltic hemodynamics, *Journal of Mechanics in Medicine and Biology*, 17 (2017) 1750052.
- [27] B. Abécassis, C. Cottin-Bizonne, C. Ybert, A. Ajdari, L. Bocquet, Osmotic manipulation of particles for microfluidic applications, *New Journal of Physics*, 11 (2009) 075022.
- [28] S. De Groot, P. Mazur, J.T.G. Overbeek, Nonequilibrium thermodynamics of the sedimentation potential and electrophoresis, *The Journal of Chemical Physics*, 20 (1952) 1825-1829.
- [29] P.R. Gascoyne, X.-B. Wang, Y. Huang, F.F. Becker, Dielectrophoretic separation of cancer cells from blood, *IEEE transactions on industry applications*, 33 (1997) 670-678.
- [30] Z. Gagnon, J. Gordon, S. Sengupta, H.C. Chang, Bovine red blood cell starvation age discrimination through a glutaraldehyde-amplified dielectrophoretic approach with buffer selection and membrane cross-linking, *Electrophoresis*, 29 (2008) 2272-2279.
- [31] P. Gascoyne, J. Satayavivad, M. Ruchirawat, Microfluidic approaches to malaria detection, *Acta tropica*, 89 (2004) 357-369.
- [32] P. Gascoyne, R. Pethig, J. Satayavivad, F.F. Becker, M. Ruchirawat, Dielectrophoretic detection of changes in erythrocyte membranes following malarial infection, *Biochimica et Biophysica Acta (BBA)-Biomembranes*, 1323 (1997) 240-252.
- [33] K. Khoshmanesh, S. Nahavandi, S. Baratchi, A. Mitchell, K. Kalantar-zadeh, Dielectrophoretic platforms for bio-microfluidic systems, *Biosensors and Bioelectronics*, 26 (2011) 1800-1814.
- [34] B. Cetin, D. Li, Effect of Joule heating on electrokinetic transport, *Electrophoresis*, 29 (2008) 994-1005.
- [35] G. Hu, Q. Xiang, R. Fu, B. Xu, R. Venditti, D. Li, Electrokinetically controlled real-time polymerase chain reaction in microchannel using Joule heating effect, *Analytica Chimica Acta*, 557 (2006) 146-151.
- [36] X.-H. Fang, M. Adams, J. Pawliszyn, A model of thermally generated pH gradients in tapered capillaries, *Analyst*, 124 (1999) 335-341.
- [37] S.M. Kim, G.J. Sommer, M.A. Burns, E.F. Hasselbrink, Low-Power Concentration and Separation Using Temperature Gradient Focusing via Joule Heating, *Analytical Chemistry*, 78 (2006) 8028-8035.
- [38] S.F. Cogan, A.A. Guzelian, W.F. Agnew, T.G. Yuen, D.B. McCreery, Over-pulsing degrades activated iridium oxide films used for intracortical neural stimulation, *Journal of neuroscience methods*, 137 (2004) 141-150.

- [39] H.Y. Lee, C. Barber, A.R. Minerick, Improving electrokinetic microdevice stability by controlling electrolysis bubbles, *Electrophoresis*, 35 (2014) 1782-1789.
- [40] Z. Wang, C. Ivory, A.R. Minerick, Surface isoelectric focusing (sIEF) with carrier ampholyte pH gradient, *Electrophoresis*, 38 (2017) 2565-2575.
- [41] A. Gencoglu, A. Minerick, Chemical and morphological changes on platinum microelectrode surfaces in AC and DC fields with biological buffer solutions, *Lab on a Chip*, 9 (2009) 1866-1873.
- [42] Y.W. Yoo, W. Jeon, W. Lee, C.H. An, S.K. Kim, C.S. Hwang, Structure and electrical properties of Al-doped HfO₂ and ZrO₂ films grown via atomic layer deposition on Mo electrodes, *ACS applied materials & interfaces*, 6 (2014) 22474-22482.
- [43] Y.W. Chen, M. Liu, T. Kaneko, P.C. McIntyre, Atomic layer deposited hafnium oxide gate dielectrics for charge-based biosensors, *Electrochemical and Solid-State Letters*, 13 (2010) G29-G32.
- [44] J.L. Collins, H. Moncada Hernandez, S. Habibi, C.E. Kendrick, Z. Wang, N. Bihari, P.L. Bergstrom, A.R. Minerick, Electrical and chemical characterizations of hafnium (IV) oxide films for biological lab-on-a-chip devices, *Thin Solid Films*, 662 (2018) 60-69.
- [45] M. Szymańska, S. Gierałtowska, Ł. Wachnicki, M. Grobelny, K. Makowska, R. Mroczyński, Effect of reactive magnetron sputtering parameters on structural and electrical properties of hafnium oxide thin films, *Applied Surface Science*, 301 (2014) 28-33.
- [46] Y. Temiz, A. Ferretti, Y. Leblebici, C. Guiducci, A comparative study on fabrication techniques for on-chip microelectrodes, *Lab on a Chip*, 12 (2012) 4920-4928.
- [47] H. Cesiulis, N. Tsyntsar, A. Ramanavicius, G. Ragoisha, The study of thin films by electrochemical impedance spectroscopy, *Nanostructures and thin films for multifunctional applications*, Springer, Place Published, 2016, pp. 3-42.
- [48] A. Lasia, *Electrochemical impedance spectroscopy and its applications*, Modern aspects of electrochemistry, Springer, Place Published, 2002, pp. 143-248.
- [49] P. García-Sánchez, A. Ramos, N.G. Green, H. Morgan, Traveling-Wave Electrokinetic Micropumps: Velocity, Electrical Current, and Impedance Measurements, *Langmuir*, 24 (2008) 9361-9369.
- [50] K. Khoshmanesh, C. Zhang, F.J. Tovar-Lopez, S. Nahavandi, S. Baratchi, K. Kalantar-zadeh, A. Mitchell, Dielectrophoretic manipulation and separation of microparticles using curved microelectrodes, *Electrophoresis*, 30 (2009) 3707-3717.
- [51] H.Y. Lee, C. Barber, J.A. Rogers, A.R. Minerick, Electrochemical hematocrit determination in a direct current microfluidic device, *Electrophoresis*, 36 (2015) 978-985.
- [52] E. Rosales-Cruzaley, P.A. Cota-Elizondo, D. Sanchez, B.H. Lapizco-Encinas, Sperm cells manipulation employing dielectrophoresis, *Bioprocess and biosystems engineering*, 36 (2013) 1353-1362.
- [53] S.Y. Tang, W. Zhang, P. Yi, S. Baratchi, K. Kalantar-zadeh, K. Khoshmanesh, Reorientation of microfluidic channel enables versatile dielectrophoretic platforms for cell manipulations, *Electrophoresis*, 34 (2013) 1407-1414.
- [54] K. Parsi, Interaction of detergent sclerosants with cell membranes, *Phlebology*, 30 (2015) 306-315.
- [55] H.A. Pohl, I. Hawk, Separation of living and dead cells by dielectrophoresis, *Science*, 152 (1966) 647-649.
- [56] E.O. Adekanmbi, S.K. Srivastava, Dielectrophoretic applications for disease diagnostics using lab-on-a-chip platforms, *Lab on a Chip*, 16 (2016) 2148-2167.

- [57] I.F. Cheng, H.C. Chang, D. Hou, H.C. Chang, An integrated dielectrophoretic chip for continuous bioparticle filtering, focusing, sorting, trapping, and detecting, *Biomicrofluidics*, 1 (2007) 21503.
- [58] P.V. Jones, S.J. Staton, M.A. Hayes, Blood cell capture in a sawtooth dielectrophoretic microchannel, *Analytical and bioanalytical chemistry*, 401 (2011) 2103-2111.
- [59] K.M. Leonard, Alternating current dielectrophoretic manipulation of erythrocytes in medical microdevice technology, (2012).
- [60] Y.-H. Lin, G.-B. Lee, An optically induced cell lysis device using dielectrophoresis, *Applied Physics Letters*, 94 (2009) 033901.
- [61] S.K. Ameri, P.K. Singh, S. Sonkusale, Utilization of graphene electrode in transparent microwell arrays for high throughput cell trapping and lysis, *Biosensors & bioelectronics*, 61 (2014) 625-630.
- [62] H. Lu, M.A. Schmidt, K.F. Jensen, A microfluidic electroporation device for cell lysis, *Lab Chip*, 5 (2005) 23-29.
- [63] Q. Ramadan, V. Samper, D. Poenar, Z. Liang, C. Yu, T.M. Lim, Simultaneous cell lysis and bead trapping in a continuous flow microfluidic device, *Sensors and Actuators B: Chemical*, 113 (2006) 944-955.
- [64] G. Mernier, N. Piacentini, T. Braschler, N. Demierre, P. Renaud, Continuous-flow electrical lysis device with integrated control by dielectrophoretic cell sorting, *Lab Chip*, 10 (2010) 2077-2082.
- [65] B. Yafouz, N.A. Kadri, H.A. Rothan, R. Yusof, F. Ibrahim, Discriminating dengue-infected hepatic cells (WRL-68) using dielectrophoresis, *Electrophoresis*, 37 (2016) 511-518.
- [66] R.R. Pethig, *Dielectrophoresis: Theory, methodology and biological applications*, John Wiley & Sons, Place Published, 2017.
- [67] A. Ismail, M.P. Hughes, H.J. Mulhall, R.O. Oreffo, F.H. Labeed, Characterization of human skeletal stem and bone cell populations using dielectrophoresis, *Journal of tissue engineering and regenerative medicine*, 9 (2015) 162-168.
- [68] C. Huang, H. Liu, N.H. Bander, B.J. Kirby, Enrichment of prostate cancer cells from blood cells with a hybrid dielectrophoresis and immunocapture microfluidic system, *Biomedical microdevices*, 15 (2013) 941-948.
- [69] X. Liang, K.A. Graham, A.C. Johannessen, D.E. Costea, F.H. Labeed, Human oral cancer cells with increasing tumorigenic abilities exhibit higher effective membrane capacitance, *Integrative biology : quantitative biosciences from nano to macro*, 6 (2014) 545-554.
- [70] T.N. Adams, P.A. Turner, A.V. Janorkar, F. Zhao, A.R. Minerick, Characterizing the dielectric properties of human mesenchymal stem cells and the effects of charged elastin-like polypeptide copolymer treatment, *Biomicrofluidics*, 8 (2014) 054109.
- [71] M.E. Forero, M. Marin, A. Corrales, I. Llano, H. Moreno, M. Camacho, *Leishmania amazonensis* infection induces changes in the electrophysiological properties of macrophage-like cells, *The Journal of membrane biology*, 170 (1999) 173-180.
- [72] X. Chen, D. Cui, C. Liu, H. Li, J. Chen, Continuous flow microfluidic device for cell separation, cell lysis and DNA purification, *Anal Chim Acta*, 584 (2007) 237-243.
- [73] P. Marmottant, S. Hilgenfeldt, Controlled vesicle deformation and lysis by single oscillating bubbles, *Nature*, 423 (2003) 153.
- [74] J. Kim, S. Hee Jang, G. Jia, J.V. Zoval, N.A. Da Silva, M.J. Madou, Cell lysis on a microfluidic CD (compact disc), *Lab Chip*, 4 (2004) 516-522.
- [75] D. Di Carlo, K.H. Jeong, L.P. Lee, Reagentless mechanical cell lysis by nanoscale barbs in microchannels for sample preparation, *Lab Chip*, 3 (2003) 287-291.

- [76] H. Takamatsu, R. Takeya, S. Naito, H. Sumimoto, On the mechanism of cell lysis by deformation, *Journal of biomechanics*, 38 (2005) 117-124.
- [77] M. Shehadul Islam, A. Aryasomayajula, P. Selvaganapathy, A review on macroscale and microscale cell lysis methods, *Micromachines*, 8 (2017) 83.
- [78] D. Di Carlo, C. Ionescu-Zanetti, Y. Zhang, P. Hung, L.P. Lee, On-chip cell lysis by local hydroxide generation, *Lab on a Chip*, 5 (2005) 171-178.
- [79] S. Yan, P. Chen, X. Zeng, X. Zhang, Y. Li, Y. Xia, J. Wang, X. Dai, X. Feng, W. Du, Integrated multifunctional electrochemistry microchip for highly efficient capture, release, lysis, and analysis of circulating tumor cells, *Analytical chemistry*, 89 (2017) 12039-12044.
- [80] H.J. Lee, J.-H. Kim, H.K. Lim, E.C. Cho, N. Huh, C. Ko, J.C. Park, J.-W. Choi, S.S. Lee, Electrochemical cell lysis device for DNA extraction, *Lab on a Chip*, 10 (2010) 626-633.
- [81] S.K. Jha, G.-S. Ra, G.-S. Joo, Y.-S. Kim, Electrochemical cell lysis on a miniaturized flow-through device, *Current Applied Physics*, 9 (2009) e301-e303.
- [82] J.T. Nevill, R. Cooper, M. Dueck, D.N. Breslauer, L.P. Lee, Integrated microfluidic cell culture and lysis on a chip, *Lab on a Chip*, 7 (2007) 1689-1695.
- [83] H. Lodish, A. Berk, S.L. Zipursky, P. Matsudaira, D. Baltimore, J. Darnell, *Molecular cell biology*, WH freeman New York, Place Published, 2013.
- [84] B. Hille, *Ion channels of excitable membranes*, Sinauer Sunderland, MA, Place Published, 2001.
- [85] D. Mark, S. Haeberle, G. Roth, F. von Stetten, R. Zengerle, Microfluidic lab-on-a-chip platforms: requirements, characteristics and applications, *Chemical Society Reviews*, 39 (2010) 1153-1182.
- [86] S.-Y. Tang, W. Zhang, S. Baratchi, M. Nasabi, K. Kalantar-zadeh, K. Khoshmanesh, Modifying Dielectrophoretic Response of Nonviable Yeast Cells by Ionic Surfactant Treatment, *Analytical Chemistry*, 85 (2013) 6364-6371.
- [87] N. Winograd, T. Kuwana, Characteristics of the electrode-solution interface under faradaic and non-faradaic conditions as observed by internal reflection spectroscopy, *Journal of Electroanalytical Chemistry and Interfacial Electrochemistry*, 23 (1969) 333-342.
- [88] A. Hassibi, R. Navid, R.W. Dutton, T.H. Lee, Comprehensive study of noise processes in electrode electrolyte interfaces, *Journal of applied physics*, 96 (2004) 1074-1082.
- [89] D.C. Grahame, Electrode processes and the electrical double layer, *Annual review of physical chemistry*, 6 (1955) 337-358.
- [90] A. Gonzalez, A. Ramos, P. Garcia-Sanchez, A. Castellanos, Effect of the combined action of Faradaic currents and mobility differences in ac electro-osmosis, *Physical review. E, Statistical, nonlinear, and soft matter physics*, 81 (2010) 016320.
- [91] O.D. Velev, S. Gangwal, D.N. Petsev, Particle-localized AC and DC manipulation and electrokinetics, *Annual Reports Section" C"(Physical Chemistry)*, 105 (2009) 213-246.
- [92] N.M. Contento, P.W. Bohn, Tunable electrochemical pH modulation in a microchannel monitored via the proton-coupled electro-oxidation of hydroquinone, *Biomicrofluidics*, 8 (2014) 044120.
- [93] L.-J. Cheng, H.-C. Chang, Switchable pH actuators and 3D integrated salt bridges as new strategies for reconfigurable microfluidic free-flow electrophoretic separation, *Lab on a Chip*, 14 (2014) 979-987.
- [94] J. Hasted, D. Ritson, C. Collie, Dielectric properties of aqueous ionic solutions. Parts I and II, *The Journal of Chemical Physics*, 16 (1948) 1-21.
- [95] R. Buchner, J. Barthel, 9 Dielectric relaxation in solutions, *Annual Reports Section" C"(Physical Chemistry)*, 97 (2001) 349-382.

- [96] M. Tait, A. Suggett, F. Franks, S. Ablett, P. Quickenden, Hydration of monosaccharides: A study by dielectric and nuclear magnetic relaxation, *Journal of Solution Chemistry*, 1 (1972) 131-151.
- [97] W. Guo, X. Zhu, Y. Liu, H. Zhuang, Sugar and water contents of honey with dielectric property sensing, *Journal of Food Engineering*, 97 (2010) 275-281.
- [98] J. Wyman Jr, Dielectric constants of polar solutions, *Journal of the American Chemical Society*, 56 (1934) 536-544.
- [99] J. Oncley, The Investigation of Proteins by Dielectric Measurements, *Chemical Reviews*, 30 (1942) 433-450.
- [100] M.J. Rosen, J.T. Kunjappu, *Surfactants and interfacial phenomena*, John Wiley & Sons, Place Published, 2012.
- [101] L. Mazutis, J. Gilbert, W.L. Ung, D.A. Weitz, A.D. Griffiths, J.A. Heyman, Single-cell analysis and sorting using droplet-based microfluidics, *Nature protocols*, 8 (2013) 870-891.
- [102] R.V. Davalos, G.J. McGraw, T.I. Wallow, A.M. Morales, K.L. Krafcik, Y. Fintschenko, E.B. Cummings, B.A. Simmons, Performance impact of dynamic surface coatings on polymeric insulator-based dielectrophoretic particle separators, *Analytical and bioanalytical chemistry*, 390 (2008) 847-855.
- [103] G. Ocuvirk, H. Salimi-Moosavi, R.J. Szarka, E.A. Arriaga, P.E. Andersson, R. Smith, N.J. Dovichi, D.J. Harrison, β -galactosidase assays of single-cell lysates on a microchip: a complementary method for enzymatic analysis of single cells, *Proceedings of the IEEE*, 92 (2004) 115-125.
- [104] J. Zhou, A.V. Ellis, N.H. Voelcker, Recent developments in PDMS surface modification for microfluidic devices, *Electrophoresis*, 31 (2010) 2-16.
- [105] E. Galembeck, A. Alonso, N.C. Meirelles, Effects of polyoxyethylene chain length on erythrocyte hemolysis induced by poly[oxyethylene (n) nonylphenol] non-ionic surfactants, *Chemico-biological interactions*, 113 (1998) 91-103.
- [106] P.S. Prete, K. Gomes, S.V. Malheiros, N.C. Meirelles, E. de Paula, Solubilization of human erythrocyte membranes by non-ionic surfactants of the polyoxyethylene alkyl ethers series, *Biophysical chemistry*, 97 (2002) 45-54.
- [107] C. Sblano, S. Micelli, G. Notaracchille, D. Meleleo, Effects of n-Octyl- β -D-Glucopyranoside on Human and Rat Erythrocyte Membrane Stability Against Hemolysis, *Open Biology Journal*, 5 (2012) 1-5.
- [108] D. Trägner, A. Csordas, Biphasic interaction of Triton detergents with the erythrocyte membrane, *The Biochemical journal*, 244 (1987) 605-609.
- [109] A.M. Katz, F.C. Messineo, Lipid-membrane interactions and the pathogenesis of ischemic damage in the myocardium, *Circulation research*, 48 (1981) 1-16.
- [110] W.Y. Ng, A. Ramos, Y.C. Lam, I.P. Wijaya, I. Rodriguez, DC-biased AC-electrokinetics: a conductivity gradient driven fluid flow, *Lab Chip*, 11 (2011) 4241-4247.
- [111] S.K. Srivastava, A. Artemiou, A.R. Minerick, Direct current insulator-based dielectrophoretic characterization of erythrocytes: ABO-Rh human blood typing, *ELECTROPHORESIS*, 32 (2011) 2530-2540.
- [112] B.G. Hawkins, C. Huang, S. Arasanipalai, B.J. Kirby, Automated dielectrophoretic characterization of *Mycobacterium smegmatis*, *Anal Chem*, 83 (2011) 3507-3515.
- [113] S. Fiedler, R. Hagedorn, T. Schnelle, E. Richter, B. Wagner, G. Fuhr, Diffusional Electrotitration: Generation of pH Gradients over Arrays of Ultramicroelectrodes Detected by Fluorescence, *Analytical Chemistry*, 67 (1995) 820-828.

- [114] A. Gencoglu, F. Camacho-Alanis, V.T. Nguyen, A. Nakano, A. Ros, A.R. Minerick, Quantification of pH gradients and implications in insulator-based dielectrophoresis of biomolecules, *ELECTROPHORESIS*, 32 (2011) 2436-2447.
- [115] N.C. Rudd, S. Cannan, E. Bitziou, I. Ciani, A.L. Whitworth, P.R. Unwin, Fluorescence Confocal Laser Scanning Microscopy as a Probe of pH Gradients in Electrode Reactions and Surface Activity, *Analytical Chemistry*, 77 (2005) 6205-6217.
- [116] S. Cannan, I. Douglas Macklam, P.R. Unwin, Three-dimensional imaging of proton gradients at microelectrode surfaces using confocal laser scanning microscopy, *Electrochemistry Communications*, 4 (2002) 886-892.
- [117] I.I. Jeican, H. Matei, A. Istrate, E. Mironescu, Ș. Bâlici, Changes observed in erythrocyte cells exposed to an alternating current, *Clujul Medical*, 90 (2017) 154.
- [118] C. Yang, C.J. Wu, A.E. Ostafin, G. Thibaudau, A.R. Minerick, Size and medium conductivity dependence on dielectrophoretic behaviors of gas core poly-L-lysine shell nanoparticles, *Electrophoresis*, 36 (2015) 1002-1010.
- [119] S.B. Brummer, J. McHardy, M.J. Turner, Electrical stimulation with Pt electrodes: Trace analysis for dissolved platinum and other dissolved electrochemical products, *Brain, behavior and evolution*, 14 (1977) 10-22.
- [120] S. Musa, D.R. Rand, C. Bartic, W. Eberle, B. Nuttin, G. Borghs, Coulometric Detection of Irreversible Electrochemical Reactions Occurring at Pt Microelectrodes Used for Neural Stimulation, *Analytical Chemistry*, 83 (2011) 4012-4022.
- [121] K. Wissel, G. Brandes, N. Pütz, G.L. Angrisani, J. Thieleke, T. Lenarz, M. Durisin, Platinum corrosion products from electrode contacts of human cochlear implants induce cell death in cell culture models, *PLOS ONE*, 13 (2018) e0196649.
- [122] T. Heida, W.L. Rutten, E. Marani, Dielectrophoretic trapping of dissociated fetal cortical rat neurons, *IEEE transactions on biomedical engineering*, 48 (2001) 921-930.
- [123] Y. Huang, X.-B. Wang, F.F. Becker, P.R. Gascoyne, Membrane changes associated with the temperature-sensitive P85gag-mos-dependent transformation of rat kidney cells as determined by dielectrophoresis and electrorotation, *Biochimica et Biophysica Acta (BBA)-Biomembranes*, 1282 (1996) 76-84.
- [124] S. Otto, U. Kaletta, F.F. Bier, C. Wenger, R. Hölzel, Dielectrophoretic immobilisation of antibodies on microelectrode arrays, *Lab on a Chip*, 14 (2014) 998-1004.
- [125] A. Sonnenberg, J.Y. Marciniak, R. Krishnan, M.J. Heller, Dielectrophoretic isolation of DNA and nanoparticles from blood, *Electrophoresis*, 33 (2012) 2482-2490.
- [126] M. Suzuki, T. Yasukawa, H. Shiku, T. Matsue, Negative dielectrophoretic patterning with different cell types, *Biosensors and bioelectronics*, 24 (2008) 1043-1047.
- [127] A. Sonnenberg, J.Y. Marciniak, J. McCanna, R. Krishnan, L. Rassenti, T.J. Kipps, M.J. Heller, Dielectrophoretic isolation and detection of cfc-DNA nanoparticulate biomarkers and virus from blood, *Electrophoresis*, 34 (2013) 1076-1084.
- [128] T. Kakutani, S. Shibatani, M. Sugai, Electrorotation of non-spherical cells: Theory for ellipsoidal cells with an arbitrary number of shells, *Bioelectrochemistry and Bioenergetics*, 31 (1993) 131-145.
- [129] A. Irimajiri, T. Hanai, A. Inouye, A dielectric theory of "multi-stratified shell" model with its application to a lymphoma cell, *Journal of Theoretical Biology*, 78 (1979) 251-269.
- [130] B. Çetin, D. Li, Dielectrophoresis in microfluidics technology, *ELECTROPHORESIS*, 32 (2011) 2410-2427.
- [131] J.M. Cruz, F.J. García-Diego, Dielectrophoretic motion of oblate spheroidal particles. Measurements of motion of red blood cells using the Stokes method, *Journal of Physics D: Applied Physics*, 31 (1998) 1745.

- [132] M. Nakamura, N. Sato, N. Hoshi, O. Sakata, Outer Helmholtz Plane of the Electrical Double Layer Formed at the Solid Electrode–Liquid Interface, *ChemPhysChem*, 12 (2011) 1430-1434.
- [133] W.B. Russel, W. Russel, D.A. Saville, W.R. Schowalter, *Colloidal dispersions*, Cambridge university press, Place Published, 1991.
- [134] Y.-L. Deng, J.-S. Chang, Y.-J. Juang, Separation of microalgae with different lipid contents by dielectrophoresis, *Bioresource technology*, 135 (2013) 137-141.
- [135] T. Zhou, S.F. Perry, Y. Ming, S. Petryna, V. Fluck, S. Tatic-Lucic, Separation and assisted patterning of hippocampal neurons from glial cells using positive dielectrophoresis, *Biomedical microdevices*, 17 (2015) 62.
- [136] K. Yang, J. Wu, Investigation of microflow reversal by ac electrokinetics in orthogonal electrodes for micropump design, *Biomicrofluidics*, 2 (2008) 024101.
- [137] T. Geng, C. Lu, Microfluidic electroporation for cellular analysis and delivery, *Lab Chip*, 13 (2013) 3803-3821.
- [138] J. Kim, M. Johnson, P. Hill, B.K. Gale, Microfluidic sample preparation: cell lysis and nucleic acid purification, *Integrative biology : quantitative biosciences from nano to macro*, 1 (2009) 574-586.
- [139] S. Movahed, D. Li, Microfluidics cell electroporation, *Microfluidics and Nanofluidics*, 10 (2011) 703-734.
- [140] S.-W. Lee, Y.-C. Tai, A micro cell lysis device, *Sensors and Actuators A: Physical*, 73 (1999) 74-79.
- [141] M.-S. Hung, Y.-T. Chang, Single cell lysis and DNA extending using electroporation microfluidic device, *BioChip journal*, 6 (2012) 84-90.
- [142] C. Church, J. Zhu, G. Huang, T.-R. Tzeng, X. Xuan, Integrated electrical concentration and lysis of cells in a microfluidic chip, *Biomicrofluidics*, 4 (2010) 044101.
- [143] G. Mernier, N. Piacentini, T. Braschler, N. Demierre, P. Renaud, Continuous-flow electrical lysis device with integrated control by dielectrophoretic cell sorting, *Lab on a Chip*, 10 (2010) 2077-2082.
- [144] M.A. McClain, C.T. Culbertson, S.C. Jacobson, N.L. Allbritton, C.E. Sims, J.M. Ramsey, Microfluidic devices for the high-throughput chemical analysis of cells, *Analytical chemistry*, 75 (2003) 5646-5655.
- [145] H. Sedgwick, F. Caron, P. Monaghan, W. Kolch, J. Cooper, Lab-on-a-chip technologies for proteomic analysis from isolated cells, *Journal of The Royal Society Interface*, 5 (2008) S123-S130.
- [146] J.K. Lim, H. Zhou, R.D. Tilton, Liposome rupture and contents release over coplanar microelectrode arrays, *Journal of colloid and interface science*, 332 (2009) 113-121.
- [147] J. Loomis-Husselbee, P. Cullen, R. Irvine, A. Dawson, Electroporation can cause artefacts due to solubilization of cations from the electrode plates. Aluminum ions enhance conversion of inositol 1, 3, 4, 5-tetrakisphosphate into inositol 1, 4, 5-trisphosphate in electroporated L1210 cells, *Biochemical Journal*, 277 (1991) 883-885.
- [148] H. Shafiee, M.B. Sano, E.A. Henslee, J.L. Caldwell, R.V. Davalos, Selective isolation of live/dead cells using contactless dielectrophoresis (cDEP), *Lab Chip*, 10 (2010) 438-445.
- [149] A. Sonnenberg, J.Y. Marciniak, J. McCanna, R. Krishnan, L. Rassenti, T.J. Kipps, M.J. Heller, Dielectrophoretic isolation and detection of cfc-DNA nanoparticulate biomarkers and virus from blood, *Electrophoresis*, 34 (2013) 1076-1084.
- [150] M. Curreli, R. Zhang, F.N. Ishikawa, H.-K. Chang, R.J. Cote, C. Zhou, M.E. Thompson, Real-time, label-free detection of biological entities using nanowire-based FETs, *IEEE Trans. Nanotechnol*, 7 (2008) 651-667.

- [151] R.K. Jain, Y.K. Gautam, V. Dave, A.K. Chawla, R. Chandra, A study on structural, optical and hydrophobic properties of oblique angle sputter deposited HfO₂ films, *Applied Surface Science*, 283 (2013) 332-338.
- [152] S.-S. Lin, Optical properties of HfO₂ nanoceramic films as a function of N–Bi co-doping, *Ceramics International*, 40 (2014) 5707-5713.
- [153] S.-S. Lin, C.-S. Liao, S.-Y. Fan, Effects of substrate temperature on properties of HfO₂, HfO₂:Al and HfO₂:W films, *Surface and Coatings Technology*, 271 (2015) 269-275.
- [154] S. Schreier, S.V.P. Malheiros, E. de Paula, Surface active drugs: self-association and interaction with membranes and surfactants. Physicochemical and biological aspects, *Biochimica et Biophysica Acta (BBA) - Biomembranes*, 1508 (2000) 210-234.
- [155] C.-T. Chu, P.D. Fuqua, J.D. Barrie, Corrosion characterization of durable silver coatings by electrochemical impedance spectroscopy and accelerated environmental testing, *Appl. Opt.*, 45 (2006) 1583-1593.
- [156] S.K. Srivastava, P.R. Daggolu, S.C. Burgess, A.R. Minerick, Dielectrophoretic characterization of erythrocytes: positive ABO blood types, *Electrophoresis*, 29 (2008) 5033-5046.
- [157] M.E. Reid, N. Mohandas, Red blood cell blood group antigens: structure and function, *Seminars in hematology*, 41 (2004) 93-117.
- [158] M. Dimaki, M. Vergani, A. Heiskanen, D. Kwasny, L. Sasso, M. Carminati, J.A. Gerrard, J. Emneus, W.E. Svendsen, A compact microelectrode array chip with multiple measuring sites for electrochemical applications, *Sensors (Basel, Switzerland)*, 14 (2014) 9505-9521.
- [159] R. Krishnan, D.A. Dehlinger, G.J. Gemmen, R.L. Mifflin, S.C. Esener, M.J. Heller, Interaction of Nanoparticles at the DEP Microelectrode Interface under High Conductance Conditions, *Electrochemistry communications*, 11 (2009) 1661-1666.
- [160] P.J. Canatella, J.F. Karr, J.A. Petros, M.R. Prausnitz, Quantitative study of electroporation-mediated molecular uptake and cell viability, *Biophysical journal*, 80 (2001) 755-764.
- [161] J. Olofsson, K. Nolkrantz, F. Ryttsén, B.A. Lambie, S.G. Weber, O. Orwar, Single-cell electroporation, *Current Opinion in Biotechnology*, 14 (2003) 29-34.
- [162] J. Teissié, M.P. Rols, An experimental evaluation of the critical potential difference inducing cell membrane electroporation, *Biophysical journal*, 65 (1993) 409-413.
- [163] T. Grahl, H. Märkl, Killing of microorganisms by pulsed electric fields, *Applied Microbiology and Biotechnology*, 45 (1996) 148-157.
- [164] W.H. Organization, World Health Organization Model List of Essential In Vitro Diagnostics First edition (2018), Geneva: World Health Organization, (2018).
- [165] J.L. Prieto, H.-W. Su, H.W. Hou, M.P. Vera, B.D. Levy, R.M. Baron, J. Han, J. Voldman, Monitoring sepsis using electrical cell profiling, *Lab on a chip*, 16 (2016) 4333-4340.
- [166] R.S. Kuczenski, H.-C. Chang, A. Revzin, Dielectrophoretic microfluidic device for the continuous sorting of Escherichia coli from blood cells, *Biomicrofluidics*, 5 (2011) 032005.
- [167] E.A. Henslee, M.B. Sano, A.D. Rojas, E.M. Schmelz, R.V. Davalos, Selective concentration of human cancer cells using contactless dielectrophoresis, *ELECTROPHORESIS*, 32 (2011) 2523-2529.
- [168] T.N.G. Adams, A.Y.L. Jiang, P.D. Vyas, L.A. Flanagan, Separation of neural stem cells by whole cell membrane capacitance using dielectrophoresis, *Methods*, 133 (2018) 91-103.
- [169] B.H. Lapizco-Encinas, B.A. Simmons, E.B. Cummings, Y. Fintschenko, Dielectrophoretic Concentration and Separation of Live and Dead Bacteria in an Array of Insulators, *Analytical Chemistry*, 76 (2004) 1571-1579.
- [170] N.G. Green, H. Morgan, J.J. Milner, Manipulation and trapping of sub-micron bioparticles using dielectrophoresis, *Journal of Biochemical and Biophysical Methods*, 35 (1997) 89-102.

- [171] J. Suehiro, M. Shutou, T. Hatano, M. Hara, High sensitive detection of biological cells using dielectrophoretic impedance measurement method combined with electroporabilization, *Sensors and Actuators B: Chemical*, 96 (2003) 144-151.
- [172] E.T. Lagally, S.H. Lee, H.T. Soh, Integrated microsystem for dielectrophoretic cell concentration and genetic detection, *Lab Chip*, 5 (2005) 1053-1058.
- [173] T.N.G. Adams, K.M. Leonard, A.R. Minerick, Frequency sweep rate dependence on the dielectrophoretic response of polystyrene beads and red blood cells, *Biomicrofluidics*, 7 (2013) 64114-64114.
- [174] J. Yang, Y. Huang, X.-B. Wang, F.F. Becker, P.R.C. Gascoyne, Differential Analysis of Human Leukocytes by Dielectrophoretic Field-Flow-Fractionation, *Biophysical journal*, 78 (2000) 2680-2689.
- [175] D. Mark, S. Haeberle, G. Roth, F. Von Stetten, R. Zengerle, Microfluidic lab-on-a-chip platforms: requirements, characteristics and applications, *Microfluidics Based Microsystems*, Springer, Place Published, 2010, pp. 305-376.
- [176] E. Sackmann, Biological membranes architecture and function, *Structure and Dynamics of Membranes*, 1 (1995) 1-63.
- [177] S. Dufour, M. Deleu, K. Nott, B. Wathélet, P. Thonart, M. Paquot, Hemolytic activity of new linear surfactin analogs in relation to their physico-chemical properties, *Biochimica et biophysica acta*, 1726 (2005) 87-95.
- [178] B. Isomaa, H. Hägerstrand, G. Paatero, Shape transformations induced by amphiphiles in erythrocytes, *Biochimica et Biophysica Acta (BBA) - Biomembranes*, 899 (1987) 93-103.
- [179] M.P. Sheetz, S.J. Singer, Biological membranes as bilayer couples. A molecular mechanism of drug-erythrocyte interactions, *Proceedings of the National Academy of Sciences of the United States of America*, 71 (1974) 4457-4461.
- [180] J.P. Dilger, S. McLaughlin, T.J. McIntosh, S.A. Simon, The dielectric constant of phospholipid bilayers and the permeability of membranes to ions, *Science*, 206 (1979) 1196-1198.
- [181] R. Pethig, D.B. Kell, The passive electrical properties of biological systems: their significance in physiology, biophysics and biotechnology, *Physics in Medicine & Biology*, 32 (1987) 933.
- [182] Y.H. Su, M. Tsegaye, W. Varhue, K.T. Liao, L.S. Abebe, J.A. Smith, R.L. Guerrant, N.S. Swami, Quantitative dielectrophoretic tracking for characterization and separation of persistent subpopulations of *Cryptosporidium parvum*, *Analyst*, 139 (2014) 66-73.
- [183] C.H. Tan, Z.J. Huang, X.G. Huang, Rapid determination of surfactant critical micelle concentration in aqueous solutions using fiber-optic refractive index sensing, *Analytical biochemistry*, 401 (2010) 144-147.
- [184] A.L. Koch, Theory of the angular dependence of light scattered by bacteria and similar-sized biological objects, *Journal of Theoretical Biology*, 18 (1968) 133-156.
- [185] C.E. Alupoaei, L.H. García-Rubio, An Interpretation Model For The UV-VIS Spectra Of Microorganisms, *Chemical Engineering Communications*, 192 (2005) 198-218.
- [186] S. Henkelman, G. Rakhorst, J. Blanton, W. van Oeveren, Standardization of incubation conditions for hemolysis testing of biomaterials, *Materials Science and Engineering: C*, 29 (2009) 1650-1654.
- [187] G.M. Xiong, S. Yuan, J.K. Wang, A.T. Do, N.S. Tan, K.S. Yeo, C. Choong, Imparting electroactivity to polycaprolactone fibers with heparin-doped polypyrrole: Modulation of hemocompatibility and inflammatory responses, *Acta Biomaterialia*, 23 (2015) 240-249.
- [188] M.L. Turgeon, *Clinical hematology: theory and procedures*, Lippincott Williams & Wilkins, Place Published, 2005.

- [189] P.G. Bhat, D.R. Flanagan, M.D. Donovan, Drug diffusion through cystic fibrotic mucus: Steady-state permeation, rheologic properties, and glycoprotein morphology, *Journal of pharmaceutical sciences*, 85 (1996) 624-630.
- [190] K. Khairy, J. Foo, J. Howard, Shapes of Red Blood Cells: Comparison of 3D Confocal Images with the Bilayer-Couple Model, *Cellular and Molecular Bioengineering*, 1 (2008) 173.
- [191] F.A. Wagener, H.-D. Volk, D. Willis, N.G. Abraham, M.P. Soares, G.J. Adema, C.G. Figdor, Different faces of the heme-heme oxygenase system in inflammation, *Pharmacological reviews*, 55 (2003) 551-571.
- [192] V. Jeney, G. Balla, J. Balla, Red blood cell, hemoglobin and heme in the progression of atherosclerosis, *Frontiers in physiology*, 5 (2014) 379.
- [193] J. Andrasko, The estimation of age of bloodstains by HPLC analysis, *Journal of forensic sciences*, 42 (1997) 601-607.
- [194] E.K. Hanson, J. Ballantyne, A Blue Spectral Shift of the Hemoglobin Soret Band Correlates with the Age (Time Since Deposition) of Dried Bloodstains, *PLOS ONE*, 5 (2010) e12830.
- [195] M. Wojdyla, S. Raj, D. Petrov, Absorption spectroscopy of single red blood cells in the presence of mechanical deformations induced by optical traps, *Journal of biomedical optics*, 17 (2012) 97006-97001.
- [196] M.B. Strader, T. Kassa, F. Meng, F.B. Wood, R.E. Hirsch, J.M. Friedman, A.I. Alayash, Oxidative instability of hemoglobin E ($\beta 26 \text{ Glu} \rightarrow \text{Lys}$) is increased in the presence of free α subunits and reversed by α -hemoglobin stabilizing protein (AHSP): Relevance to HbE/ β -thalassemia, *Redox biology*, 8 (2016) 363-374.
- [197] F. Meng, T. Kassa, M.B. Strader, J. Soman, J.S. Olson, A.I. Alayash, Substitutions in the β subunits of sickle-cell hemoglobin improve oxidative stability and increase the delay time of sickle-cell fiber formation, *Journal of Biological Chemistry*, (2019) jbc. RA118. 006452.
- [198] M. Banerjee, M. Pramanik, D. Bhattacharya, M. Lahiry, S. Basu, A. Chakrabarti, Faster heme loss from hemoglobin E than HbS, in acidic pH: effect of aminophospholipids, *Journal of biosciences*, 36 (2011) 809-816.
- [199] F. Meng, A.I. Alayash, Determination of extinction coefficients of human hemoglobin in various redox states, *Analytical biochemistry*, 521 (2017) 11-19.
- [200] W. Sun, X. Li, Y. Wang, R. Zhao, K. Jiao, Electrochemistry and electrocatalysis of hemoglobin on multi-walled carbon nanotubes modified carbon ionic liquid electrode with hydrophilic EMIMBF₄ as modifier, *Electrochimica Acta*, 54 (2009) 4141-4148.
- [201] J.F. Rusling, A.E.F. Nassar, Enhanced electron transfer for myoglobin in surfactant films on electrodes, *Journal of the American Chemical Society*, 115 (1993) 11891-11897.
- [202] S. Garabagiu, A spectroscopic study on the interaction between gold nanoparticles and hemoglobin, *Materials Research Bulletin*, 46 (2011) 2474-2477.
- [203] A.B. Anderson, C.R. Robertson, Absorption spectra indicate conformational alteration of myoglobin adsorbed on polydimethylsiloxane, *Biophysical journal*, 68 (1995) 2091-2097.
- [204] D. Koley, A.J. Bard, Triton X-100 concentration effects on membrane permeability of a single HeLa cell by scanning electrochemical microscopy (SECM), *Proceedings of the National Academy of Sciences*, 107 (2010) 16783-16787.
- [205] A. Irimajiri, K. Asami, T. Ichinowatari, Y. Kinoshita, Passive electrical properties of the membrane and cytoplasm of cultured rat basophil leukemia cells. II. Effects of osmotic perturbation, *Biochimica et Biophysica Acta (BBA)-Biomembranes*, 896 (1987) 214-223.
- [206] K. Asami, Characterization of biological cells by dielectric spectroscopy, *Journal of Non-Crystalline Solids*, 305 (2002) 268-277.
- [207] C. Yi, C.-W. Li, S. Ji, M. Yang, Microfluidics technology for manipulation and analysis of biological cells, *Analytica chimica acta*, 560 (2006) 1-23.

- [208] K. Ohno, K. Tachikawa, A. Manz, Microfluidics: applications for analytical purposes in chemistry and biochemistry, *Electrophoresis*, 29 (2008) 4443-4453.
- [209] J. Yang, Y. Huang, X.-B. Wang, F.F. Becker, P.R. Gascoyne, Differential analysis of human leukocytes by dielectrophoretic field-flow-fractionation, *Biophysical journal*, 78 (2000) 2680-2689.
- [210] T. Muller, A. Pfennig, P. Klein, G. Gradl, M. Jager, T. Schnelle, The potential of dielectrophoresis for single-cell experiments, *IEEE engineering in medicine and biology magazine*, 22 (2003) 51-61.
- [211] J. Gimsa, D. Wachner, A unified resistor-capacitor model for impedance, dielectrophoresis, electrorotation, and induced transmembrane potential, *Biophysical journal*, 75 (1998) 1107-1116.
- [212] J.H. Nieuwenhuis, M.J. Vellekoop, Simulation study of dielectrophoretic particle sorters, *Sensors and actuators B: Chemical*, 103 (2004) 331-338.
- [213] L.-C. Hsiung, C.-L. Chiang, C.-H. Wang, Y.-H. Huang, C.-T. Kuo, J.-Y. Cheng, C.-H. Lin, V. Wu, H.-Y. Chou, D.-S. Jong, Dielectrophoresis-based cellular microarray chip for anticancer drug screening in perfusion microenvironments, *Lab on a Chip*, 11 (2011) 2333-2342.
- [214] S. Mahabadi, M.P. Hughes, F.H. Labeed, Abstract 3490: Measurement of Gifinitib (ZD1839) effect on electrophysiological properties of head and neck cancer cells using Dielectrophoresis (DEP), *Cancer Research*, 74 (2014) 3490-3490.
- [215] C. Huang, H. Liu, N.H. Bander, B.J. Kirby, Enrichment of prostate cancer cells from blood cells with a hybrid dielectrophoresis and immunocapture microfluidic system, *Biomedical microdevices*, 15 (2013) 941-948.
- [216] Y.-H. Su, C.A. Warren, R.L. Guerrant, N.S. Swami, Dielectrophoretic monitoring and interstrain separation of intact *Clostridium difficile* based on their S (Surface)-layers, *Analytical chemistry*, 86 (2014) 10855-10863.
- [217] K. Khoshmanesh, S. Baratchi, F.J. Tovar-Lopez, S. Nahavandi, D. Wlodkowic, A. Mitchell, K. Kalantar-zadeh, On-chip separation of *Lactobacillus* bacteria from yeasts using dielectrophoresis, *Microfluidics and Nanofluidics*, 12 (2012) 597-606.
- [218] E.M. Nascimento, N. Nogueira, T. Silva, T. Braschler, N. Demierre, P. Renaud, A.G. Oliva, Dielectrophoretic sorting on a microfabricated flow cytometer: Label free separation of *Babesia bovis* infected erythrocytes, *Bioelectrochemistry*, 73 (2008) 123-128.
- [219] M.F. Tafur, K.S. Vijayaragavan, C.L. Heldt, Reduction of porcine parvovirus infectivity in the presence of protecting osmolytes, *Antiviral research*, 99 (2013) 27-33.
- [220] D.W. Bolen, Effects of naturally occurring osmolytes on protein stability and solubility: issues important in protein crystallization, *Methods*, 34 (2004) 312-322.
- [221] M. Boisvert, S. Fernandes, P. Tijssen, Multiple pathways involved in porcine parvovirus cellular entry and trafficking toward the nucleus, *Journal of virology*, 84 (2010) 7782-7792.
- [222] G.G. Prikhod'ko, H. Reyes, I. Vasilyeva, T.F. Busby, Establishment of a porcine parvovirus (PPV) DNA standard and evaluation of a new LightCycler nested-PCR assay for detection of PPV, *Journal of virological methods*, 111 (2003) 13-19.
- [223] S. Halder, R. Ng, M. Agbandje-McKenna, Parvoviruses: structure and infection, *Future Virology*, 7 (2012) 253-278.
- [224] Z.R. Gagnon, Cellular dielectrophoresis: applications to the characterization, manipulation, separation and patterning of cells, *Electrophoresis*, 32 (2011) 2466-2487.
- [225] Y. Demircan, E. Ozgur, H. Kulah, Dielectrophoresis: applications and future outlook in point of care, *Electrophoresis*, 34 (2013) 1008-1027.
- [226] R. Pethig, Dielectrophoresis: Status of the theory, technology, and applications, *Biomicrofluidics*, 4 (2010) 022811.

- [227] C. Grosse, A. Delgado, Dielectric dispersion in aqueous colloidal systems, *Current Opinion in Colloid & Interface Science*, 15 (2010) 145-159.
- [228] X. Wang, F.F. Becker, P.R. Gascoyne, Membrane dielectric changes indicate induced apoptosis in HL-60 cells more sensitively than surface phosphatidylserine expression or DNA fragmentation, *Biochimica et biophysica acta*, 1564 (2002) 412-420.
- [229] T. Adams, K. Leonard, A. Minerick, Frequency sweep rate dependence on the dielectrophoretic response of polystyrene beads and red blood cells, *Biomicrofluidics*, 7 (2013) 064114.
- [230] A.R. Minerick, J.L. Collins, K.M. Leonard, T.N. Adams, Methods and systems for identifying a particle using dielectrophoresis, Google Patents, 2016.
- [231] H. Narayanan Unni, D. Hartono, L. Yue Lanry Yung, M. Mah-Lee Ng, H. Pueh Lee, B. Cheong Khoo, K.-M. Lim, Characterization and separation of *Cryptosporidium* and *Giardia* cells using on-chip dielectrophoresis, *Biomicrofluidics*, 6 (2012) 012805.
- [232] Y.-H. Su, M. Tsegaye, W. Varhue, K.-T. Liao, L.S. Abebe, J.A. Smith, R.L. Guerrant, N.S. Swami, Quantitative dielectrophoretic tracking for characterization and separation of persistent subpopulations of *Cryptosporidium parvum*, *Analyst*, 139 (2014) 66-73.
- [233] H. Zhang, Y. Huang, Q. Du, X. Luo, L. Zhang, X. Zhao, D. Tong, Porcine parvovirus infection induces apoptosis in PK-15 cells through activation of p53 and mitochondria-mediated pathway, *Biochemical and biophysical research communications*, 456 (2015) 649-655.
- [234] G.L. Gulati, *Blood Cell Morphology: Grading Guide*, American Society for Clinical Pathology Press Chicogo, IL, Place Published, 2009.
- [235] M. Rasia, A. Bollini, Red blood cell shape as a function of medium's ionic strength and pH, *Biochimica et Biophysica Acta (BBA)-Biomembranes*, 1372 (1998) 198-204.
- [236] T.M. Fischer, Shape memory of human red blood cells, *Biophysical journal*, 86 (2004) 3304-3313.
- [237] T.Y. Tsong, E. Kingsley, Hemolysis of human erythrocyte induced by a rapid temperature jump, *Journal of Biological Chemistry*, 250 (1975) 786-789.
- [238] A.R. Minerick, J.L. Collins, K.M. Leonard, T.N. Adams, Methods and systems for identifying a particle using dielectrophoresis, Google Patents, 2018.
- [239] G.W. Kemble, T. Danieli, J.M. White, Lipid-anchored influenza hemagglutinin promotes hemifusion, not complete fusion, *Cell*, 76 (1994) 383-391.
- [240] X. Wang, F.F. Becker, P.R. Gascoyne, Membrane dielectric changes indicate induced apoptosis in HL-60 cells more sensitively than surface phosphatidylserine expression or DNA fragmentation, *Biochimica et Biophysica Acta (BBA)-Biomembranes*, 1564 (2002) 412-420.
- [241] D. Bratosin, L. Mitrofan, C. Palii, J. Estaquier, J. Montreuil, Novel fluorescence assay using calcein-AM for the determination of human erythrocyte viability and aging, *Cytometry Part A: the journal of the International Society for Analytical Cytology*, 66 (2005) 78-84.
- [242] O. Bussolati, S. Belletti, J. Uggeri, R. Gatti, G. Orlandini, V. Dall'Asta, G.C. Gazzola, Characterization of apoptotic phenomena induced by treatment with L-asparaginase in NIH3T3 cells, *Experimental cell research*, 220 (1995) 283-291.
- [243] D. Darbari, M. Loyevsky, V. Gordeuk, J.A. Kark, O. Castro, S. Rana, V. Apprey, J. Kurantsin-Mills, Fluorescence measurements of the labile iron pool of sickle erythrocytes, *Blood*, 102 (2003) 357-364.
- [244] H.A. Pohl, Some effects of nonuniform fields on dielectrics, *Journal of Applied Physics*, 29 (1958) 1182-1188.
- [245] H.A. Pohl, The motion and precipitation of suspensoids in divergent electric fields, *Journal of Applied Physics*, 22 (1951) 869-871.

- [246] B.J. Kirby, Micro-and nanoscale fluid mechanics: transport in microfluidic devices, Cambridge university press, Place Published, 2010.
- [247] L.K. Goodhead, F.M. MacMillan, Measuring osmosis and hemolysis of red blood cells, *Advances in physiology education*, 41 (2017) 298-305.
- [248] J.M. Crance, N. Scaramozzino, A. Jouan, D. Garin, Interferon, ribavirin, 6-azauridine and glycyrrhizin: antiviral compounds active against pathogenic flaviviruses, *Antiviral Res*, 58 (2003) 73-79.
- [249] B. Gu, P. Mason, L. Wang, P. Norton, N. Bourne, R. Moriarty, A. Mehta, M. Despande, R. Shah, T. Block, Antiviral profiles of novel iminocyclitol compounds against bovine viral diarrhea virus, West Nile virus, dengue virus and hepatitis B virus, *Antiviral Chemistry and Chemotherapy*, 18 (2007) 49-59.


Appendix A

Letter of Permission

A.1 Letter of Permission for Reference [33] (Chapter 1)



[Home](#) [Account Info](#) [Help](#) 



Title: Dielectrophoretic platforms for bio-microfluidic systems
Author: Khashayar Khoshmanesh, Saeid Nahavandi, Sara Baratchi, Aman Mitchell, Kourosh Kalantar-zadeh
Publication: Biosensors and Bioelectronics
Publisher: Elsevier
Date: 15 January 2011
Copyright © 2010 Elsevier B.V. All rights reserved.

Logged in as:
Sanaz Habibi
Sanaz Habibi
[LOGOUT](#)

Order Completed

Thank you for your order.

This Agreement between Sanaz Habibi -- Sanaz Habibi ("You") and Elsevier ("Elsevier") consists of your license details and the terms and conditions provided by Elsevier and Copyright Clearance Center.

Your confirmation email will contain your order number for future reference.

[printable details](#)

License Number	4558320201033
License date	Mar 29, 2019
Licensed Content Publisher	Elsevier
Licensed Content Publication	Biosensors and Bioelectronics
Licensed Content Title	Dielectrophoretic platforms for bio-microfluidic systems
Licensed Content Author	Khashayar Khoshmanesh, Saeid Nahavandi, Sara Baratchi, Aman Mitchell, Kourosh Kalantar-zadeh
Licensed Content Date	Jan 15, 2011
Licensed Content Volume	26
Licensed Content Issue	5
Licensed Content Pages	15
Type of Use	reuse in a thesis/dissertation
Portion	figures/tables/illustrations
Number of figures/tables/illustrations	1
Format	electronic
Are you the author of this Elsevier article?	No
Will you be translating?	No
Original figure numbers	Figure 3
Title of your thesis/dissertation	EXPLORING THE ROLE AND IMPACT OF MICROSCALE PHENOMENA ON ELECTRODE, MICRODEVICE, AND CELLULAR FUNCTION
Expected completion date	May 2021
Estimated size (number of pages)	180
Requestor Location	Sanaz Habibi 1400 Townsend Drive HOUGHTON, MI 49931 United States Attn: Sanaz Habibi
Publisher Tax ID	98-0397604
Total	0.00 USD

[ORDER MORE](#)[CLOSE WINDOW](#)

Copyright © 2019 Copyright Clearance Center, Inc. All Rights Reserved. [Privacy statement](#), [Terms and Conditions](#). Comments? We would like to hear from you. E-mail us at customerservice@copyright.com